Static and dynamic properties of hexagonally shaped magnetic nanotubes

DISSERTATION

zur Erlangung des Doktorgrades
der Naturwissenschaften (Dr. rer. nat.)
der Fakultät für Physik
der Universität Regensburg

vorgelegt von

Michael Zimmermann

aus Sollngriesbach

im Jahr 2018

Promotionsgesuch eingereicht am: 28.04.2018

Die Arbeit wurde angeleitet von: Prof. Dr. Christian H. Back

Prüfungsausschuss:	Vorsitzender:	Prof. Dr. K. Rincke
	1. Gutachter:	Prof. Dr. C. H. Back
	2. Gutachter:	Prof. Dr. D. Bougeard
	weiterer Prüfer:	Prof. Dr. G. Bali

...Für meinen verstorbenen Vater Michael...

Contents

1 Introduction

Within half a century the area a single bit requires on a magnetic hard disk storage unit reduced in size by about nine orders of magnitude [1]. Nowadays the ongoing miniaturization process encounters fundamental limits that are difficult or even impossible to overcome [2]. Hence many alternative routes are proposed, that are capable of working faster, with less power consumption or increased storage densities. Ideas reach from using spin waves as information carrier [3] to magnetic race track memories [4]. In the latter, domain walls are moved along a nanowire by passing a spin polarized current through the device. Spin angular momentum is transferred from the conduction electrons to the magnetic moments in the domain wall, causing a displacement in the direction of the electron flow [5]. A prerequisite for efficient movement is a high spin polarization in the ferromagnetic material. For bulk permalloy it is approximately 70% [6], resulting in typical velocities in the range of 100-200 m/s for current densities around 10^{12} A/m^2 [1, 7]. The performance of such a device relies on fast information processing and thus a high domain wall velocity. In magnetic nanotubes (NTs) very high velocities are expected due to an increased domain wall stability and, for instance, suppression of velocity limiting effects such as the Walker breakdown [8, 9].

Miniaturization of magnetic devices can be hampered by stray fields of individual domain sections, which cause unwanted interactions. It would thus be favorable to have flux closed magnetic states to enable close packing. A ferromagnetic NT with its lack of magnetic core, can exhibit a variety of stable configurations at zero external field [10]. These are a flux closed vortex state (VS), where the magnetization circulates around the circumference of the tube, a uniform state (US), where the magnetization points parallel to the long axis of the tube, an onion state (OS) and mixed states composed of the previously mentioned. The onion state assumes a special position in this list since it is a metastable state at zero field that can only be obtained after the application of an external magnetic field oriented perpendicularly to the tube axis [11].

Besides the flux closure the vortex state has an additional advantage. It resembles the Damon-Eshbach (DE) configuration for spin waves, where magnetization ($\mathbf{M}$) and wave vector ($\mathbf{k}$) are perpendicular. This is advantageous since spin waves in the DE geometry show a high group velocity and are thus capable of traveling comparably large distances. However, in the absence of any external field or current, the wave vector $\mathbf{k}$ is in general not perpendicular to $\mathbf{M}$ in the ground state configuration of flat magnetic stripes [12]. Theses additional requirements are superseded if NTs exhibit the VS as a zero-field state. Hence, the determination of the ground state is a

crucial task, which will be addressed in this thesis. Former simulations [10] revealed that the ground state at zero field is geometry dependent, meaning it changes with varying NT diameter and metal thickness. With the state (VS, OS and US) also the magnetic properties change. Hence by varying the growth parameters, NTs can easily be designed to fulfill the requirements for different applications. For instance, if used as spin wave guide, the VS would result in the usually preferred DE spin waves, compared to BV in the US.

In early works [13–15], the properties of magnetic NTs have mostly been investigated on large ensembles, due to the small single magnetic moment of individual tubes. This, however, prevents an accurate characterization, since ensembles of NTs often exhibit a distribution in size, shape and orientation, depending strongly on the distance between them during growth. Consequently the investigation of single NTs came into the focus of research [16–19]. Anisotropic magnetoresistance (AMR) measurements on single NTs turned out to be a powerful tool to draw conclusions on the magnetic properties. However, typically rough surfaces made the interpretation and comparison to simulations difficult. In this thesis nearly perfectly grown NTs were chosen as subject of investigation. Magnetic layers are deposited in ultra high vacuum conditions and a dual beam scanning electron microscope (SEM) with focused ion beam (FIB) is utilized to fabricate NTs with defined endings, that are comparable to micromagnetic simulations.

In the course of this thesis the magnetic ground state of hexagonally shaped ferromagnetic NTs and ways to manipulate this state are investigated in detail. To do so a variety of different NTs consisting of permalloy (Py) and aluminum oxide (Al_2O_3) buffer layers are fabricated. Individual NTs are then contacted with gold leads and measured utilizing the AMR effect. Conclusions on inherent magnetic properties and differences to former investigations will be highlighted. We find for instance vortex states that are independent of the NTs geometry. This extends the range of realizable applications, since the NTs can be fabricated in various lengths, without significantly changing their magnetic properties.

After the static analysis, a study on dynamic properties is presented. For this purpose three different techniques are applied: Planar microresonator based ferromagnetic resonance (PMR based FMR), time resolved magneto optical Kerr effect (TRMOKE) spectroscopy and scanning transmission X-ray microscopy (STXM). PMR averages the magnetic response of the whole specimen. In contrast, TRMOKE with its spatial resolution down to 400 nm relies on reflection of light and is thus only sensitive to one side facet of the NT. STXM operates in transmission, giving access to all sides of the NT. However, opposing facets might cancel out their signal for certain magnetization configurations. In combination with simulations these methods provide a powerful analysis tool for complex magnetic textures.

The three dimensional architecture of the hexagonally shaped NT will play a major role in this thesis. It offers the possibility of localized resonances dictated by the sense of rotation of the NT with respect to the orientation of the externally applied

field. These regions could potentially act as spin wave channels [20], that can be turned on and off by currents or external fields that influence the magnetic state.

The thesis concludes with a discussion on spin waves in permalloy NTs. Here different types of excitation geometries will be discussed, since a homogeneous radio frequency (rf) excitation, equivalent on all six facets, is hard to realize experimentally. Instead, during measurements the NT will be placed on top of an antenna, leading to an inhomogeneous driving field. This ultimately leads to mode patterns, which can tremendously vary from those resulting from a homogeneous excitation.

2 Theoretical considerations

This chapter discusses the theoretical concepts necessary to interpret the experimental results presented in chapter 4. First, magnetic energy contributions in ultrathin films are introduced. On these grounds the ferromagnetic resonance (FMR) for different configurations of external field $\mathbf{H}$ and internal magnetization $\mathbf{M}$ is discussed in section 2.2. The spin wave dispersion relation is explained and derived for flat films and circular NTs in section 2.3. Subsequently various types of domain walls for selected geometries, including bulk systems, nano-stripes and NTs, are presented. Followed by an introduction of the anisotropic magnetoresistance. Section 2.6 finally addresses the general method of finite-difference micromagnetic simulations based on the open-source software mumax3.

2.1 Magnetic energies and fields in ultrathin ferromagnetic films

The direction of the magnetization vector in a ferromagnetic material is determined by its total energy density

$$\varepsilon_{\text{tot}} = \varepsilon_{\text{ex}} + \varepsilon_{\text{dem}} + \varepsilon_{\text{ani}} + \varepsilon_{\text{zee}}, \tag{2.1}$$

comprising exchange energy density ε_{ex}, demagnetizing energy density ε_{dem}, anisotropy energy density ε_{ani} and Zeeman energy density ε_{zee}. The magnetization vector in ferromagnetic materials may therefore favor a particular orientation direction without an applied magnetic field ($\varepsilon_{\text{zee}} = 0$). In such a situation the magnetic moments will align parallel to the energetically favorable, so-called, 'easy axis'. Whereas the 'hard axis' is defined as the direction of maximum energy. Thus, application of magnetic fields in various directions can cause different responses of the magnetic moments.

Subsections 2.1.1 to 2.1.4 discuss the origin and magnitude of each contribution appearing in Eq. (2.1).

2.1.1 Exchange energy

The exchange interaction is a consequence of the Coulomb interaction and the Pauli principle [21]. Considering an itinerant ferromagnet, such as iron, cobalt or nickel, the distance between same-spin electrons is larger than for different-spin

electrons, since electrons with equivalent spin orientation are not allowed to occupy the same electronic state. Therefore the Coulomb interaction can be minimized when the magnetic moments are aligned parallel. Consequently, a larger area of the reciprocal space has to be populated, resulting in an increase of kinetic energy. Materials, for which the gain in kinetic energy is less than the loss in Coulomb energy align their magnetic moments parallel, hence become ferromagnetic. Once achieved, the ferromagnetism can be sustained until a critical temperature, the Curie temperature T_C. For $T > T_\mathrm{C}$ thermal fluctuations destroy the magnetic order, creating a paramagnetic state.

For a lattice of localized spins the exchange interaction can be quantified using the Heisenberg model. The associated Hamiltonian reads [21]

$$\mathcal{H}_\mathrm{ex} = -\sum_{\mathrm{i>j}} 2J_\mathrm{ij}\mathbf{S}_\mathrm{i}\cdot\mathbf{S}_\mathrm{j}, \tag{2.2}$$

where J_ij is the exchange integral linking the i-th magnetic moment with spin $\mathbf{S}_i$ and the j-th magnetic moment with spin $\mathbf{S}_j$. Since the exchange interaction is short ranged it is usually well described by nearest neighbor interactions, yielding $J_\mathrm{ij} = J$ in Eq. (2.2). For $J > 0$ the spins align parallel describing a ferromagnet whereas for $J < 0$ the spins align anti-parallel forming an antiferromagnet.

Usually a continuum approximation of the Heisenberg model is considered for a specific crystal lattice. It can be obtained by integrating over the unit magnetization profile $\mathbf{m}$ within the sample volume V

$$\varepsilon_\mathrm{ex} = \frac{E_\mathrm{ex}}{V} = \frac{A}{V}\int \left((\boldsymbol{\nabla} m_\mathrm{x})^2 + (\boldsymbol{\nabla} m_\mathrm{y})^2 + (\boldsymbol{\nabla} m_\mathrm{z})^2\right) dV, \tag{2.3}$$

where $m_\mathrm{i} = M_\mathrm{i}/M_\mathrm{S}$ with $i \in \{\mathrm{x},\mathrm{y},\mathrm{z}\}$ are the unit magnetization components and $A = JS^2z/a$ is the exchange constant with lattice constant a and number of atoms per unit cell z. M_S denotes the saturation magnetization.

The exchange energy density ε_ex is zero in Eq. (2.1) if the material can be treated in the macrospin approximation [22] where all magnetic moments behave as one single magnetization vector (uniform magnetization). This assumption usually applies, if the lateral dimensions of a magnetic film are sufficiently small and the film thickness is less than the exchange length, defined as [22]

$$l_\mathrm{ex} = \left(\frac{2A}{\mu_0 M_\mathrm{S}^2}\right)^{1/2}, \tag{2.4}$$

where $\mu_0 = 4\pi\cdot 10^{-7}$ N/A^2 is the permeability of free space. l_ex is also a measure of the length scale at which the exchange interaction usually dominates the magnetic behavior over the demagnetizing energy. For iron (Fe) $l_\mathrm{ex}^\mathrm{Fe} \approx 3.3$ nm and for permalloy $l_\mathrm{ex}^\mathrm{Py} \approx 5.7$ nm.

2.1.2 Demagnetizing energy

As one of Maxwell's equations states $\nabla \mathbf{B} = 0$ and the magnetic induction is defined as $\mathbf{B} = \mu_0(\mathbf{H} + \mathbf{M})$, this implies

$$\nabla \mathbf{H} = -\nabla \mathbf{M}. \tag{2.5}$$

Thus the magnetization itself gives rise to the demagnetizing field $\mathbf{H}_{\text{dem}}$. Additionally Maxwell's equations indicate $\nabla \times \mathbf{H}_{\text{dem}} = 0$, hence the demagnetizing field can be written as the gradient of a magnetic scalar potential: $\mathbf{H}_{\text{dem}} = -\nabla\phi$. Using Eq. (2.5) this yields a differential equation (Poisson's equation)

$$\Delta\phi = \nabla M, \tag{2.6}$$

where Δ is the Laplace operator. Eq. (2.6) has the general solution for the case of no local boundary conditions

$$\phi(\mathbf{r}) = -\frac{1}{4\pi}\int d\mathbf{r}' \frac{\nabla' \cdot \mathbf{M}(\mathbf{r}')}{|\mathbf{r} - \mathbf{r}'|}. \tag{2.7}$$

The right side of Eq. (2.6) can be interpreted as effective magnetic charge. Finally this solution gives

$$\mathbf{H}_{\text{dem}} = -\frac{1}{4\pi}\int d\mathbf{r}' \nabla\nabla' \frac{1}{|\mathbf{r} - \mathbf{r}'|}\mathbf{M}(\mathbf{r}') = \int d\mathbf{r}' \hat{\mathbf{G}}(\mathbf{r}, \mathbf{r}')\mathbf{M}(\mathbf{r}'), \tag{2.8}$$

where $\hat{\mathbf{G}}(\mathbf{r}, \mathbf{r}')$ is defined as the Green's tensor. A discussion of the solution including boundary conditions is for instance given in [23]. $\mathbf{H}_{\text{dem}}$ can be imagined as if its sources are positive and negative magnetic charges located according to the orientation of $\mathbf{M}$. Although these charges have no physical existence, they offer a mathematical way to represent the demagnetizing field as [24]

$$\mathbf{H}_{\text{dem}} = \int dV' \frac{(\mathbf{r} - \mathbf{r}')\nabla\mathbf{M}}{|\mathbf{r} - \mathbf{r}'|^3} + \int dS' \frac{(\mathbf{r} - \mathbf{r}')\mathbf{M} \cdot \mathbf{n}}{|\mathbf{r} - \mathbf{r}'|^3}, \tag{2.9}$$

where the first term accounts for volume charges inside the magnetic material and the second term describes surface charges; $\mathbf{n}$ is a unit vector normal to the surface.

Assuming $\mathbf{H}_{\text{dem}}$ is known, the associated energy density can be calculated by integration over the sample volume V, reading

$$\epsilon_{\text{dem}} = -\frac{\mu_0}{2V}\int_V \mathbf{M} \cdot \mathbf{H}_{\text{dem}} dV. \tag{2.10}$$

For arbitrarily shaped samples the analytical determination of $\mathbf{H}_{\text{dem}}$ and $\mathbf{M}$ can be very complicated and numerical calculations are often necessary.

For a thin magnetic film, however, magnetic charges can be avoided if the film is magnetized in-plane [22]. Whereas if the magnetization is oriented out-of-plane

the demagnetizing field is simply given by $\mathbf{H}_{\text{dem}} = (0, 0, -M_\perp)$, with $M_\perp$ being the out-of-plane component of the magnetization vector. Using Eq. (2.10) the demagnetizing energy density for a thin magnetic film becomes

$$\varepsilon_{\text{dem}} = \frac{\mu_0}{2} M_\perp^2 = \frac{\mu_0}{2} M_S^2 \cos^2\Theta, \tag{2.11}$$

where Θ is the angle between $\mathbf{M}$ and the surface normal.

2.1.3 Magnetocrystalline anisotropy

The electron orbits are influenced by the crystal fields. Since in 3d transition metals the orbital moments are highly reduced, the magnetic moments are dominated by the spin angular momentum [25]. However, the small remaining orbital momentum still couples to the spin via spin-orbit coupling. This leads to a connection between the crystal field and magnetization, generating favored axes to which $\mathbf{M}$ tends to align parallel. This is known as magnetocrystalline anisotropy.

Assuming a simple cubic lattice the magnetocrystalline anisotropy can be obtained by a power series expansion of the energy density. Odd terms need to be dropped due to time inversion symmetry, which demands an equal energy if the magnetization direction is reversed. Hence, [24, 26]

$$\varepsilon_{\text{ani, cubic, bulk}} = K_4(m_x^2 m_y^2 + m_y^2 m_z^2 + m_x^2 m_z^2) + K_6 m_x^2 m_y^2 m_z^2 + ..., \tag{2.12}$$

where $\mathbf{m} = (m_x, m_y, m_z) = \mathbf{M}/M_S$ and K_4 and K_6 are four- and six-fold anisotropy constants describing the strength of the magnetocrystalline anisotropy in units of J/m^3. Considering only the first term in Eq. (2.12), the easy axes are $\langle 100 \rangle$ directions (for $K_4 > 0$) or $\langle 111 \rangle$ directions (for $K_4 < 0$) [27].

In the case of thin magnetic films the situation differs. Other than in bulk materials, the in-plane and out-of-plane anisotropy constants can be different. Due to epitaxial growth of the ferromagnetic film an additional in-plane and out-of-plane uniaxial anisotropy can be induced by the substrate, caused by lattice mismatch or hybridization. Hence Eq. (2.12) changes to [27]

$$\varepsilon_{\text{ani, cubic, film}} = -\frac{K_4^{\parallel}}{2}(m_x^4 + m_y^4) - \frac{K_4^{\perp}}{2} m_z^4 - K_U^{\perp} m_z^2 - K_U^{\parallel} \frac{(\hat{\mathbf{n}} \cdot \mathbf{M})^2}{M_S^2}, \tag{2.13}$$

where $K_4^{\parallel}$, $K_4^{\perp}$, $K_U^{\perp}$ and $K_U^{\parallel}$ are fourfold and uniaxial out-of-plane and in-plane anisotropy constants, respectively. $\hat{n}$ is a unit vector, pointing along the in-plane uniaxial direction.

The electronic potential experienced by surface (or interface) atoms can also influence the magnetocrystalline anisotropy. Due to the broken symmetry at the surface the spin-orbit interaction can be greatly enhanced, since the otherwise reduced orbital momentum becomes large. The contribution from surfaces and

interfaces can be added to the bulk anisotropy. For a film with one surface (S) and one interface (I) this leads to [28]

$$K_i = K_{i,bulk} + \frac{K_{i,S}}{d} + \frac{K_{i,I}}{d}, \tag{2.14}$$

where d is the film thickness and K_i with $i \in \{1, 2, 3, 4\}$ represents all anisotropy constants appearing in Eq. (2.13). As expected the anisotropy contributions from surfaces and interfaces become less important as the film thickness increases.

2.1.4 Zeeman energy

The last contribution appearing in Eq. (2.10) is the Zeeman energy density, which describes the interaction of $\mathbf{M}$ with an external field $\mathbf{H}_0$:

$$\varepsilon_{\text{zee}} = -\frac{\mu_0}{V} \int_V \mathbf{M} \cdot \mathbf{H}_0 \, dV. \tag{2.15}$$

In the case of an uniform magnetization Eq. (2.15) becomes zero for parallel alignment $\mathbf{H}_0 \parallel \mathbf{M}$.

2.2 Ferromagnetic resonance

This section discusses the time evolution of the magnetization vector when being excited out of the equilibrium state. The equilibrium state is assumed if $\mathbf{M} \parallel \mathbf{H}_{\text{eff}}$. The effective field $\mathbf{H}_{\text{eff}}$ is defined as the functional derivative of the total energy density introduced in Eq. (2.1) [22]

$$\mathbf{H}_{\text{eff}} = -\frac{\delta \varepsilon_{\text{tot}}}{\delta \mathbf{M}}, \tag{2.16}$$

hence it accounts for internal and external fields. In practice a perturbation in terms of a time dependent magnetic field h_{rf} can be used to force $\mathbf{M} \nparallel \mathbf{H}_{\text{eff}}$. In order to achieve ferromagnetic resonance the driving frequency should typically be in the range of gigahertz (GHz). Besides the frequency also an external field $\mathbf{H}$ can be used to tune the conditions for FMR. This can be understood qualitatively, since $\mathbf{H}$ provides an additional magnetic stiffness. The same kind of stiffness is introduced intrinsically if magnetic anisotropies are present in the system. Alignment of $\mathbf{M}$ parallel to an easy axis (hard axis) consequently leads to a higher (lower) resonance frequency.

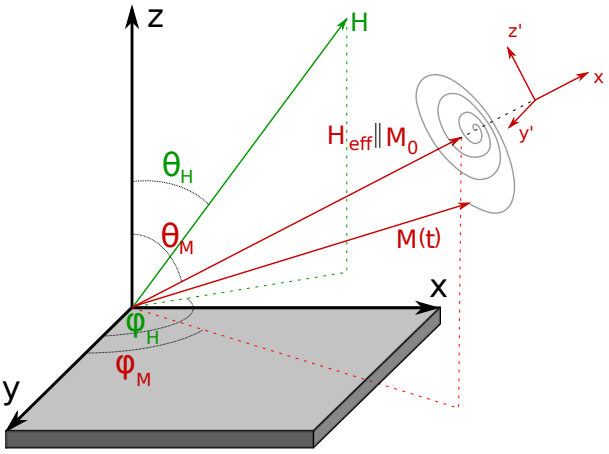

Figure 2.1: Illustration of the spiral motion of $\mathbf{M}$ around $\mathbf{H}_{\text{eff}}$. Both, the externally applied field $\mathbf{H}$ and $\mathbf{M}$ can be represented in a spherical coordinate system using the angles (θ_H, φ_H) and (θ_M, φ_M), respectively. The coordinate system $(\mathrm{x}', \mathrm{y}', \mathrm{z}')$ is chosen such that $\mathrm{x}' \parallel \mathbf{M}_0$ and $\mathrm{y}' \parallel \mathrm{y}$.

2.2.1 Landau-Lifshitz-Gilbert equation

A quantitative description of the dynamical evolution of the magnetization vector can be obtained using the Landau-Lifshitz-Gilbert (LLG) equation, reading

$$\frac{\partial \mathbf{M}}{\partial t} = -\gamma \mathbf{M} \times \mu_0 \mathbf{H}_{\text{eff}} + \frac{\alpha}{M_S} \mathbf{M} \times \frac{\partial \mathbf{M}}{\partial t}, \tag{2.17}$$

where $\gamma = \frac{eg}{2m_e}$ is the gyromagnetic ratio and α is the empirical Gilbert damping constant [29, 30]. The precessional motion of the magnetization vector is described by the first term of Eq. (2.17). The second term on the right hand side accounts for energy dissipation in the system and is called damping term. It exerts a torque which forces $\mathbf{M}$ to acquire the equilibrium orientation parallel to the effective field $\mathbf{H}_{\text{eff}}$. During the relaxation process the amplitude of $\mathbf{M}$ is preserved, leading to a trajectory where the tip of the magnetization vector is moving on a spherical surface. The spiral motion is schematically depicted in Fig. 2.1. To account for more complex circumstances like the interaction of $\mathbf{M}$ with spin polarized currents, additional torques must be added to the LLG equation [31]. In the following subsections the coordinate system and angles introduced in Fig. 2.1 are used.

2.2.2 Resonance conditions and magnetic susceptibility

This subsection summarizes the calculations performed in [22, 32].

Ferromagnetic resonance experiments basically measure the absorbed power of an alternating microwave field $\mathbf{h}_{\text{f}} = (h'_{\text{x}}, h'_{\text{y}}, h'_{\text{z}})$ by the magnetic moments of a specimen. The absorption can be obtained by detecting the transmitted power through, for

instance, a coplanar wave guide (CPW). The absorption is linked to the Zeeman energy of H_0 and $\mathbf{h}_\mathrm{f}$ via

$$\Delta E = \int -\mu_0(\mathbf{H}_0 + \mathbf{h}_\mathrm{f}) d\mathbf{m} = -\int_0^T dt \mu_0(\mathbf{H}_0 + \mathbf{h}_f)\frac{d\mathbf{m}}{dt}, \tag{2.18}$$

where a time average over a full oscillation period T yields the absorbed power [31]

$$P = \frac{\Delta E}{T} = \frac{1}{2}\mu_0 M_\mathrm{S}\omega\left(\chi''_{\mathrm{y'y'}} h^2_{\mathrm{y'}} + \chi''_{\mathrm{z'z'}} h^2_{\mathrm{z'}}\right), \tag{2.19}$$

with ω being the excitation frequency and $\chi_\mathrm{y} = \chi'_\mathrm{y} + i\chi''_\mathrm{y}$ and $\chi_\mathrm{z} = \chi'_\mathrm{z} + i\chi''_\mathrm{z}$ define the y and z components of the imaginary part of the magnetic susceptibility. Ferromagnetic resonance occurs when Eq. (2.19) is maximal, i.e. the imaginary part of the susceptibility has a maximum. In the following an expression of χ''_y for the in-plane configuration, as well as resonance conditions for in-plane and out-of-plane configurations are derived.

Since only ultrathin films are considered in this thesis, it is assumed that the radio frequency microwave field is constant throughout the sample thickness. This assumption is justified, because the skin depth $\delta = (2/\mu_0\mu_r\omega\sigma)^{1/2}$, where σ is the conductivity and μ_r is the relative magnetic permeability, is usually larger than 10^{-7} m. Furthermore the magnetic moments are collectively treated in the macrospin approximation (see section 1.1). Furthermore the equilibrium orientation of the magnetization vector in the (x′,y′,z′) coordinate system is defined as $\mathbf{M}_0 = (M_\mathrm{S}, 0, 0)$ and only small deviations in the y′ and z′ directions, such that $M_{\mathrm{x'}} = (M_\mathrm{S}^2 - m^2_{\mathrm{y'}} - m^2_{\mathrm{z'}})^{1/2} \approx M_\mathrm{S}$, are considered.

In-plane configuration

In the following the applied dc field $\mathbf{H}$ is parallel to the sample surface ($\theta_\mathrm{H} = 90°$) and $\mathbf{h}_\mathrm{f}$ is directed perpendicularly to $\mathbf{M}_0$, along the y′ axis. Therefore the effective magnetic field entering the LLG equation is given by

$$\mathbf{H}_\mathrm{eff} = \mathbf{H}_\mathrm{ani} + \mathbf{H}_\mathrm{dem} + H_0\cos(\varphi_\mathrm{H} - \varphi_\mathrm{M})\hat{x}' + h_0\hat{y}'. \tag{2.20}$$

Assuming a time variation of $\exp(-i\omega t)$ and taking only first order terms of $m_{\mathrm{y'}}$ and $m_{\mathrm{z'}}$ into account, linearization of the LLG equation yields:

$$i\frac{\omega}{\gamma}m_{\mathrm{y'}} + \left(\mathscr{B} + \alpha\frac{i\omega}{\gamma}\right)m_{\mathrm{z'}} = 0, \tag{2.21}$$

$$\left(\mu_0\mathscr{H} + \alpha\frac{i\omega}{\gamma}\right)m_{\mathrm{y'}} - i\frac{\omega}{\gamma}m_{\mathrm{z'}} = \mu_0 M_s h_0, \tag{2.22}$$

where

$$\begin{aligned}\mathscr{B} =&\mu_0 H_0 \cos(\varphi_\mathrm{H}-\varphi_\mathrm{M}) + \mu_0 M_\mathrm{S} - \frac{2K_\mathrm{U}^{\perp}}{M_\mathrm{S}} + \frac{K_4^{\parallel}}{2M_\mathrm{S}}[3+\cos(4\varphi_\mathrm{M})]+\\ &+\frac{K_\mathrm{U}^{\parallel}}{M_\mathrm{S}}[1+\cos(2(\varphi_\mathrm{M}-\varphi_\mathrm{easy}))],\\ \mu_0\mathscr{H} =&\mu_0 H_0 \cos(\varphi_\mathrm{H}-\varphi_\mathrm{M}) + \frac{2K_4^{\parallel}}{M_\mathrm{S}}\cos(4\varphi_\mathrm{M}) + \frac{2K_\mathrm{U}^{\parallel}}{M_\mathrm{S}}\cos(2(\varphi_\mathrm{M}-\varphi_\mathrm{easy})),\end{aligned} \tag{2.23}$$

are the effective magnetic induction and the effective magnetic field, respectively. The angle φ_easy defines the preferred uniaxial in-plane axis. A detailed derivation for this expression can for instance be found in [33]. The associated uniaxial energy reads

$$E_\mathrm{U} = -K_\mathrm{U}^{\parallel}\cos^2(\varphi_\mathrm{M}-\varphi_\mathrm{easy}). \tag{2.24}$$

Inserting Eq. (2.21) into Eq. (2.22) the linear susceptibility reads:

$$\chi_{\mathrm{y}'} = \frac{m_{\mathrm{y}'}}{h_{\mathrm{y}'}} = \frac{\mu_0 M_\mathrm{S}\left(\mathscr{B}+i\alpha\frac{\omega}{\gamma}\right)}{\left(\mathscr{B}+i\alpha\frac{\omega}{\gamma}\right)\left(\mu_0\mathscr{H}+i\alpha\frac{\omega}{\gamma}\right)-\left(\frac{\omega}{\gamma}\right)^2}. \tag{2.25}$$

The corresponding resonance condition can be obtained by maximizing the imaginary part of Eq. (2.25). Thus, setting the denominator to zero and ignoring the damping ($\alpha = 0$) yields the general resonance condition

$$\left(\frac{\omega}{\gamma}\right)^2 = \mu_0\mathscr{B}\mathscr{H}\,|_{H_0=H_\mathrm{FMR}}\,. \tag{2.26}$$

The samples investigated in this thesis usually exhibit a damping α in the range of $10^{-3}-10^{-4}$, which justifies the approximation of neglecting terms with α in Eq. (2.26). In general, for FMR measurements conducted on permalloy the applied field H_0 is rather large compared to in-plane anisotropies. This assures M_S to be almost aligned parallel to H_0 ($\varphi_\mathrm{H} \approx \varphi_\mathrm{M}$). Inserting Eq. (2.23) into Eq. (2.26) and neglecting in-plane anisotropies provides a resonance condition for a fully in-plane saturated magnetic film

$$\left(\frac{\omega}{\gamma}\right)^2 = \mu_0 H_\mathrm{FMR}(\mu_0 H_\mathrm{FMR} + \mu_0 M_\mathrm{eff}). \tag{2.27}$$

This equation is known as the famous Kittel formula [34]. In Eq. (2.27) the effective magnetization M_eff is defined as

$$\mu_0 M_\mathrm{eff} = \mu_0 M_\mathrm{S} - \frac{2K_\mathrm{U}^{\perp}}{M_\mathrm{S}}. \tag{2.28}$$

Out-of-plane configuration

In the perpendicular configuration the external field H_0 and the magnetization $\mathbf{M}$ are oriented perpendicularly to the magnetic film. The four-fold as well as the uniaxial in-plane anisotropies are neglected for this case. Hence Eq. (2.23) can be rewritten as [33]

$$\begin{aligned}\mathscr{B} =&\mu_0 H_0 \cos(\theta_\mathrm{H} - \theta_\mathrm{M}) - \mu_0 M_\mathrm{eff} \cos^2\theta_\mathrm{M} + \frac{2K_4^\perp}{M_\mathrm{S}} \cos^4\theta_\mathrm{M},\\ \mu_0\mathscr{H} =&\mu_0 H_0 \cos(\theta_\mathrm{H} - \theta_\mathrm{M}) - \mu_0 M_\mathrm{eff} \cos 2\theta_\mathrm{M} + \frac{2K_4^\perp}{2M_\mathrm{S}} (\cos 4\theta_\mathrm{M} + \cos 2\theta_\mathrm{M}),\end{aligned} \tag{2.29}$$

where $K_4^\perp$ is the four-fold out-of-plane anisotropy constant. Using the resonance condition of Eq. (2.26) and applying $\theta_\mathrm{M} = \theta_\mathrm{H} = 0$ leads to

$$\frac{\omega}{\gamma} = \mu_0 H_\mathrm{FMR} - \mu_0 M_\mathrm{eff} + \frac{2K_4^\perp}{M_\mathrm{S}}. \tag{2.30}$$

Susceptibility and FMR lineshape

The FMR lineshape for the in-plane configuration discussed above is addressed in the following. When assuming only small deviations from the resonance field H_FMR the imaginary part of Eq. (2.25) can be expressed as

$$\chi_\mathrm{y}'' = \frac{\mathscr{B} M_\mathrm{S}}{\mathscr{B} + \mu_0 \mathscr{H}}\Big|_{H_\mathrm{FMR}} \frac{\Delta H}{\Delta H^2 + (H_0 - H_\mathrm{FMR})^2}, \tag{2.31}$$

where the first part is evaluated at the resonance field H_FMR and $\Delta H = \alpha\frac{\omega}{\gamma}$ is the half width at half maximum linewidth (HWHM). Eq. (2.31) reveals the lineshape of a FMR-measurement to be in good approximation a Lorentzian, as long as $\mathscr{H} \gg \Delta H$ close to $H = H_\mathrm{FMR}$. Finally a typical FMR measurement is discussed. Two major differences to the ideal case can be identified:

First, two-magnon scattering and magnetic layer inhomogeneities may be present. Two-magnon scattering is a process where the uniform FMR mode scatters into spin waves ($\mathbf{k} \neq 0$) with equal frequency (compare Fig. 2.2). The second parasitic effect can appear, for example if the layer thickness is not constant. Both effects lead to extrinsic losses during FMR and to an increased linewidth [22]

$$\mu_0 \Delta H = \mu_0 \Delta H(0) + \alpha\frac{\omega}{\gamma}, \tag{2.32}$$

where $\Delta H(0)$ is a zero frequency offset to the linewidth and is usually on the order of mT.

Second, the measured absorption may not purely be Lorentzian. This is because the magnetic sample and the waveguide may couple to each other. During FMR the Q-factor of the waveguide can vary, changing the absorbed and dissipated power. A

mixture of symmetric and asymmetric lineshapes can also occur when the dynamic magnetization is sampled by means of stroboscopic techniques (see section 3.4), where a phase between the sampling frequency and h_f may arise. Both cases result in a mixture of real and imaginary parts of the susceptibility. Hence, the fitting function for the absorption becomes:

$$P \sim \chi'_\mathrm{y}\cos(\varepsilon) + \chi''_\mathrm{y}\sin(\varepsilon) \sim \frac{\Delta H\cos(\varepsilon) + (H - H_\mathrm{FMR})\sin(\varepsilon)}{\Delta H^2 + (H_0 - H_\mathrm{FMR})^2}, \tag{2.33}$$

where ε is the mixing angle between dispersive and absorptive components [35]. Eq. (2.33) provides accessibility to all important parameters by performing angle and frequency dependent measurements. Thereby ΔH is related to the damping and the quality of the magnetic film via Eq.(2.32) and the resonance field H_FMR is related to magnetic anisotropies and the gyromagnetic ratio γ via Eq.(2.26).

2.3 Spin waves

In this section the former applied macrospin approximation is dropped. Neighboring spins thus are allowed to exhibit a relative phase during oscillations. This leads to the appearance of non-uniform excitations called spin waves. Since many properties of spin waves have quasi particle character, they are often called magnons. Spin waves can be created by local magnetic rf fields induced, for instance, by rf currents. The magnons subsequently travel away from the region of excitation and can be guided through structured spin wave channels [36]. A property that led to the idea of utilizing spin waves as information carriers.

2.3.1 Dispersion relation

The constitutive energies, dictating the spin wave characteristics, are the exchange interaction and dipolar energies. The exchange energy becomes dominant for short wavelengths λ (large wave vectors k), since tilting angles between neighboring spins are large. In contrast, for small wave vectors the dipolar interactions are most relevant. In the following only magnons with $\mathbf{k}$-vectors in the film plane and a homogeneous profile throughout the sample thickness are considered. This approximation is valid for thin magnetic films, were the exchange length introduced in Eq. (2.4) is of the order of the film thickness d.

To obtain the eigenfrequencies of spin waves in thin infinitely wide films Kalinikos and Slavin developed a formalism using tensorial Greens functions, as introduced in Eq. (2.8), to account for the dynamical dipolar fields arising from non-homogeneous wave profiles [37]. After linearization of the LLG (compare with the previous section), the differential exchange interaction is treated as a perturbation in order to

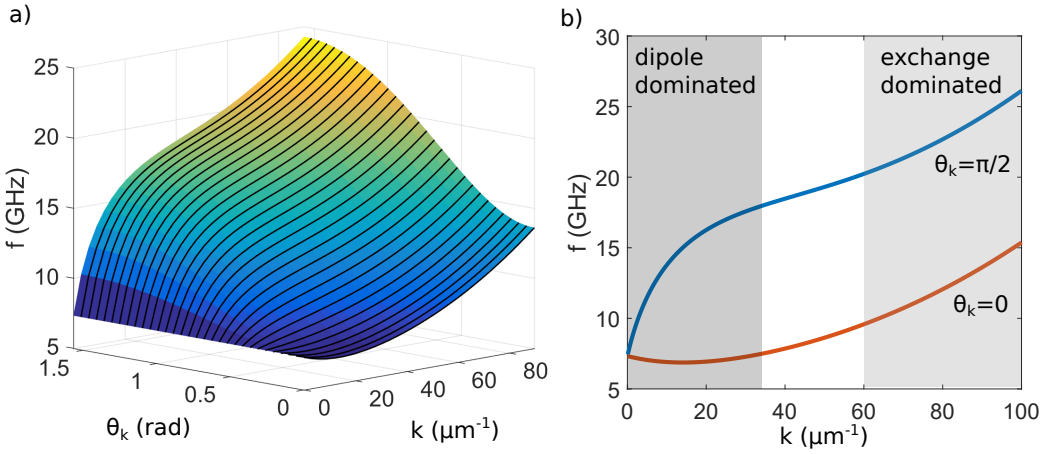

Figure 2.2: a) Calculated spinwave dispersion according to Eq. (2.34) with the parameters: $\mu_0 H = 0.06$ T, $A = 1.6 \cdot 10^{-11}$ J/m, $\mu_0 M_S = 1.08$ T and $d = 40$ nm. The angle between the magnetization and the spin wave propagation direction is denoted as θ_k. FMR is obtained at 7.3 GHz for $k = 0$ independent of θ_k. b) Shows the important cases of backward volume ($\theta_k = 0$) and Damon-Eshbach ($\theta_k = \pi/2$) spin waves. The shaded areas highlight the regions for which the dipole or the exchange contribution are dominant.

obtain solutions of the LLG. A detailed calculation can be found in [37]. Without considering anisotropies the dispersion relation is derived as

$$f(\theta_k, k) = \frac{\gamma}{2\pi}\sqrt{\left(\mu_0 H + \frac{2A}{M_S}k^2\right)\left(\mu_0 H + \frac{2A}{M_S}k^2 + \mu_0 M_S F_{00}\right)}, \tag{2.34}$$

with

$$F_{00} = 1 - P_{00}\cos^2\theta_k + P_{00}(1 - P_{00})\frac{\mu_0 M_S}{H + \frac{2A}{M_S}k^2}\sin^2\theta_k \tag{2.35}$$

and

$$P_{00} = 1 - \frac{1 - \exp(-kd)}{kd}, \tag{2.36}$$

where f is the frequency of the wave and θ_k is the angle between k and the static magnetization orientation [38]. Since anisotropies are neglected for the considered system and the external field is applied in-plane, the magnetization is always parallel to the external field H. Eq. (2.34) shows, that a spin wave dispersion is inherently anisotropic. For parallel alignment ($\theta = 0°$) the magnons are called backward volume (BV) waves and in the perpendicular configuration ($\theta = 90°$) they are denoted Damon-Eshbach waves. Fig. (2.2) displays Eq. (2.34) for various angles θ_k. Detailed description of the material parameters used for the calculation, can be found in the caption of Fig. 2.2.

As can be seen in the calculations, DE waves are characterized by a purely positive slope. DE spin waves are also called surface modes, since their amplitude decreases exponentially into the volume of the magnetic material. This feature, however, can be neglected for thin films with a thickness in the range of tens of nanometers. In

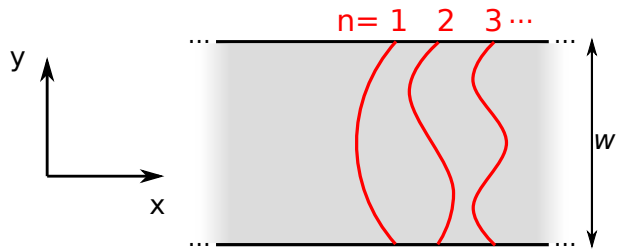

Figure 2.3: Illustration of confined spin waves ($n = 1, 2, 3, \dots$) in an infinitely long stripe of width w. The coordinate system defines the direction parallel (x) and perpendicular (y) to the stripes length.

contrast, BV modes exhibit a constant amplitude throughout the volume and show a negative slope for small values of k. Hence, in this small region the group velocity, given by $\partial\omega/\partial k$ is also negative. Besides the different sign of the group velocities, also the magnitude of the slope for DE and BV modes differs. In the case of DE modes the slope is much larger (compare Fig. 2.2b). This means for equal magnetic damping spin waves travel a larger distance from the region of excitation. This behavior is in general advantageous for the detection and characterization of spin waves in experiments.

For large values of k the exchange interaction term $(2A/M_S)k^2$ in Eq. (2.34) is dominant and the dispersion increases quadratically with k. This region is highlighted gray in Fig. (2.2) and named exchange dominated. In contrast, for small values of $\mathbf{k}$ the spin waves are dipole dominated and their behavior depends on the orientation of $\mathbf{k}$ and $\mathbf{M}$. In case $k = 0$, Eq. (2.34) transforms into the Kittel formula introduced in Eq. (2.27).

2.3.2 Confinement and excitation efficiency

This section is dedicated to briefly overview the effects of confinement and excitation efficiency. A detailed analysis can be found in [39]. In the following an infinitely long stripe with width w and thickness d is considered (see Fig. 2.3). The direction parallel and perpendicular to the stripe is denoted x and y, respectively. To begin with, the magnetization is directed along the x-axis, while the confinement of the spin waves is in the y direction. This leads to a DE geometry since $\mathbf{M} \perp \mathbf{k}$. For this case the problem is one dimensional and can be solved under the restriction $d/w \ll 1$. Yielding a discrete set of eigenfrequencies [31]

$$f_n = \frac{\gamma}{2\pi}\sqrt{\mu_0 H(\mu_0 H + \mu_0 M_S) + \frac{\pi}{4}(\mu_0 M_S)^2(2n-1)\frac{d}{w}}, \quad n = 1, 2, 3, \dots \tag{2.37}$$

were the number of nodes is denoted n. Each node located at a boundary of the stripe is evaluated as 1/2. The first mode ($n = 1$) is comparable to the FMR mode in a full film, but slightly shifted upwards in frequency, according to Eq. (2.37). In general, the higher the order n, the higher the eigenfrequency of the mode. The

distance between neighboring modes depends on the ratio d/w. Assuming d to be constant, a decreasing value w leads to a larger separation in the frequency spectrum. Whereas an increasing value w shifts the modes closer together, eventually making the distinction between modes difficult if the linewidths are sufficiently large.

In the following an external field is utilized to force the magnetization perpendicular to the stripes long axis (y-direction). Hence $\mathbf{M} \parallel \mathbf{k}$ and the BV geometry is realized. In this case no simple analytic formula exists to obtain the eigenfrequencies and calculations have to be numerically performed. This is mainly because of the complex internal fields emerging due to the dynamic wave profile. Additionally, due to inhomogeneities of the internal field at the boundaries of the stripe, additional solutions, called edge modes, can appear. These modes are usually located at lower frequencies for higher orders of n. Since the dispersion relation for BV modes exhibits a small slope, the BV modes show a much smaller separation in frequency compared to the case of DE spin waves. Furthermore the frequency decreases for higher order modes because of the negative sign of the slope.

Finally the excitation efficiency ϵ_{SW} is addressed. Various types of antennas enable efficient excitation of different wave vectors. Hence the dimensions of the antenna must be chosen according to the wave vector range of interest. The efficiency is determined by the overlap integral of the excitation field $h(x)$ and the mode profile $q(x,k)$ [31],

$$\epsilon_{\mathrm{SW}} \sim \int_0^{\frac{2\pi}{k}} dx h(x) q(x,k), \tag{2.38}$$

where $q(x,k) \sim \cos(\omega t - kx)$ for plane waves. Application of a homogeneous excitation can therefore not excite traveling spin waves in an infinite film, but is able to excite symmetric standing wave patterns ($n = 1, 3, \dots$) in a confined structure.

2.3.3 Spin wave dispersion for cylindrical nanotubes

This section follows the work presented in [8]. The spin wave dispersion of an infinitely long cylindrical NT is derived in the following to outline the significant differences to full film magnetic layers discussed previously. The magnetic moments of the NT are excited with radio frequency as depicted in Fig. 2.4. As the magnetic ground state may not be a vortex state for a given tubular geometry (see [10]) a current flowing in the non-magnetic core of the NT can be applied, creating an Oersted field referred to as $\mathbf{h}_0 = \mathbf{H}_0/M_{\mathrm{S}}$, which can stabilize the vortex state above a critical field denoted H_{crit}. In the following small perturbations $\mathbf{m}$ (i.e. $|\mathbf{m}| \ll 1$) perpendicular to the equilibrium vortex state (denoted $\mathbf{M}_0$) are considered:

$$\mathbf{m} = \rho m_\rho + z m_{\mathrm{z}}, \tag{2.39}$$

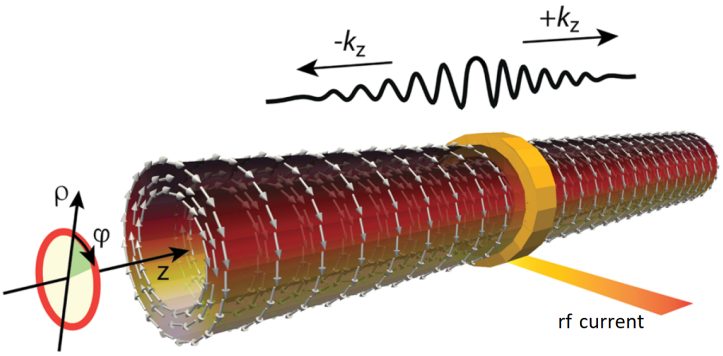

Figure 2.4: Illustration of the circular nanotube and the polar coordinate system. The vortex state can be set by applying a current in the tubes non-magnetic core parallel to its axis. The rf excitation introduces spin waves which are able to propagate in the positive and negative z-direction. For both $\mathbf{k} \perp \mathbf{M}$ holds. Taken from [8].

where the directions are introduced in Fig. 2.4. In order to obtain the dynamical equations the LLG (Eq. (2.17)) is linearized to the first order of $\mathbf{m}$. For the analytical model exchange, dipole and Zeeman (related to the circular field $\mathbf{h}_0$) energy terms are considered in the framework of micromagnetic continuum-theory. Consequently the effective field introduced in Eq. (2.16) becomes

$$\mathbf{H}_{\text{eff}} = \mathbf{H}_{\text{ex}} + \mathbf{H}_{\text{dem}} + \mathbf{h}_0. \tag{2.40}$$

Linearization can be conducted by expanding these contributions in terms of the linear excitation $\mathbf{m}$. Hence the exchange and dipole interaction are expressed as

$$\mathbf{H}_{\text{ex}} \approx \mathbf{H}^0_{\text{ex}} + \mathbf{h}_{\text{ex}}, \tag{2.41}$$

$$\mathbf{H}_{\text{dem}} \approx \mathbf{H}^0_{\text{dem}} + \mathbf{h}_{\text{dem}}, \tag{2.42}$$

where $\mathbf{H}^0_{\text{ex}} = l^2_{\text{ex}} M_S \nabla^2 \mathbf{M}$ and $\mathbf{H}^0_{\text{dem}} = 0$ are the associated exchange and dipolar fields to the vortex state, respectively. Furthermore the linear perturbations are $\mathbf{h}_{\text{ex}} = l^2_{\text{ex}} M_S \nabla^2 \mathbf{m}$ and $\mathbf{h}_{\text{dem}} = \hat{\rho}(h_{\text{dem}})_\rho + \hat{\varphi}(h_{\text{dem}})_\varphi + \hat{z}(h_{\text{dem}})_z = -\nabla\Phi$, where $(h_{\text{dem}})_\rho = -\partial_\rho \Phi$, $(h_{\text{dem}})_\varphi = -(1/\rho)\partial_\varphi \Phi$ and $(h_{\text{dem}})_z = -\partial_z \Phi$. The dynamic dipolar potential is generated by the excitation and reads (compare section 2.1.2)

$$\Phi = \int_V d^3\mathbf{r} \frac{\rho_V}{|\mathbf{r} - \mathbf{r}'|} + \oint_S dS \frac{\sigma_S}{|\mathbf{r} - \mathbf{r}'|}, \tag{2.43}$$

where the dynamical volume and surface charge densities are

$$\rho_V = -\frac{M_S}{4\pi} \nabla \cdot \mathbf{m}, \tag{2.44}$$

$$\sigma_S = \frac{M_S}{4\pi} \mathbf{m} \cdot \hat{n}, \tag{2.45}$$

respectively. $\hat{n}$ denotes the surface normal unit vector. Finally, linearization of the undamped LLG ($\alpha = 0$) with the fields given by Eq. (2.41) and Eq. (2.42) and

averaging over the NTs cross-section yields the dynamic equations for the excitation components of $\mathbf{m}$:

$$\dot{m}_\rho = \gamma\mu_0 M_\mathrm{S}\left(-l_\mathrm{ex}^2\left(\frac{1}{b^2}+\nabla^2\right)m_z + h_0 m_z + \frac{1}{M_\mathrm{S}}\langle h_\mathrm{dem}\rangle_z\right), \tag{2.46}$$

$$\dot{m}_z = \gamma\mu_0 M_\mathrm{S}\left(l_\mathrm{ex}^2\nabla^2 m_\rho - h_0 m_\rho + \frac{1}{M_\mathrm{S}}\langle h_\mathrm{dem}\rangle_\rho\right), \tag{2.47}$$

where $\langle h_\mathrm{dem}\rangle_i = 2/(R^2-r^2)\int_r^R d\rho(h_\mathrm{dem})_i$ with $i=\rho$, z and $b^{-2} = 2\ln(R/r)/(R^2-r^2)$ with R and r being the outer and inner radii, respectively. In order to extract the spin wave dispersion from Eq. (2.46) and Eq. (2.47) knowledge of the excitation is necessary. Due to the azimuthal symmetry and the infinitely long tube any occurring oscillations can be described by a wave vector k_z and an integer wave number n to account for the azimuthal oscillation phase along φ. The excitation is thus rewritten as Fourier expansion of the components of $\mathbf{m}$ reading

$$m_z(\varphi,z,t) = \sum_{n=-\infty}^{\infty}\int_{-\infty}^{\infty} Z_n(k_\mathrm{z})e^{ik_\mathrm{z}z}e^{in\varphi}e^{-i\omega t}dk_\mathrm{z}, \tag{2.48}$$

$$m_\rho(\varphi,z,t) = \sum_{n=-\infty}^{\infty}\int_{-\infty}^{\infty} R_n(k_\mathrm{z})e^{ik_\mathrm{z}z}e^{in\varphi}e^{-i\omega t}dk_\mathrm{z}, \tag{2.49}$$

where ω is the frequency and $R_n(k_\mathrm{z})$ and $Z_n(k_\mathrm{z})$ are the Fourier amplitudes. Using this ansatz, Eq. (2.46) and Eq. (2.47) yield a set of equations in terms of $R_n(k_\mathrm{z})$ and $Z_n(k_\mathrm{z})$, whose eigenvalues correspond to the dispersion relation

$$\frac{\omega_n(k_\mathrm{z})}{\gamma\mu_0 M_\mathrm{S}} = \mathcal{K}_n(k_\mathrm{z}) + \sqrt{\mathcal{A}_n(k_\mathrm{z})\mathcal{B}_n(k_\mathrm{z})}, \tag{2.50}$$

where

$$\mathcal{A}_n(k_\mathrm{z}) = l_\mathrm{ex}^2\left(\frac{n^2-1}{b^2}+k_\mathrm{z}^2\right) + h_0 + \mathcal{L}_n(k_\mathrm{z}), \tag{2.51}$$

$$\mathcal{B}_n(k_\mathrm{z}) = l_\mathrm{ex}^2\left(\frac{n^2}{b^2}+k_\mathrm{z}^2\right) + h_0 + \mathcal{J}_n(k_\mathrm{z}). \tag{2.52}$$

The functions $\mathcal{J}$, $\mathcal{K}$ and $\mathcal{L}$ are given by

$$\mathcal{J}_n(k_\mathrm{z}) = \frac{\pi}{S}\int_0^\infty dk\frac{k^3}{2(k^2+k_\mathrm{z}^2)}\left(\Lambda_{n-1}(k)-\Lambda_{n+1}(k)\right)^2, \tag{2.53}$$

$$\mathcal{K}_n(k_\mathrm{z}) = \frac{\pi}{S}\int_0^\infty dk\frac{k^2 k_\mathrm{z}}{k^2+k_\mathrm{z}^2}(\Lambda_{n-1}(k)-\Lambda_{n+1}(k))\Lambda_n(k), \tag{2.54}$$

$$\mathcal{L}_n(k_\mathrm{z}) = \frac{\pi}{S}\int_0^\infty dk\frac{2kk_\mathrm{z}^2}{k^2+k_\mathrm{z}^2}(\Lambda_n(k))^2, \tag{2.55}$$

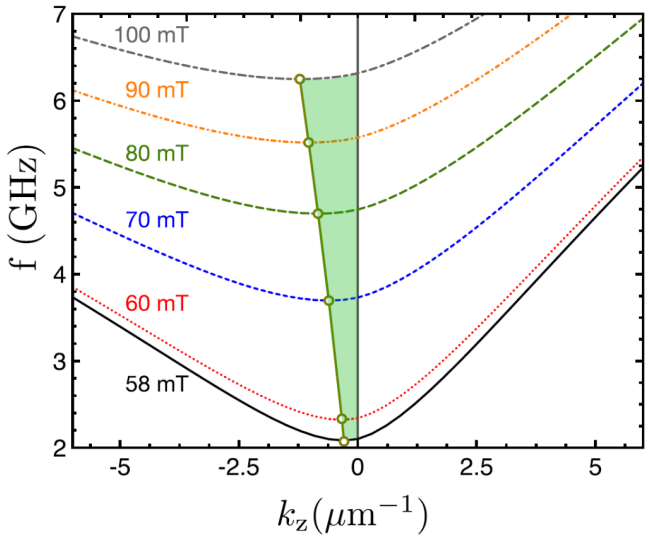

Figure 2.5: Dispersion relation calculated from Eq. (2.50) with $R = 30$ nm and $r = 20$ nm for different circular fields $\mathbf{h}_0$. The asymmetry with respect to $k_z = 0$ increases with larger circular fields. The open dots represent the minima for each field value, hence within the green shaded area the group velocity is negative. Image taken from [8].

with $\Lambda_n(k) = \int_r^R d\rho\rho J_n(k\rho)$ and $J_n(x)$ being the Bessel-functions of the first kind of order n and $S = \pi(R^2 - r^2)$ is the nanotubes cross section area. Since none of the interactions considered in Eq. (2.40) are able to mix oscillations of different numbers k_z and n in the dispersion relation, a set of values $(k_z, n, \omega_n(k_z))$ can be associated with a magnon. The special case of homogeneously distributed spin wave excitations along the angle φ is achieved for $n = 0$. Eq. (2.50) is plotted exemplary for $r = 20$ nm and $R = 30$ nm and varying circular fields in Fig. 2.5. As can be seen the spin wave dispersion shows an asymmetry with respect to the direction of propagation. This in turn induces a range of k_z values for which the group velocity is negative (green area in Fig. 2.5). The asymmetry, decreases with increasing tube diameter, eventually reaching the thin film limit at infinite diameters.

The origin of this asymmetric behavior can be traced back to Eq. (2.54), since $\mathcal{K}_0(k_z)$ is the only odd function in k_z appearing in Eq. (2.50). It solely comprises dynamic dipolar energy terms arising from surface and volume charges created by the propagating spin waves. The volume charges averaged over the nanotubes radius $\langle \rho_V \rangle = \langle \rho_V \rangle_0 e^{i(k_z z - \omega t)}$ with

$$\langle \rho_V \rangle_0 = -\frac{M_S^2}{4\pi} \Bigg(\underbrace{\frac{2}{r+R}}_{\text{I}} + \underbrace{k_z \sqrt{\frac{\mathcal{B}_0(k_z)}{\mathcal{A}_0(k_z)}}}_{\text{II}} \Bigg) \left(1 + \frac{\mathcal{B}_0(k_z)}{\mathcal{A}_0(k_z)} \right)^{-\frac{1}{2}}, \tag{2.56}$$

are proportional to two terms labeled I and II. Since II depends on k_z also the sum of I and II must depend on the direction of propagation. Consequently the volume

charges are different for positive and negative values of k_z. Hence also the dipolar energies have to differ. However, as the excitation is usually fixed at a defined frequency, the energy distribution in both directions should be equal. This can only be achieved if the wavelengths for both propagation directions differ such that the dynamic dipolar energy adjusts the surface and volume charges to be energetically equal. Hence the asymmetry is solely a dipolar effect, created due to the curvature of the nanotube.

2.4 Domain walls in magnetic nanotubes

This section introduces the typical types of domain walls found in magnetic bulk systems, flat stripes and nanotubes.

The formation of domains is provoked by the reduction of stray field energy. At the cost of exchange energy systems can form domain walls which separate regions of uniform magnetization. The most famous types of domain walls are Bloch and Néel walls, both illustrated in Fig. 2.6 a) and b), respectively. While for Bloch walls, the magnetic moments rotate in the plane of the domain wall, in the case of Néel walls the rotation is perpendicular to the plane. Hence, Bloch walls generate only stray fields at the surface of the material and not within the domain wall. Therefore Bloch walls are favored over Néel walls in bulk materials due to the large volume to surface ratio. As soon as this ratio is sufficiently reduced the situation changes and Néel type walls can be favored. This is usually the case if the exchange length is larger than the thickness t of the magnetic layer.

The domain wall width of a Bloch wall is usually defined as

$$\Delta_{\mathrm{DW}} = \pi l = \pi\sqrt{\frac{A}{K}}, \tag{2.57}$$

where l is the domain wall parameter and K is the anisotropy constant. Since the transition of the magnetization between domains is continuous, multiple definitions of the domain wall width exist [26]. As a rule of thumb the domain wall width can be illustrated as the distance between regions in which more than 91 % of the magnetization direction of the domains is acquired (this results by inserting $x = \pi l/2$ into Eq. 2.59).

In the following a coordinate system is defined, where x is the direction perpendicular to the domain wall plane and y and z are parallel to w and t, introduced in Fig. 2.6 a) - d), respectively. The usual Bloch wall profile can thus be expressed as [40]

$$m_z(x) = \frac{1}{\cosh(x/l)}, \tag{2.58}$$

$$m_y(x) = \tanh(x/l). \tag{2.59}$$

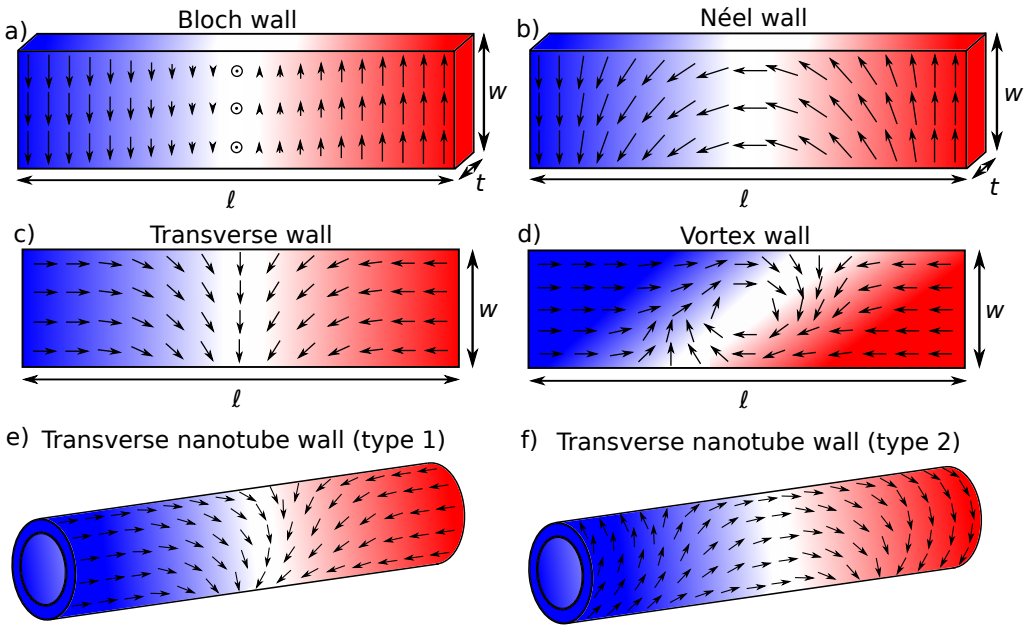

Figure 2.6: Illustration of the different types of domain walls. a) Bloch wall, the dominant wall type in bulk materials ($w \sim l \sim t$). b) Reduction of the t below the exchange length ($l, w \gg t$) can lead to Néel walls. In the case of a very long magnetic stripe ($l > w \gg t$) c) transverse or d) vortex walls are often found. Magnetic nanotubes usually exhibit transverse-like domain walls which avoid edge charges due to circular symmetry. e) Type 1 wall, found in uniform magnetized NTs. f) Type 2 wall, found if the NT is in a vortex state.

We now consider the case of magnetic nanostripes with $l > w \gg t$ and without crystalline anisotropies. Due to the magnetic shape anisotropy, the magnetization is generally aligned parallel to the length of the nanostripe. Introduction of a domain wall thus separates domains with magnetization pointing towards or away from each other. These structures are often referred to as head-to-head or tail-to-tail domain walls. Two typical types among these 180° domain walls are the transverse and the vortex wall, illustrated in Fig. 2.6 c) and d), respectively. Which of these types is lowest in energy was empirically found to be well described for permalloy stripes by [41]

$$w(t) = 128 \cdot \left(\frac{A}{\mu_0 M_S^2} \right)^2 \cdot \frac{1}{t}, \tag{2.60}$$

where the vortex domain wall is favored below the function $w(t)$. Eq. (2.60) reveals the dependence of the domain wall type on the thickness t and the width w of the stripe. The domain wall profile of a transverse wall is well described by the Bloch wall profile introduced in Eq. (2.58) and (2.59) if the width is parallel to the y-axis and the length of the stripe is parallel to the z-axis, respectively. In contrast the domain wall width of a Bloch type wall is not suitable for the description of

transverse and vortex walls, since the domain wall width is not constant along the stripe width. An average over the width w yields [41]

$$\Delta_{\mathrm{TW}} = w, \qquad \Delta_{\mathrm{VW}} = \frac{3\pi w}{4}, \tag{2.61}$$

for the transverse wall and the vortex wall, respectively.

Finally, the case of a magnetic nanotube is discussed. Depending on the diameter, length and magnetic layer thickness as well as on anisotropies a NT can either be in a uniform state or a vortex state. Introduction of a domain wall consequently leads to the appearance of type 1 or type 2 transverse domain walls, respectively (illustrated in Fig. 2.6 e) and f)). A NT can be described as a magnetic stripe with additional periodic boundary conditions at its long edges. Hence, magnetic charges of a transverse wall can be completely avoided and are the dominant type of domain walls. Simulations suggest a high wall stability if driven by an external field or current. This is due to the lack of boundaries, which are usually responsible for velocity limiting effects such as the Walker breakdown. At the same time the transverse nanotube walls exhibit a high mobility, allowing for large domain wall velocities at low applied current densities [9, 42]. The domain wall profiles can again be approximated well with Eq. (2.58) and (2.59).

It shall be mentioned that other forms and mixtures of the presented domain wall types exist (see for instance [26]). Their appearance is a result of the non-trivial interplay between stray fields and crystalline anisotropies.

2.5 Anisotropic magnetoresistance

The anisotropic magnetoresistance effect was first mentioned in 1857 by William Thomson. The AMR basically describes a resistance difference arising from the orientations of the electrical current $\mathbf{J}$ with respect to the magnetization $\mathbf{M}$ of a ferromagnetic sample. For $\mathbf{J} \parallel \mathbf{M}$ the resistance is usually a few percent higher than for $\mathbf{J} \perp \mathbf{M}$, in the case of bulk materials [43]. In the following 3d transition metals such as iron, nickel and cobalt with explicit itinerant character of the d-electrons are considered.

The main contribution to the resistivity comes from interband transitions since the density of states for d-electrons $N_{\mathrm{d}}(E_{\mathrm{F}})$ at the Fermi energy E_F is large and most of the current is carried by s-electrons [44]. The relaxation time is inversely proportional to $N_{\mathrm{d}}(E_{\mathrm{F}})$ and given by [45]

$$\frac{1}{\tau_s} = \frac{\pi}{\hbar} N_{\mathrm{d}}(E_{\mathrm{F}}) \int |V^{sd}_{k,k'}|^2 \sin\theta d\theta, \tag{2.62}$$

where $V_{k,k'}^{sd}$ is the matrix element for transitions from s to d and θ is the angle between the momenta k and k'. The conductivity is given by

$$\sigma = \frac{n_s e^2 \tau_{\mathrm{s}}}{m_{\mathrm{s}}^*}, \tag{2.63}$$

where n_{s} is the density of s-electrons and m_s^* is the effective electron mass. The scattering of s-electrons in the minority (-) and majority (+) band are assumed to independently contribute to the conductivity:

$$\sigma = \sigma_{\mathrm{s}+} + \sigma_{\mathrm{s}-}. \tag{2.64}$$

This is the case if the spin is conserved during scattering events. The mean relaxation time for each channel (spin up and spin down) can be approximately defined as

$$\frac{1}{\tau} = \frac{1}{\tau_{\mathrm{ss}}} + \frac{1}{\tau_{\mathrm{sd}}}, \tag{2.65}$$

where $\tau_{\mathrm{ss}} = \tau_{\mathrm{s}-,\mathrm{s}-} = \tau_{\mathrm{s}+,\mathrm{s}+}$ is the relaxation time for intraband (within the majority or minority s-band) and τ_{sd} for interband (between the majority or minority s and d bands) scattering processes. Using Eq. (2.64) and Eq. (2.65) together with the definition of the resistivity $\sigma = 1/\rho$ yields

$$\frac{1}{\rho} = \frac{1}{\rho_{\mathrm{ss}} + \rho_{\mathrm{s}+,\mathrm{d}+}} + \frac{1}{\rho_{\mathrm{ss}} + \rho_{\mathrm{s}-,\mathrm{d}-}}. \tag{2.66}$$

This model is often referred to as 'two current' model and is depicted in Fig. 2.7 a).

This model leads to a decreasing resistivity even if the external field is large enough to saturate the magnetic specimen. This is because the d bands split further with increasing external field and the majority band shifts below E_{F} (compare Fig. 2.7 b)), which gradually decreases $N_{\mathrm{d}}(E_{\mathrm{F}})$. Hence possible scattering events are reduced and τ_s is increased while $\rho_{\mathrm{s}-,\mathrm{d}-}$ approaches zero. This background effect is called negative magnetoresistance and can be subtracted in measurements.

The discussed scenario still leads to an isotropic resistance for various field directions. The origin of the anisotropic magnetoresistance is the spin-orbit interaction which enables spin-flip scattering and can be described with the operator [46]

$$\mathcal{H} = \lambda_{\mathrm{LS}} \mathbf{L} \cdot \mathbf{S} = \lambda_{\mathrm{LS}} \left(L_{\mathrm{z}} S_{\mathrm{z}} + \frac{L^+ S^- + L^- S^+}{2} \right), \tag{2.67}$$

where λ_{LS} is the coupling constant and $L^{\pm} = L_{\mathrm{x}} \pm i L_{\mathrm{y}}$ and $S^{\pm} = S_{\mathrm{x}} \pm i S_{\mathrm{y}}$ are raising and lowering operators for angular momentum and spin, respectively. Eq. (2.67) yields a spin dependent contribution to the energy of the d states. The spin of d electrons is thus coupled to the orbital motion, which itself is coupled to the crystal field. As the crystal fields differ for various crystallographic directions, the resistance is anisotropic as well.

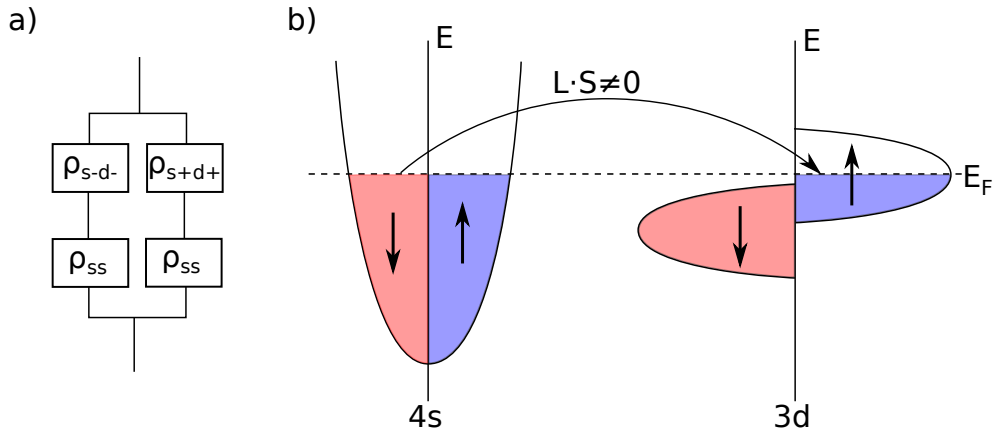

Figure 2.7: Schematic drawing of the density of states for a strong ferromagnet. The spin-orbit interaction enables scattering of electrons into different spin states. Exemplary a transition from the $4s^{\uparrow}$ to the $3d^{\downarrow}$ state is shown.

Eq. (2.67) applied to an electron state can lower (increase) the spin quantum number, while simultaneously increase (lower) the angular momentum quantum number. The z-direction was chosen as the axis of quantization. Fig. (2.7) b) illustrates one additional scattering event introduced due to spin-orbit interaction.

To quantitatively account for the anisotropy the relaxation times $\tau_{s\text{-,d}}$ and $\tau_{s+,d}$ need to be adjusted. This is usually done by introducing a proper scattering potential and recalculating the matrix elements introduced in Eq. (2.62). This, however, requires specific information on the wave functions and the magnetization (see [45] for a detailed calculation). Note that since most current is carried by s-electrons, transitions within the d band (d+ to d- or vice versa) can be neglected.

In the following the resistivity values are assumed to be known. In order to obtain a formula for the AMR ratio for arbitrary alignment of $\mathbf{M}$ and $\mathbf{J}$ the electrical field is considered

$$\begin{aligned}\mathbf{E} &= \rho_{\perp}(\mathbf{J} - (\hat{M}\cdot\mathbf{J})\cdot\hat{M}) + \rho_{\parallel}(\hat{M}\cdot\mathbf{J})\cdot\hat{M},\\ &= \rho_{\perp}\mathbf{J} + (\rho_{\parallel} - \rho_{\perp})(\hat{M}\cdot\mathbf{J})\cdot\hat{M},\end{aligned} \tag{2.68}$$

where $\hat{M}$ is a unit vector oriented along $\mathbf{M}$ and $\rho_{\perp}$ and $\rho_{\parallel}$ are the resistivity perpendicular and parallel to $\mathbf{M}$, respectively. Multiplication of Eq. (2.68) with $\mathbf{J}$ yields

$$\begin{aligned}\frac{\mathbf{E}\cdot\mathbf{J}}{J^2} = \rho &= \rho_{\perp} + (\rho_{\parallel} - \rho_{\perp})\cos^2\theta\\ &= \frac{\rho_{\parallel} + \rho_{\perp}}{2} + (\rho_{\parallel} - \rho_{\perp})(\cos^2\theta - \frac{1}{2}),\end{aligned} \tag{2.69}$$

where the angle between $\mathbf{J}$ and $\mathbf{M}$ is denoted θ. In the following a thin magnetic film is discussed. Assuming only in-plane magnetization the average value of $\cos^2\theta$ is 1/2 and the average resistance is defined as $\rho_{av} = (\rho_{\parallel} + \rho_{\perp})/2$. This value is adopted

if the system decays randomly into domains at zero applied field. The anisotropic magnetoresistance is thus defined as [43]

$$\mathrm{AMR} = \frac{\rho - \rho_{\mathrm{av}}}{\rho_{\mathrm{av}}} = \frac{2(\rho_{\parallel} - \rho_{\perp})}{(\rho_{\parallel} + \rho_{\perp})}(\cos^2\theta - \frac{1}{2}). \tag{2.70}$$

Application of an external magnetic field can be used to define the internal magnetization $\mathbf{M}$. In the case of $\theta = 0°$ Eq. (2.70) yields

$$\mathrm{AMR}_{\parallel} = \frac{(\rho_{\parallel} - \rho_{\perp})}{(\rho_{\parallel} + \rho_{\perp})}, \tag{2.71}$$

and for $\theta = 90°$

$$\mathrm{AMR}_{\perp} = -\frac{(\rho_{\parallel} - \rho_{\perp})}{(\rho_{\parallel} + \rho_{\perp})}. \tag{2.72}$$

The total AMR signal is therefore

$$\mathrm{AMR}_{\mathrm{tot}} = \frac{2(\rho_{\parallel} - \rho_{\perp})}{(\rho_{\parallel} + \rho_{\perp})} \approx \frac{(\rho_{\parallel} - \rho_{\perp})}{\rho_{\perp}}, \tag{2.73}$$

where we used $\rho_{\parallel} \approx \rho_{\perp}$ to estimate the denominator. The samples investigated in this thesis usually exhibit an AMR signal below 1%, justifying the approximation in Eq. (2.73).

2.6 Finite-difference simulations

The numerical simulations presented in this thesis have been performed with the open-source GPU-accelerated micromagnetic simulation software MuMax3. The program solves Eq. (2.17) applying a finite difference (FD) discretization using three dimensional grids of orthorhombic cells. Similar FD programs are for instance OOMMF and MicroMagnum. In addition also finite element (FE) software is available, for instance NMag or TetraMag. The choise for the FD software MuMax3 is mostly based on the advantage of high performance, compared to FE techniques. In the following relevant features and details about MuMax3 are presented, based on a detailed description found in [47].

FD methods usually divide the geometry into identically shaped cells. While volumetric parameters such as the magnetization or effective fields are considered at the center of each cell. Interfacial quantities like the exchange interaction are taken into account at the boundaries between cells. The exchange energy is calculated using a discretized version of Eq. (2.2) with 6 nearest neighbors for each cell, under the restriction of small angles. To estimate the range of validity a one dimensional magnetic spiral chain is considered. Fig. 2.8 shows simulated (red) and analytically derived (green) normalized energies for this system. As the tilting angle between neighboring spins, denoted spin-spin angle, reaches 5° the relative error is already

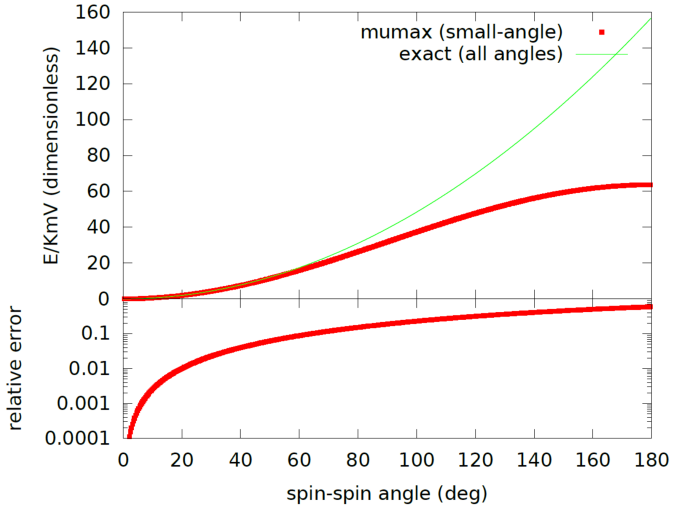

Figure 2.8: Normalized energy (top part) and relative error (bottom part) of a one dimensional magnetic spiral chain. The exactly calculated solution is shown in green, the simulation is shown in red. The error grows tremendously for increasing tilting angles between neighboring spins, denoted as spin-spin angle. Taken from [47].

0.1 percent. As a rule of thumb, the approximation of small angles is justified as long as neighboring cell spins are only tilted by less than $5°$. This condition can be guaranteed by adjusting the cell size. However this procedure can substantially increase the number of cells, which ultimately leads to a longer calculation time.

Dipolar energies are the only long-range interaction entering the energy density (Eq. (2.16)). Consequently, their computation is rather time-consuming. Within the framework of the FD technique the magnetostatic fields can be elegantly calculated as a convolution of the magnetization introducing a demagnetizing kernel $\hat{\mathbf{K}}$

$$\mathbf{B}_{\mathrm{demag,i}} = M_{\mathrm{S}} \hat{\mathbf{K}}_{\mathrm{ij}} \cdot \mathbf{m}_{\mathrm{j}}. \tag{2.74}$$

This treatment is only possible because of the regular meshgrid consisting of identical cells. Eq. (2.74) can be very efficiently evaluated using fast Fourier transforms (FFT), assuming a constant magnetization in each finite difference cell.

Within the framework of this thesis, simulations are mostly used to find magnetic ground states (compare section 4.1) or to dynamically excite the magnetization of a specimen (compare section 4.3). The magnetic ground state is found by means of energy minimization. MuMax3 first reduces the total energy until it reaches the numerical noise floor introduced by the FFT. This is done with the condition of high damping in order to accelerate the relaxation into the equilibrium state. Subsequently the torque is monitored instead of the energy, since it typically exhibits less noise. The relaxation process is continued until its maximal error is smaller than 10^{-9}. This procedure, however, can not guarantee for a global ground state since it may end up in a saddle point or local energy minimum.

Dynamic and static excitations are set for each cell, analogously to material parameters such as the saturation magnetization. Smooth time and space dependent excitations can be modeled by adding terms of the form $f(t) \times g(x, y, z)$, where $f(t)$ is a function of time t and $g(x, y, z)$ is a continuously varying spatial profile [47].

Within the frame of this thesis only Py coated magnetic nanotubes are simulated. Hence standard material parameters $\mu_0 M_S = 1$ T and $A_{ex} = 13 \cdot 10^{-12}$ J/m are used in all simulations presented.

3 Samples and experimental setups

This chapter introduces the investigated samples and experimental methods used in this thesis. First the growth mechanism of the GaAs cores and the deposition of the different coating layers is discussed. Subsequently the isolation process to separate a single nanotube is introduced. The remaining sections present the experimental methods and setups used to analyze static and dynamic properties of magnetic NTs. This comprises anisotropic magnetorestistance, scanning transmission X-ray microscopy, time-resolved magneto-optical Kerr effect and planar microresonator based ferromagnetic resonance measurements.

3.1 Gallium-catalyzed nanorod growth

The NTs produced in the scope of this thesis were grown Ga-catalyzed on a Si substrate, covered with a native oxide layer. Since the GaAs nanorods (NRs) grow parallel to the $\langle 111 \rangle$ direction, the silicon substrate surface is chosen to be Si(111) as well. This is necessary, to provide NRs with the long axis oriented perpendicular to the substrate plane. These NRs can subsequently be coated with a homogeneous metal layer.

A growth process on an untreated Si(111) substrate can sometimes result in a chaotic growth of the NRs. This is due to a thick oxide layer, that originates from the wafer production process [48]. The layer prevents epitaxial relation between the substrate and the NRs. If this is the case, the oxide thickness can be reduced before growth via wet chemical etching using ammonium fluoride (NH_4F). The ideal etching time depends on the oxide thickness. Very long etching times result in too large unpassivated areas on the substrate and GaAs clusters can partially form instead of NRs. The Si(111) wafers used in this thesis did not require any additional etching treatment.

Note that due to equivalent growth directions to the perpendicular [111] orientation there will always be NRs exhibiting a tilting angle with respect to the substrate normal (compare Fig. 3.1 a)).

The Si(111) wafer is mounted in a III-IV molecular beam epitaxy (MBE) vacuum system with a base pressure of $8 \cdot 10^{-11}$ mbar. The nanorods are grown by the vapor-liquid-solid (VLS) mechanism, first described in 1964 by Wagner and Ellis [49], who used gold particles to grow Si NRs. The samples investigated in this thesis were produced using gallium as catalyst. A thin layer of Ga is deposited on the substrate. Small Ga-droplets are formed due to surface tension if the specimen is heated sufficiently. Additionally, arsenic is provided as a constant background

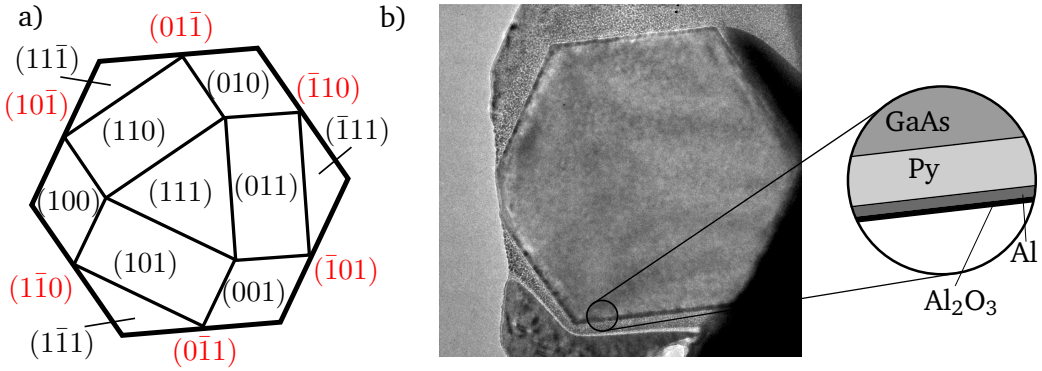

Figure 3.1: a) Crystallographic planes of a GaAs dot structure on the Si(111) surface. The planes marked red are the facets of the nanotube. b) TEM image of a thin nanotube slice, cut perpendicularly to the [111] direction. The inset shows the composition of the layers covering the tubes facets. Here the Py is 15 nm and the Al/Alox is 3 nm thick.

pressure within the chamber and Ga is evaporated onto the specimen at a constant rate. Common growth conditions are:

- Arsenic background pressure: $9 \cdot 10^{-6}$ mbar
- Gallium evaporation rate: 0.4 - 0.8 Å/s
- Substrate temperature: $\sim$ 600 °C

The liquid Ga absorbs the incoming arsenic and the gallium until a critical level of supersaturation is reached within the droplet. This will lead to a random nucleation of a stable GaAs nucleus, larger than one Ga-As atom pair, at the liquid solid interface. The saturation level consequently drops below the critical level and one complete solid layer is filled at the interface before nucleation of a new nucleus is possible [50, 51]. After completion of the layer, the saturation within the liquid rises again and the process starts over again. After many cycles a GaAs rod is created with the liquid droplet sitting always on top during the growth process.

Fig. 3.2 b) shows a transmission electron microscopy (TEM) image of a NT with a diameter of 500 nm. The different contrasts appearing within the NT represent wurtzite (WZ) and zinc-blende (ZB) crystal structures of the GaAs. The stacking sequence is ABAB... for WZ and ABCABC... for ZB, where one capital letter stands for a monolayer in the plane perpendicular to the [111] direction. This behavior is explained by the spontaneous nucleation of the GaAs crystal during overcritical saturation. Depending on which lattice site the nucleus is created the layer stacking is either WZ or ZB. While for optical properties of NTs the stacking can have a great influence [52], the properties of the magnetic shell is unaffected.

A crucial parameter during NR growth is the temperature. Only between 530°C and 670°C the VLS technique leads to the growth of GaAs NRs on Si(111) [48]. Temperatures below 540°C cause the Ga droplet to become solid. Above 670°C GaAs crystals are not stable under ultra-high vacuum (UHV) conditions. Both scenarios lead to the suppression of NR growth.

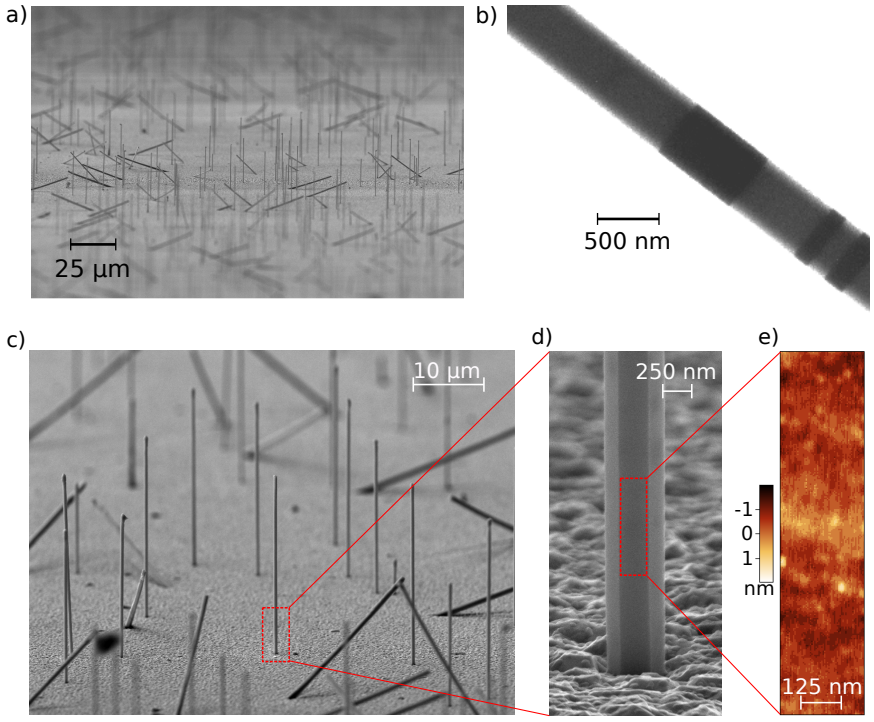

Figure 3.2: a), c) and d) SEM images of low density GaAs/Py NTs. The images were taken at a grazing incidence angle of 80° with respect to the surface normal. b) TEM image of a NT showing different contrast, corresponding to WZ and ZB crystal structures. e) AFM image of the top facet reveals a root mean squared roughness of $R_{\mathrm{rms}} = 0.4$ nm.

The actual growth process starts at high temperatures (> 670°C), such that no NR growth is possible. The above introduced conditions are applied (0.4 - 0.8 Å/s Ga evaporation rate, $9 \cdot 10^{-6}$ mbar As background pressure). The temperature is subsequently slowly reduced and the rotating wafer is investigated via reflection high-energy electron diffraction (RHEED). The RHEED signal is monitored during the temperature reduction. As soon as RHEED spots, which correspond to NR nucleation, appear, the temperature is increased by approximately 10°C. This prevents further nucleation of NRs, whereas the growth of the already existing NRs is not affected. This procedure leads to a controllable NR density. Usually the density was aimed to be very low in order to avoid shadowing effects which lead to tapered NTs, especially during shell growth. Typical values are approximately 1000 NRs/mm^2. Fig. 3.2 a) and c) display the low density NTs on the substrate. The SEM images were taken at an angle of 80° with respect to the substrate normal.

The specimen is held at constant temperature, until the desired length for the NRs is reached. Afterwards the temperature is decreased in order to solidify the Ga droplet and hence prevent further NR elongation. The created NRs usually have a diameter below 100 nm at this point. To create thicker NRs GaAs is simply deposited on the already existing facets until the desired diameter is reached. The finished NRs are in-situ transferred into a metal MBE system with a base pressure of $5 \cdot 10^{-11}$ mbar. Here the permalloy and the aluminum capping layers are deposited. The

thickness is monitored using a quartz micro balance. Knowledge of the deposited amount of material on a flat surface (previously calibrated) allows the determination of the metal thickness on the facet sides. The angle between the NTs long axis and the Py evaporation beam direction is 28° in our MBE system.

A TEM image of the finalized NT is shown in Fig. 3.1 b), together with a schematic drawing of the layer structure displayed in the inset. The outermost Al_2O_3 layer is created by oxidation of the Al capping layer in air. The six facet normals are oriented along the $\langle 110 \rangle$ directions, marked red in Fig. 3.1 a). The finalized samples exhibit very low roughness on the facet sides. A root mean squared roughness of $R_{\mathrm{rms}} = 0.4$ nm was measured using atomic force microscopy (AFM) on a 500 nm diameter NT with 15 nm Py and 3 nm Al (compare Fig. 3.2 e)).

3.2 Sample preparation

In order to investigate single NTs, they have to be detached from the Si wafer and brought to a flat surface where they can locally be contacted with gold leads. This can be done in different ways. For example the NTs can be dispensed into a liquid (usually isopropyl alcohol) using supersonic vibrations. The excitation causes the NTs to be ripped off the substrate and drifting in the liquid. Subsequent evaporation of the solution leaves only the detached NTs. This process, however, has some enormous downsides. Besides the impossibility of precise placement of individual NTs also information on the original positions is lost. This is a tremendous problem, since particular NTs might grow very close to each other on the Si wafer, causing an inhomogeneous metal coating on the facets. Depending on the actual distance, this changes the magnetic properties in an unpredictable way.

Within the scope of this thesis, a very careful approach was chosen to circumvent the formerly described problems. A Zeiss Crossbeam Auriga SEM-FIB microscope with integrated gas injection system (GIS) and nanomanipulator is used to select single NTs while they are still standing on the Si(111) substrate they were grown on.

The focused ion beam accelerates ionized Ga atoms with a voltage of 30 kV. The atom beam is focused to the sample. Different apertures allow for controllable beam currents. Hence, very precise cuts of approximately 100 nm diameter as well as very strong ion beams, capable of milling depths of approximately 100 μm are possible. The GIS is used to precisely deposit platinum at a desired location. The Pt is previously attached to a carrier gas, which is released through a nozzle in the direction of the specimen. Via electron bombardment the precursor gas releases the platinum which subsequently accumulates at the illuminated spot. The precision of deposition is therefore given by the focus of the electron beam (< 50 nm).

An exemplary sample preparation process is shown in Fig 3.3 a) - f). First, a suitable NT is selected, such that no other NTs are in its close vicinity. Thus, inhomogeneous metal layers or tapering effects occurring during the growth process

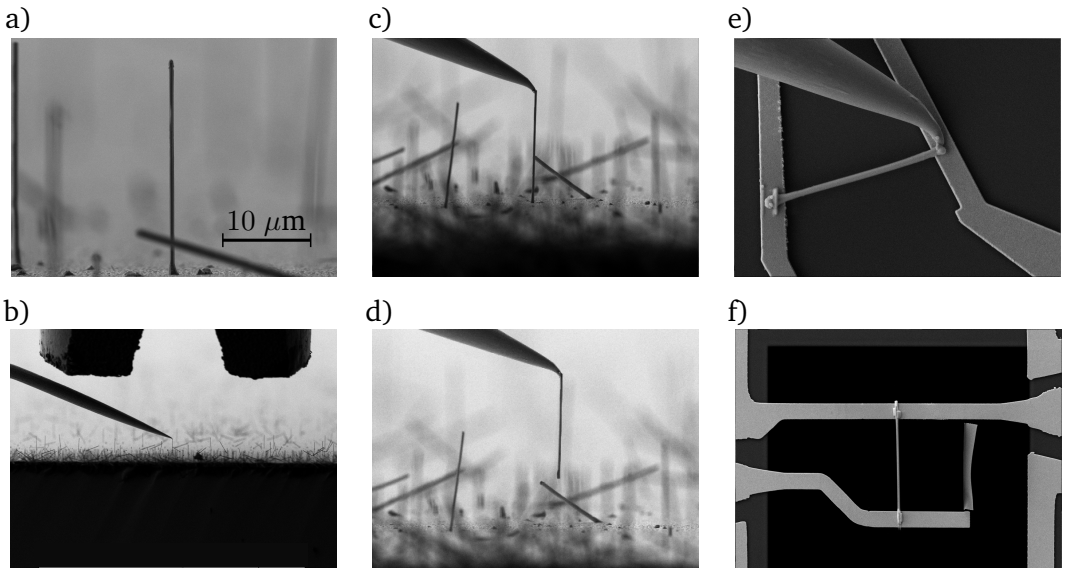

Figure 3.3: SEM images of the sample preparation process using a SEM/FIB dual beam system with integrated GIS and nanomanipulator. a) Selection of a vertically free standing NT. b) GIS nozzle at the top of the image and the nanomanipulator coming from the left side. c) The manipulator is fixed to the NT tip using platinum. d) The NT is detached at its bottom from the substrate using FIB. e) and f) It is now maneuvered to a second specimen, where it is connected to gold contacts on its top and bottom with platinum.

are not present for the chosen NT. Fig. 3.3 b) shows the GIS nozzle at the top of the image and the nanomanipulator entering the field of view from the left side. The NT is attached to the nanomanipulator at its tip using platinum, provided by the GIS. Subsequently the NT is detached from the substrate with a precise FIB cut at its bottom. At this point, it is important to work with small FIB currents, since the magnetic coating layer should not be damaged during this process step. Finally, the NT is attached to a flat substrate, were it can be accurately positioned and fixed with platinum. Usually it is enough to apply mechanical stress to remove the nanomanipulator. If not, FIB can be used to separate both. In Fig. 3.3 e) and f) the NT is mounted between two gold contacts, providing the possibility of applying currents through the NT. Depending on the experiment, the NT is positioned in different variations. In the following the experimental setups and the corresponding sample designs are introduced.

3.3 AMR experiment

The resistance change as a function of applied magnetic field strength and orientation is measured to obtain averaged information on the magnetization of a specimen. For this purpose the sample is mounted at the center of an electromagnet, capable of producing homogeneous fields up to 2 T. The actual field value is always monitored with a Hall sensor and can be actively adjusted by controlling the current that is

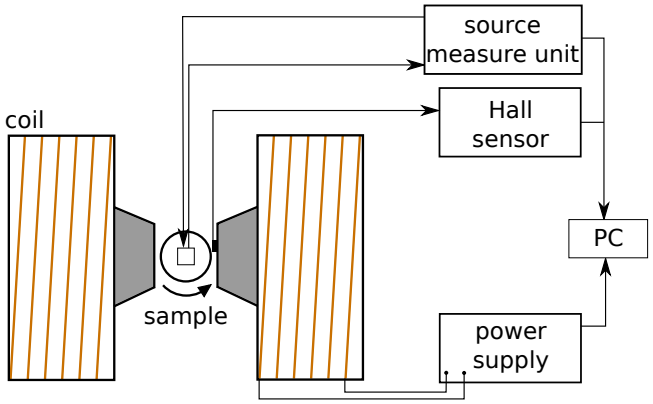

Figure 3.4: Illustration of the AMR setup. The sample is mounted between the pole shoes of a magnet capable of producing fields of up to 2 T. Current and voltage is simultaneously sourced and measured using a Keithley 2450 SourceMeter®.

flowing through the coils using a power supply. A 360° rotatable stage provides different in-plane angles between current and external field. The NT is connected to a Keithley 2450 SourceMeter® which is able to apply very low and stable dc currents in the range of 1 μA. Since the current is guided through a NT with very low cross-sectional area it needs to be very stable in order to not damage or destroy the NT. Simultaneously the resistance change is measured by the same unit. A sketch of the setup is shown in Fig. 3.4.

3.3.1 Sample design

The AMR signal is measured in a four point configuration to measure only the resistance change occurring in the NT. Fig. 3.5 shows a SEM image of a 500 nm diameter NT contacted by gold leads. The current is applied through the outermost contacts. Hence, a voltage measurement at the inner contacts solely detects the resistance arising from the NT and does not include resistance contributions due to the gold contacts or cables. The noise level is usually below 0.01%, whereas the measured AMR signals usually are in the range of 0.2 - 0.8%.

The NT was processed as described in section 3.2. Afterwards, the gold leads were evaporated at an angle of 30° with respect to the surface normal. Since most NTs investigated via AMR are 500 nm in diameter, this treatment is necessary to achieve good electrical contact between the NT and the gold contacts on the substrate surface. Hence a region deprived of Au deposition is created on the opposite side (Fig. 3.5).

3.4 TRMOKE experiment

Time and space resolved measurement of the magnetization dynamics is achieved by making use of the time resolved magneto optical Kerr effect (TRMOKE). This

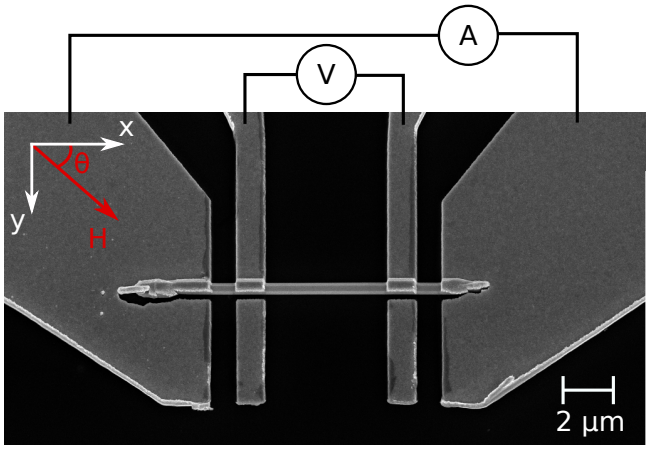

Figure 3.5: Exemplary AMR sample. The SEM image was taken at an angle of 45° with respect to the substrate normal. The NT shown here is 500 nm in diameter and the voltage contacts are 6 μm apart. The external magnetic field can be applied in the xy plane, which is defined as the substrate surface plane.

technique stroboscopically probes the dynamic out-of-plane component of the magnetization using pulsed laser beams. The spatial resolution is limited by the Abbe diffraction limit ($\approx \lambda/2 \approx 400$ nm) and the temporal resolution is defined by the laser pulse duration (usually in the range of picoseconds).

The magneto-optical Kerr effect describes the rotation of the polarization axis when linearly polarized light is reflected from a magnetic specimen. The process strongly depends on the relative orientation of $\mathbf{M}$ and the polarization axis. The experimental setup is only sensitive to the out-of-plane component of $\mathbf{M}$, known as the polar configuration [53].

A sketch of the experimental setup is shown in Fig. 3.6. A titanium-sapphire laser is used to generate short pulses of about 150 fs with a repetition rate of 80 MHz at a central wavelength of 800 nm. The laser is guided through a polarizer and is focused on the sample with an objective lens. The reflected light is analyzed using a Wollaston prism and photo detectors. The Wollaston prism is mounted such that it separates a polarized incident beam into two orthogonally polarized components with equal intensity. Any rotation of the polarization axis due to the Kerr effect induced by a magnetic specimen, leads to an asymmetric intensity shift proportional to $2\Theta_\mathrm{k}$, where Θ_k is the Kerr rotation angle.

The sample is positioned on a piezoelectric stage with a lateral range of several tens of micrometers and a vertical displacement of some microns. In addition to the laser beam, the light from a light emitting diode (LED) with a wavelength of $\lambda = 635$ nm is coupled into the beam path and illuminates a large part of the sample which is recorded by a CCD camera. Hence, an optical image of the sample is generated, enabling immediate adjustment of the specimen position and focus during measurement.

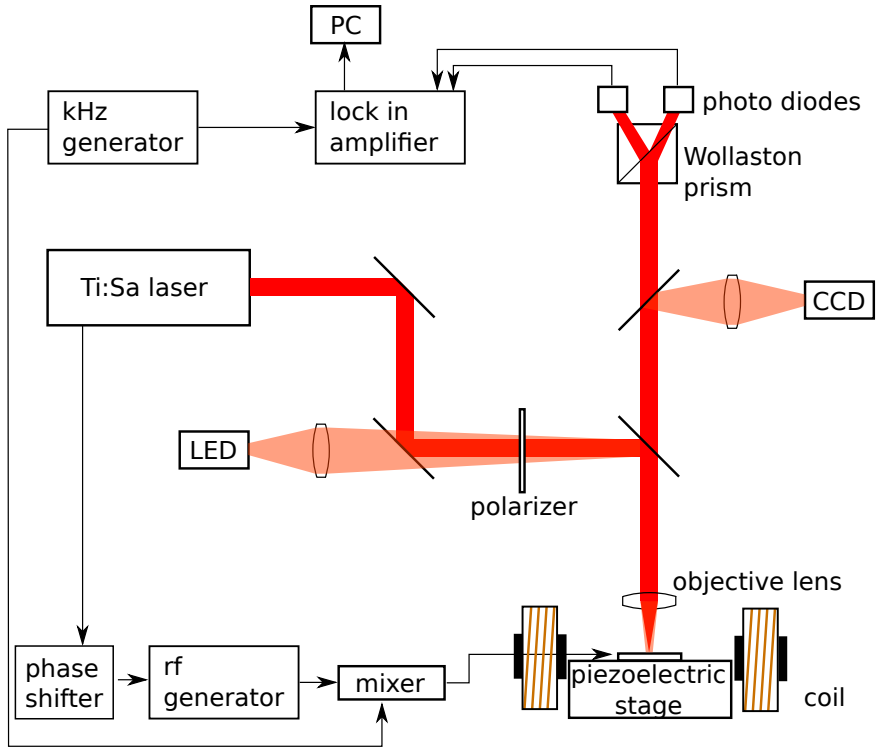

Figure 3.6: Schematic drawing of the TRMOKE setup. Linearly polarized, pulsed, laser light is focused on a magnetic sample excited with rf fields. After deflection from a magnetic specimen, the axis of polarization is rotated due to the MOKE effect. A Wollaston prism and photo diodes are used to measure the Kerr rotation. Lock-in technique is used to additionally enhance the signal.

An external field of up to 300 mT can be applied using coils with a soft-iron core. The field can be rotated by 360° in the plane of the sample, which in turn is mounted at the center of the coil, in order to create a homogeneous field at the specimen site.

The magnetic moments of the sample are excited with rf fields h_{rf} in the GHz regime. A coplanar waveguide is used to locally convert the rf currents, created by a signal generator, into rf fields (compare Fig. 3.7). The excitation can be chosen to be out-of-plane, if the NT is positioned in the gap, or in-plane, if it is placed on the signal line. Ideally, h_{rf} is chosen to be perpendicular to $\mathbf{M}$. The phase between rf signal and laser pulses is locked, meaning the magnetization is measured at constant phase. The phase can be actively stabilized and shifted with an electronic phase shifter, enabling measurements over very long periods of time.

In order to increase the signal-to-noise ratio, lock-in technique is used to measure the Kerr signal. Thus, the setup is only sensitive to a dynamical out-of-plane magnetization component. Usually a modulation frequency of 6.6 kHz was applied to enable lock-in detection. A more detailed description of the setup can be found in [31].

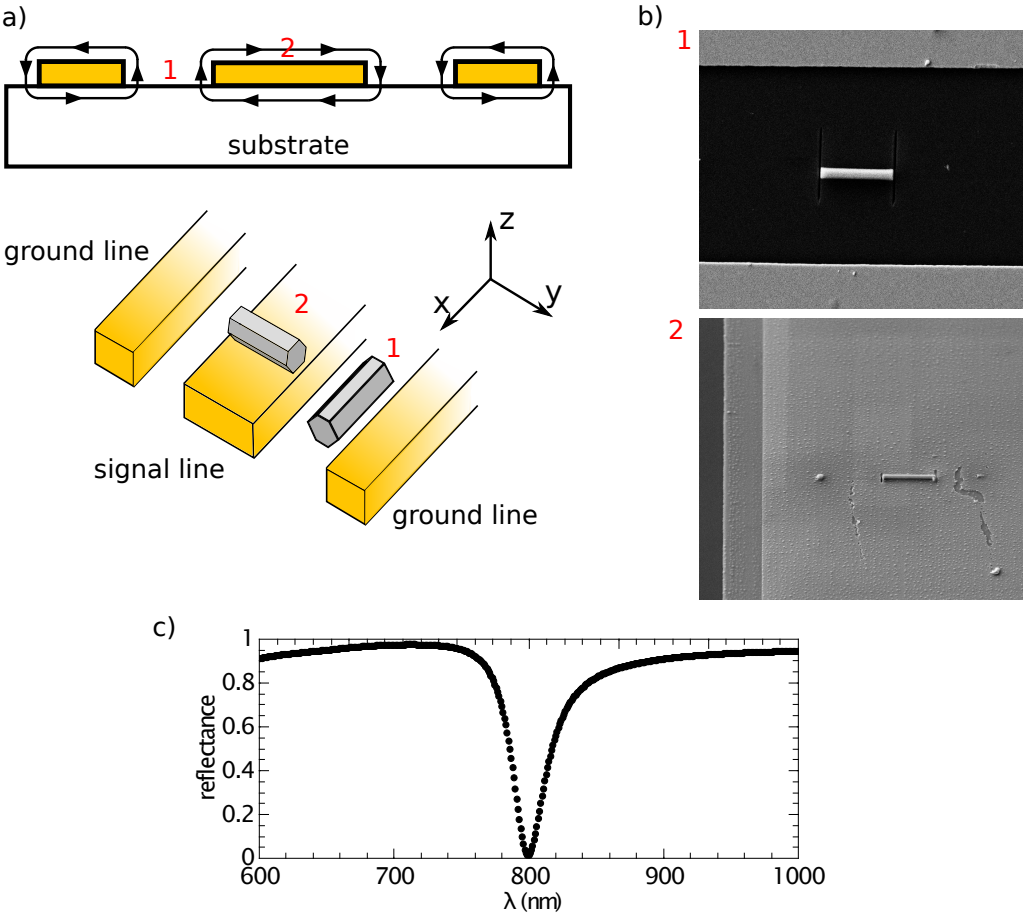

Figure 3.7: a) Illustration of the driving fields, generated by the CPW. The NTs are placed at two positions, denoted 1 and 2. 1: Within the gap of the CPW, where mostly out-of-plane excitation is present (parallel to the z-axis). 2: On top of the signal line where the driving field is aligned in-plane (parallel to the y-axis). b) Images of the actual samples. The NT at position 1 (2) is 4 μm (7.5 μm) long. c) Calculated reflectance of the 25 nm Au / 173 nm Al_2O_3 anti-reflection layer placed on the 150 nm thick Au signal line.

3.4.1 Sample design

The magnetic moments of the specimen are excited using rf fields in the GHz regime (2 - 14 GHz). These fields are generated using CPWs, consisting of one signal line and two ground lines as shown in Fig. 3.7 a). CPWs can be manufactured for a large range of frequencies with only little losses. The rf generator is connected to the signal and ground lines. Due to induction a current with reversed sign but equal intensity flows in the two ground lines. This generates regions of different excitation field directions within the CPW. An out-of-plane field is generated in the gap and an in-plane field is present at the top of the signal line, denoted position 1 and 2 in Fig. 3.7 a), respectively.

The NT is either placed on position 1 or 2. SEM images in Fig. 3.7 b) display the samples. As can be seen, the dimensions of the NT compared to the width of the CPW

gap or the width of the signal line are significantly smaller. Hence, inhomogeneous contributions to the driving field, arising for instance due to the skin effect, can be neglected.

The NTs were processed as described in section 3.2. However, since TRMOKE is a surface sensitive technique, the attachment of the NT to the substrate with Pt may interfere with the experimental method as it prevents optical access to parts of the top facet. Hence the NT is additionally connected to the surface with a 5 nm thick, transparent, Al_2O_3 layer using atomic layer deposition (ALD). Since this is enough to fix the NT to substrate it can subsequently be cut into a specific length in order to remove the Pt contaminated parts and create straight endings. The resulting samples have no Pt deposited on their top facet and are shown in Fig. 3.7 b).

In case the NT is placed in position 2 an additional treatment of the signal line was used, to improve the signal-to-noise ratio. This turned out to be necessary because of the high reflectance of the gold signal line. An anti-reflection layer for a wavelength of 800 nm was deposited on top of the signal line in order to reduce the reflected light from the signal line. The reflection of the NT is not affected by this additional layer. The calculated reflectance is shown in Fig. 3.6 c). Hence mostly light reflected from the NTs facet enters the photo detectors, reducing the noise level of the measurement. The layer consists of 25 nm Au and 173 nm Al_2O_3, both deposited on a 150 nm thick signal line. Since the destructive interference is very sensitive to the top Au layer thickness, it was grown as a wedge (20 - 30 nm). A suitable position at which total destructive interference occurs for the laser light is determined by measuring the reflected intensity and the NT is positioned accordingly.

3.5 PMR-based FMR experiment

An averaged signal of the dynamical response of a magnetic specimen to microwave excitation is provided by the planar microresonator based FMR experiment. The technique investigates the quality factor change as a function of applied field to gain information about magnetic properties. A resonator is usually characterized by its quality factor, defined as

$$Q = 2\pi \frac{\text{energy stored in system}}{\text{energy loss per cycle}}. \tag{3.1}$$

Hence, $Q^{\text{cav}}_{\text{empty}}$ accounts for the energy losses of an empty cavity, for instance, due to absorption of microwave radiation by the cavity walls. At resonance the precessing magnetic moments of the investigated sample absorb additional excitation energy and the quality factor is reduced to $Q^{\text{sample}}_{\text{res}}$. Assuming a negligible contribution of the

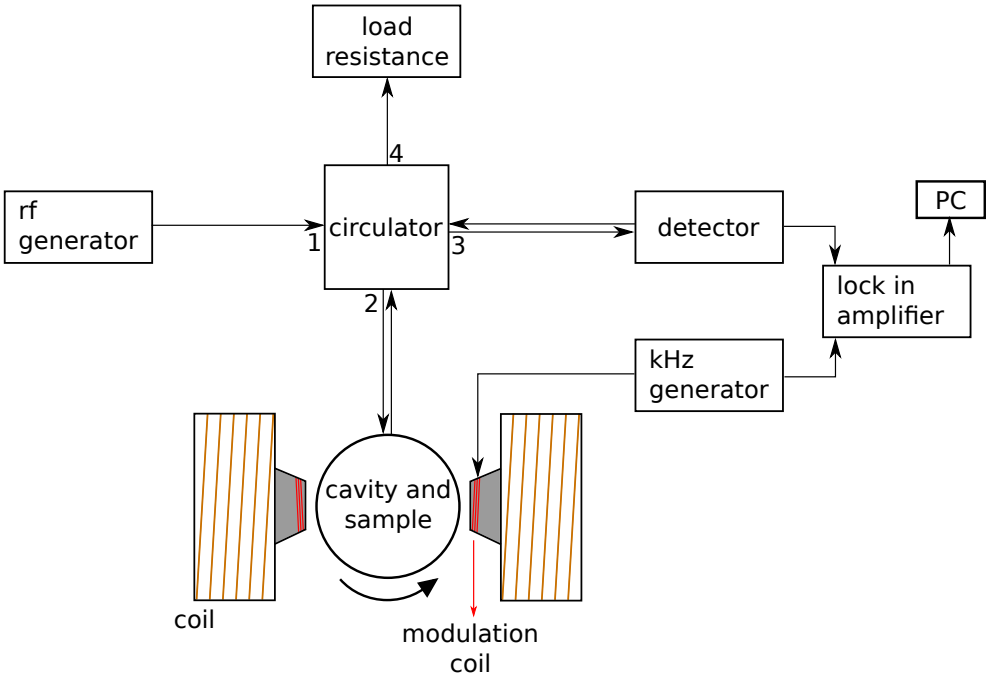

Figure 3.8: PMR based FMR experimental setup. Rf excitation is guided through a cavity including a magnetic sample. During FMR the quality factor of the cavity is lowered, which is detected by analyzing the reflected rf power. Typically a field modulation approach is used to enable lock-in detection.

sample at non resonance on $Q^{\text{cav}}_{\text{empty}}$, the relative change due to magnetic resonance of a sample within the cavity can be derived applying Eq. (2.19) to be [54]

$$\frac{Q^{\text{sample}}_{\text{res}}}{Q^{\text{cav}}_{\text{empty}}} = \chi'' F Q^{\text{cav}}_{\text{empty}}, \tag{3.2}$$

with the filling factor F defined as

$$F = \frac{\int_{\text{sample}} h^2_{\text{rf}}\, dV}{\int_{\text{cavity}} h^2_{\text{rf}}\, dV}. \tag{3.3}$$

In the case of a homogeneous rf field distribution within the cavity, F reduces to the ratio of sample to cavity volume. Eq. (3.2) yields a direct connection between the relative change of the quality factor and the imaginary part of the susceptibility χ''. Hence, detection of $Q^{\text{sample}}_{\text{res}}/Q^{\text{cav}}_{\text{empty}}$ provides information on the FMR of the magnetic sample, in our case a NT.

The experiment was conducted at the Helmholtz-Zentrum Dresden - Rossendorf, Institute of Ion Beam Physics and Material Research under the supervision of Dr. J. Lindner. A detailed description of theory and experiment can be found in [54].

The setup is sketched in Fig. 3.8. Rf frequency is guided through a four-port microwave circulator to the microcavity shown in Fig. 3.9. The circulator separates wave paths depending on the port they enter. Microwaves can only pass from the entrance port i to port j=i+1. At the microresonator (named 'cavity and sample'

in Fig. 3.8) a fraction of the rf signal gets reflected and enters the detector after passing the circulator from port 2 to 3. The mechanism of reflection as well as the necessary geometry will be discussed in the following subsection 3.5.1. The detector basically consists of a Schottky diode, used to analyze the microwave power, which is in turn converted into a dc voltage. The measured voltage can again be linked to the magnetic susceptibility as it is shown in [54]. In the case of a critically coupled system, all incident power gets absorbed by the cavity and the signal voltage ΔU_{sig} reaches its maximum value

$$\Delta U_{\mathrm{sig}}^{\mathrm{max}} = \alpha_0 \cdot \chi'' F Q_{\mathrm{empty}}^{\mathrm{cav}} \cdot \sqrt{P_0}, \tag{3.4}$$

were α_0 is a detector parameter, dependent on the resistance of the Schottky diode and P_0 is the initial rf power. Eq. (3.4) reveals the importance of the filling factor F and the quality factor of the empty cavity. In order to improve the signal-to-noise ratio the cavity volume must be comparable to the NTs magnetic volume.

Finally any rf signal reflected from the detector unit gets absorbed by a load resistance placed at the fourth port of the circulator.

3.5.1 Sample design

The microresonator consists of copper and is grown on a Si substrate, fully metalized at its back side. The structure illustrated in Fig. 3.9 describes an open circuit, at which the rf signal entering from the left gets reflected. The rectangular and radial open ends, denoted C1 and C2, act as capacitances, while the microresonator loop can be described as an inductance L. Hence, the microresonator can be compared to a RLC oscillator circuit operating in the GHz regime. The resonance frequency of the RLC circuit is determined by L and C2, whereas C1 is used to match the impedance to the usual value of 50 Ω. While the resulting electrical field generates maxima at the far ends of C1 and C2, it is almost zero inside the microresonator loop. In contrast, the magnetic field inside the loop is homogeneous and oriented normal to the substrate surface.

The inset of Fig. 3.9 shows an exemplary PMR sample. The NT (500 nm diameter) is positioned inside the microresonator loop and cut into a length of 7.5 μm. The NTs axis is parallel to the surface of the substrate, leading to a homogeneous out-of-plane rf excitation over the full length of the NT.

3.6 STXM experiment

This section introduces the scanning transmission X-ray microspectroscope at the PolLux end station at the Swiss Light Source (SLS) synchrotron. A detailed description of the PolLux facility can be found in the original publication [55].

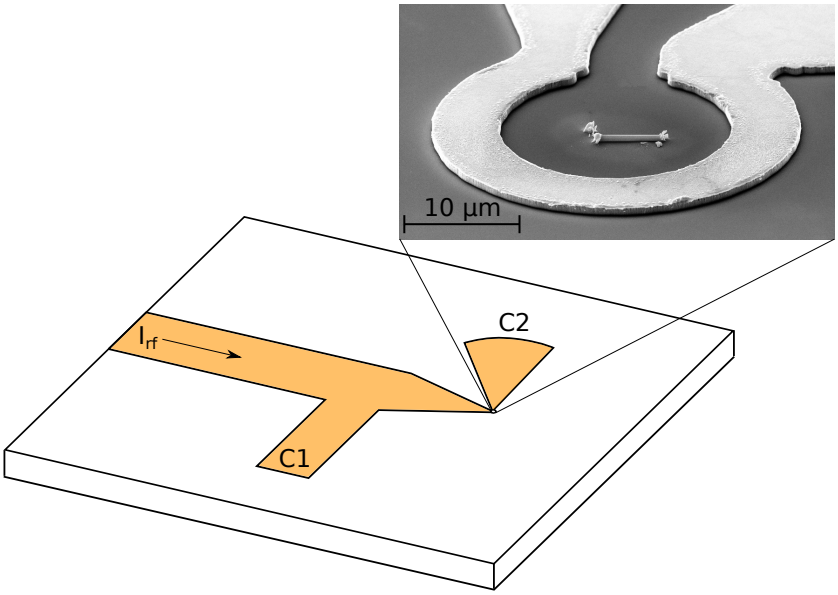

Figure 3.9: Sketch of the microresonator geometry. The rf signal is injected into the strip on the left side and generates a standing wave pattern between capacity C1 and C2 with a node of the electric field at the cavity. In contrast the magnetic field is maximal at the cavity site and generates a homogeneous out-of-plane excitation. The inset shows an exemplary SEM image of a NT with a diameter of 500 nm, placed inside the cavity.

The 2.4 GeV electron storage ring at the SLS usually operates in the top-up mode, meaning additional electrons are injected every 4-5 minutes, keeping the beam intensity constant. The X-rays are generated by a bending magnet located inside the storage ring, which basically forces the electrons on a circular path. The permanent acceleration thus generates synchrotron radiation. The beam path is sketched in Fig. 3.10.

In order to obtain magnetic contrast it is necessary to access right- and left-handed circularly polarized X-rays. At the SLS this can be achieved by four successive dipole magnets located inside the storage ring. The magnets slightly tilt the electron beam orbit relative to the optical axis of the beamline, causing a shift in synchrotron light direction. As illustrated in Fig. 3.10 this can be utilized to select the polarization of the X-ray light using an aperture. If these magnets are inactive the X-rays exhibit linear polarization.

The beam is now guided through a grating monochromator in order to adjust the desired energy. The system can operate at photon energies E_{ph} between 200 and 1400 eV. Typically, the measurements presented in this thesis were conducted at the Fe 2p absorption edge ($E_{\mathrm{ph}} = 709.8$ eV).

The beamline as well as the STXM usually operate under vacuum conditions. Both volumes are separated by a thin silicon nitride membrane located in front of the zone plate. Thus the sample inside the STXM can be easily mounted at atmospheric pressure and evacuated before the measurement. Subsequent to the monochromator the X-rays are focused to a spot on the sample using a Fresnel zone plate. Higher

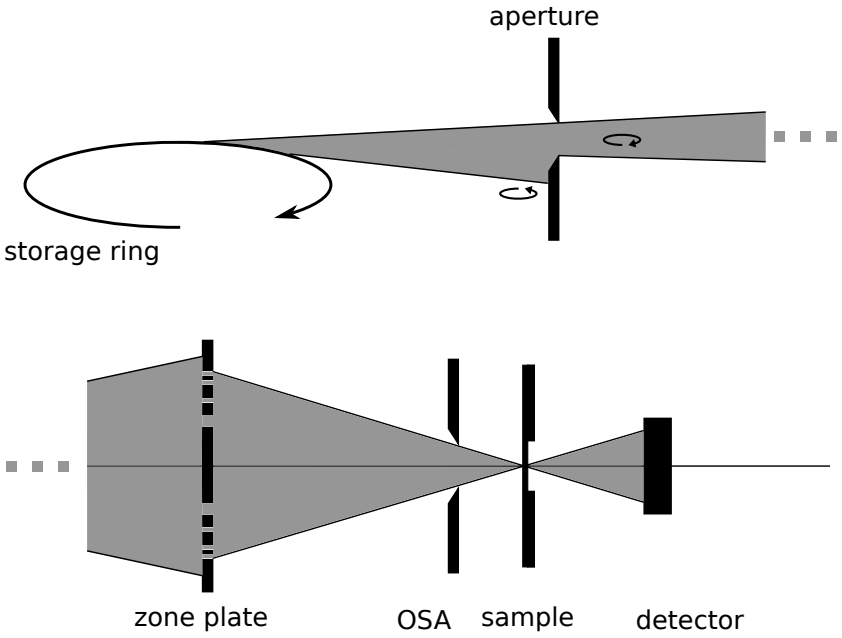

Figure 3.10: Illustration of the X-ray beam path at PolLux end station. Left- or right-handed circularly polarized light can be selected by an aperture. The beam is focused using a Fresnel zone plate. The order selecting aperture (OSA) transmits only the first-order focus onto the sample. Finally, the transmitted light is measured by a photodiode detector.

diffraction orders are absorbed by the order selecting aperture, mounted in front of the sample. The spatial resolution is approximately 20 nm. In order to obtain images the sample is scanned through the focal point in a plane perpendicular to the beam direction. During the scan the transmitted intensity is measured using a photo detector. If necessary, a magnetic field can be applied at the sample position, perpendicular to the beam direction.

Magnetic imaging is possible utilizing the X-ray circular dichroism (XMCD) effect. For this purpose two images, with right and left circularly polarized light are taken. Their difference is obtained by calculating the XMCD asymmetry given by

$$I_{\mathrm{XMCD}} = \frac{I_{\mathrm{left}} - I_{\mathrm{right}}}{I_{\mathrm{left}} + I_{\mathrm{right}}}. \tag{3.5}$$

The XMCD method is only sensitive to components of the magnetization collinear with the X-ray beam. Since the setup requires some seconds to switch from left to right handed polarized light, the XMCD technique is rather slow and is thus only suitable for imaging of static magnetic configurations.

In order to investigate dynamical properties the sample is excited with local rf fields. The beam pulse repetition rate and the rf excitation are locked at constant phase, such that the magnetization can be probed stroboscopically with each pulse. In this case the signal is detected using lock-in technique. The general detection scheme is very much comparable to the one described in section 3.4.

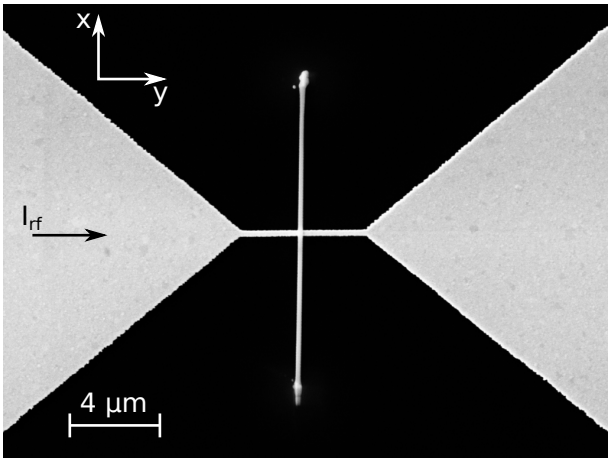

Figure 3.11: SEM image of an exemplary STXM sample. A NT (210 nm diameter) is placed on top of a 250 nm wide copper antenna. The magnetic moments of the specimen are excited by rf currents guided through the antenna. A magnetic field can be applied in the xy plane, which is defined as the surface plane. The X-ray radiation is applied perpendicular to the xy plane. The whole structure is located on a 200 nm thick silicon nitride membrane.

3.6.1 Sample design

An exemplary STXM sample is shown in Fig. 3.11. The magnetic NT is placed on top of an antenna. The NT is usually oriented such that the top facet is parallel to the substrate surface. The antenna generates a local inhomogeneous driving field at the center of the NT. Due to the small width of the antenna (250 nm) it can not be matched to the impedance of the system (usually 50 Ω). Thus, it acts as a resistance, causing most of the current to be reflected. In general, the higher the frequency, the more power gets reflected. For example, in case of an antenna structure as the one shown in Fig. 3.11, for $f = 4.6$ GHz the input power is 4 times higher compared to the throughput power.

The entire structure shown in Fig. 3.11 is placed on a 200 nm thick silicon nitride membrane. The X-ray beam is directed perpendicular to the substrate surface. The antenna as well as the contacts consist of copper, since the material is transparent for X-rays at the given thicknesses. Hence also information on the NTs dynamics directly on top of the antenna is accessible.

4 Experimental results

This chapter summarizes the experimental findings obtained in the present work. First the static properties of permalloy NTs are discussed. The AMR effect in combination with micromagnetic simulations is utilized to gain insight into the magnetic ground states of several types of NTs. By means of STXM the magnetization texture of a single NT is imaged in real-space. Complex ground states were found, made possible due to magnetic pinning. Dynamical properties are investigated either with a spatially resolved technique using TRMOKE or by averaging methods such as PMR based FMR. Both techniques provide access to mode patterns related closely to the geometry of the NTs. The chapter closes with a discussion of spin waves in NTs, investigated both experimentally with STXM or TRMOKE and theoretically with simulations.

4.1 Static properties of ferromagnetic nanotubes

The static magnetization of single NTs will be discussed in this section. First, simulations on magnetic NTs without anisotropy and FMR measurements on a full film Py sample are presented to illustrate the expected magnetic ground state of hexagonally shaped NTs. The actual magnetic ground states of individual NTs are investigated in the following subsection by utilizing the AMR effect. We find significant differences compared to full film samples, which are linked to a high anisotropy. The tunability as well as the origin of the NTs magnetic state at zero external field are subsequently discussed. The section concludes with an introduction of multi-domain states found in NTs at zero field and an analysis of the associated domain walls.

4.1.1 Ground state simulations without anisotropy

This section introduces simulations conducted in order to investigate the magnetic ground states at zero applied field for different types of hexagonally shaped NTs. A sketch of the NT is provided on the right side in Fig. 4.1 a). The diameter measured from vertex to vertex is denoted ϕ_{vv}, the Py shell thickness is $t = 15$ nm for all simulations shown within this subsection. The simulated volume was discretized into a $64 \times 64 \times 256$ (x, y, z) grid, where the length of the NT is oriented parallel to the z-direction. Since the NT is hexagonal, the magnetic layers in x and y direction exhibit a slightly different amount of active cells. This does not influence the magnetic state after the relaxation process, since simulations with a

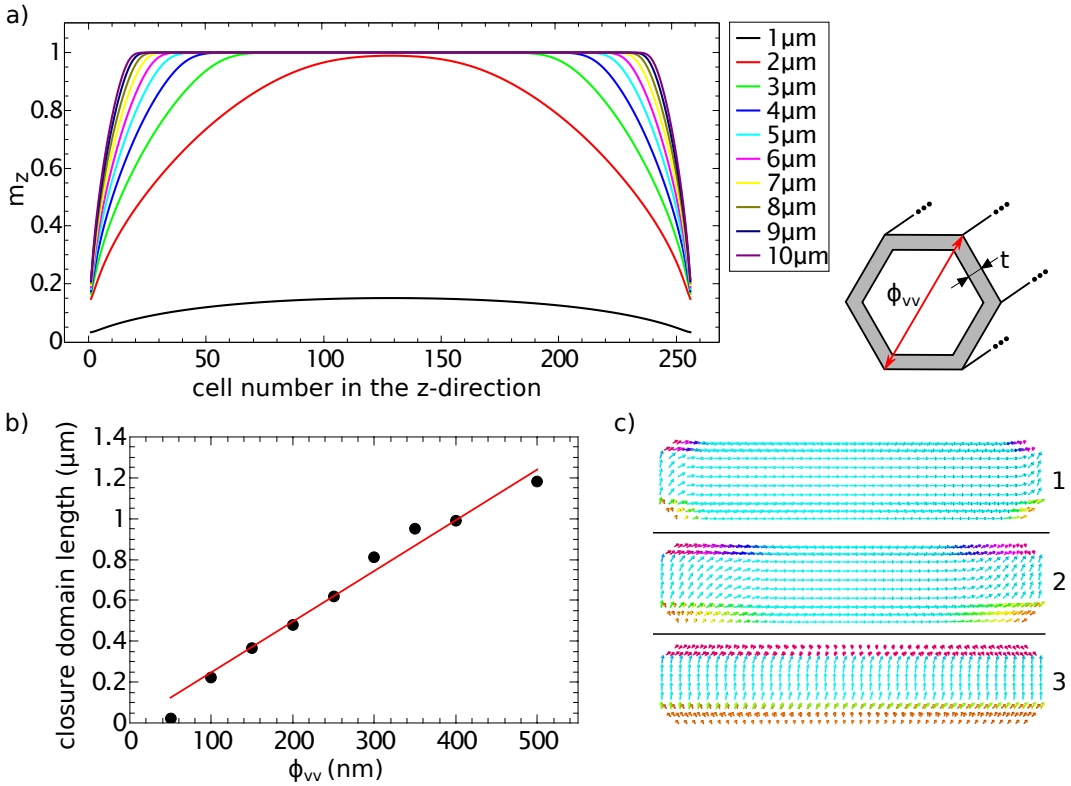

Figure 4.1: a) Normalized magnetization component parallel to the tubes axis (z-direction) for different tube lengths shown in the legend. The simulations reveal the NTs ground state occupied at zero external magnetic field. The tube parameters are $\phi_{vv} = 500$ nm and $t = 15$ nm. b) Simulated dependence of the closure domain length on the NT diameter, while $t = 15$ nm is held constant. The data is fitted with the linear function $y = 2.48 \cdot x$. As the rotation of $\mathbf{M}$ in the z-direction is continuous, the cut-off condition for the closure domain length was chosen to be 95% of $\mathbf{M}$ pointing parallel to the tubes axis. c) Illustration of the magnetic states. 1 and 2 exhibit closure domains and 3 is in a global vortex state.

more detailed grid ($128 \times 128 \times 512$) resulted in similar final states, while taking a sufficiently larger amount of time to compute.

Since all, by means of AMR, experimentally investigated NTs exhibit $\phi_{vv} = 500$ nm a length dependence for this particular diameter is conducted and shown in Fig. 4.1 a). The graphs display the z-component of $\mathbf{M}$, normalized to the saturation magnetization for different lengths L ranging from 1 - 10 μm. Each point in the graph is generated by averaging over a cross sectional area perpendicular to the NTs axis, with a thickness of one cell. In case the NT is longer than 3 μm its magnetic ground state basically consists of a center part, magnetized parallel to the tubes axis and two closure domains located on each side (compare Fig. 4.1 c) 1 and 2). The closure domains avoid stray fields, that would otherwise be present at the NTs endings. All graphs shown in Fig. 4.1 a) exhibit a nearly perfect symmetry. However, the closure domains on either side can have different chirality. In this study no dependence of closure domain chirality and tube parameters is found. In contrast, we find both situations, identical chirality and different chirality almost

equally often. Similar results have been found for ground state simulations on cylindrical tubes [10]. This indicates that both states are energetically degenerate for sufficiently long NTs. Exemplary ground states are depicted in Fig. 4.1 c). 1 and 2 show the same chirality on both tube endings.

An interesting feature revealed by simulations is an almost constant length of the closure domains, irrespective of the NTs length. The averaged length of both closure domains is denoted L_{cd}. For a length range of 3-10 μm the simulations shown in Fig. 4.1 a) exhibit 1.18 ± 0.02 μm. Tubes shorter than 3 μm result in the closure domains touching each other at the center of the tube. This leads to a vortex state condition in the form of $L_{cd} > L$. Whereas a mixed state with constant L_{cd} prevails in case $L_{cd} < L$.

A similar behavior is obtained for all investigated tube diameters. The averaged closure domain lengths under the restriction $L_{cd} < L$ are shown in Fig. 4.1 b) for various NT diameters. It seems that L_{cd} depends linearly on ϕ_{vv}. The corresponding red line was fitted such that it intersects with the origin of the diagram. Similar results were reported by Landeros et al. where cylindrical NTs are investigated by means of Monte Carlo simulations [10]. Their theoretical model also predicts L_{cd} to be independent of the tubes length.

4.1.2 The onion state

The onion state can only be occupied if a certain field threshold applied perpendicular to the tube is exceeded. Thereafter reducing the external field to zero may lead to the appearance of the OS as metastable state, as shown by AMR measurements in the next subsection.

In the current subsection the OS is more closely investigated. To do so, micromagnetic simulations are conduced on a NT with comparable properties to sample s1 introduced in table 4.1, namely $K_2^{s1} = -23000$ J/m^3, tube diameter $\phi_{vv} = 500$ nm, Py thickness $t = 15$ nm. The magnetic field is applied perpendicular to the NTs axis as depicted in Fig. 4.2 b). The coordinate system is chosen such that z is parallel to the NT, y is parallel to the facet and x is normal to the facet. Due to the given symmetry of the OS, only one of four equivalent facets is considered, highlighted in Fig. 4.2 b) by the eye looking normal to the facet plane.

Due to the high anisotropy included in the simulations the NTs ground state is a VS. A field of 55 mT is necessary to force the NT to occupy the OS. Consequently two domain walls form on the left and right vertex of the NT (compare Fig. 4.2 b)). The domain wall profile, meaning the magnetization component parallel to the NT (z-direction) is shown in Fig. 4.2 a). As the field increases, the domain walls shrink in size and become largely confined at the vertices. At $H_{\text{ex}} = 390$ mT the m_z component disappears. At this value the external field is large enough to force the magnetization to point out-of-plane at the corner. The resulting state

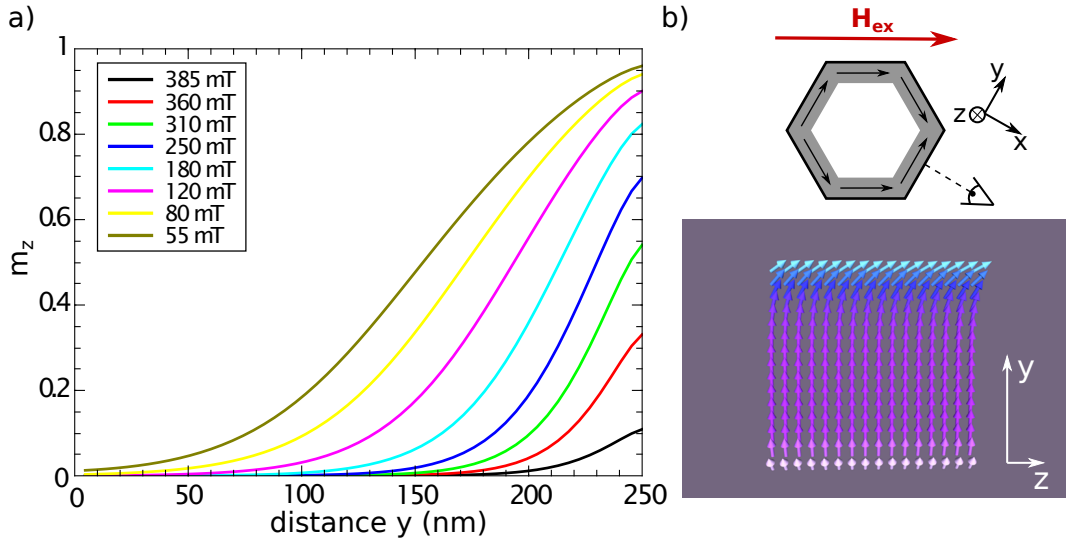

Figure 4.2: a) Domain wall profiles of the OS. If $H < 55$ mT the vortex ground state is occupied, whereas for $H > 385$ mT the domain wall is forced out-of-plane causing the m_z component to vanish. b) Illustration of the OS. z is parallel to the tubes axis, x (y) is normal (parallel) to the facet plane. The images shows the considered facet magnetization for an applied field $H_{ex} = 350$ mT.

shows an equivalent AMR response as a VS, since all magnetization components are perpendicular to the current direction.

4.1.3 Uniaxial magneto crystalline anisotropy in Py thin films grown on GaAs(110)

According to section 3.1 the facet normals of hexagonally shaped GaAs rods are parallel to the $\langle 110 \rangle$ directions. In order to account for crystalline properties of Py grown on a GaAs(110) surface, a flat and extended Py layer grown on a full wafer is investigated in this subsection.

A GaAs(110) wafer is heated up to a temperature of 600°C for 10 minutes while simultaneously an arsenic background of $1.7 \cdot 10^{-5}$ mbar is applied in high vacuum conditions in order to remove the native oxide layer of the GaAs. The sample is subsequently in-situ transferred to a MBE system, where a Py layer of 15 nm thickness is deposited. To prevent the sample from oxidation additionally a 3 nm layer of Al is added. The layer structures are equivalent to those of the NT sample s1 introduced in the following subsection in table 4.1.

The finished wafer is cleaved into pieces of roughly 3×4 mm^2. The magnetic properties are studied by means of conventional full film FMR. The sample is placed on a CPW of comparable size and both are mounted in the gap of an electro magnet, which is capable of applying in-plane fields up to 1 T. Various field angles can be set by a rotatable stage. The rf intensity throughput of the CPW is measured by means

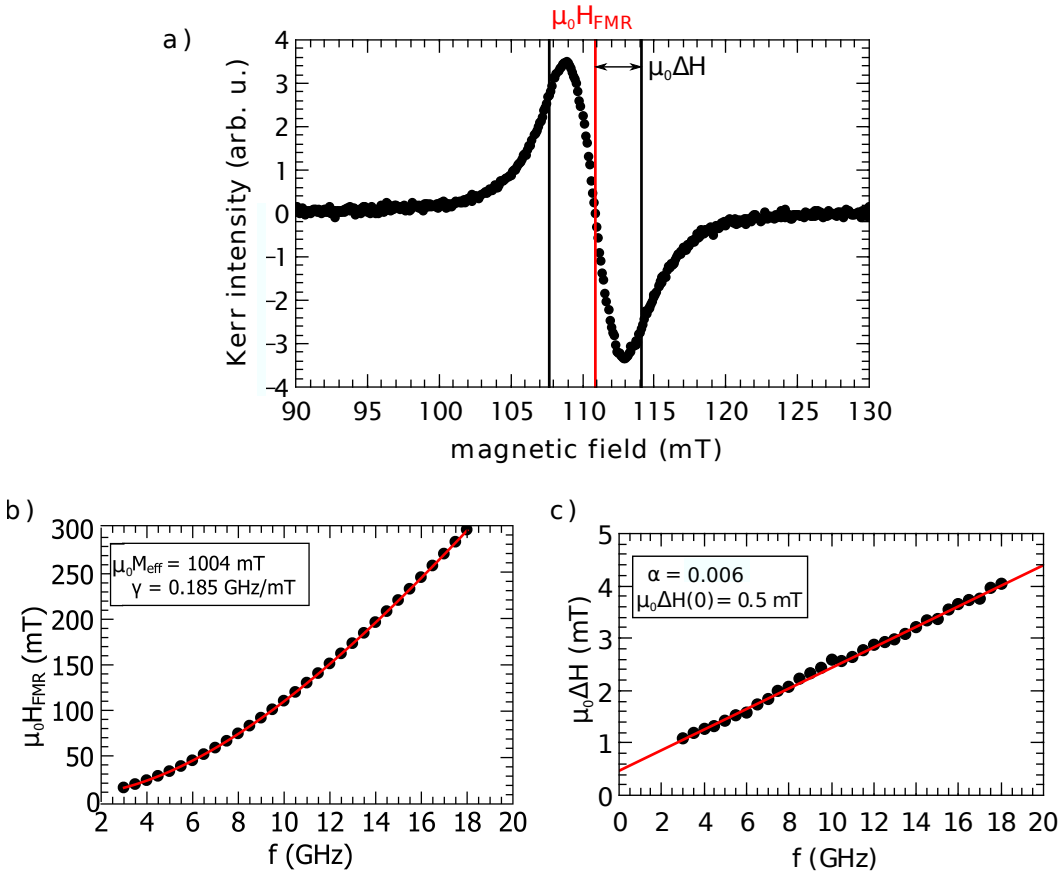

Figure 4.3: FMR analysis of 15 nm Py layer grown on GaAs(110). a) FMR spectrum obtained for $f = 10$ GHz. $H_{\mathrm{FMR}} = 110.8$ mT and $\Delta H = 3.2$ mT. b) H_{FMR} measured as a function of frequency along the [001] direction. The red line shows the Kittel fit yielding $\mu_0 M_{\mathrm{eff}} = 1$ T. c) Half width at half maximum ΔH measured as a function of frequency for the $[1\bar{1}0]$ direction. From the linear fit the damping $\alpha = 0.006$ is extracted.

of field-modulated lock-in technique. The experimental setup is described in detail elsewhere [56].

An exemplary measurement at a frequency of 10 GHz is shown in Fig. 4.3 a). Since the absorption of the CPW is measured with lock-in technique the signal resembles the derivative of a Lorentzian. Using Eq. (2.33), the field value at which FMR takes place (H_{FMR}) as well as the half width at half maximum ΔH can be extracted. Both quantities are marked in Fig. 4.3 a). In order to obtain material parameters the frequency is varied and both H_{FMR} as well as ΔH are extracted. The resulting graphs are shown in Fig. 4.3 b) and c). The data presented in b) is fitted using Eq. (2.27) and the effective magnetization is determined to $\mu_0 M_{\mathrm{S}} = 1.00$ T. In case of zero anisotropy $M_{\mathrm{S}} = M_{\mathrm{eff}}$ according to Eq. (2.28). The linewidth depicted in c) is fitted by Eq. (2.32) and the damping factor α is determined to be 0.006. The intersection with the ΔH axis, denoted $\Delta H(0)$, is related to inhomogeneities in the magnetic layer. All the obtained quantities so far are in agreement with standard values for high quality Py films (for instance see [57]). Especially the low damping

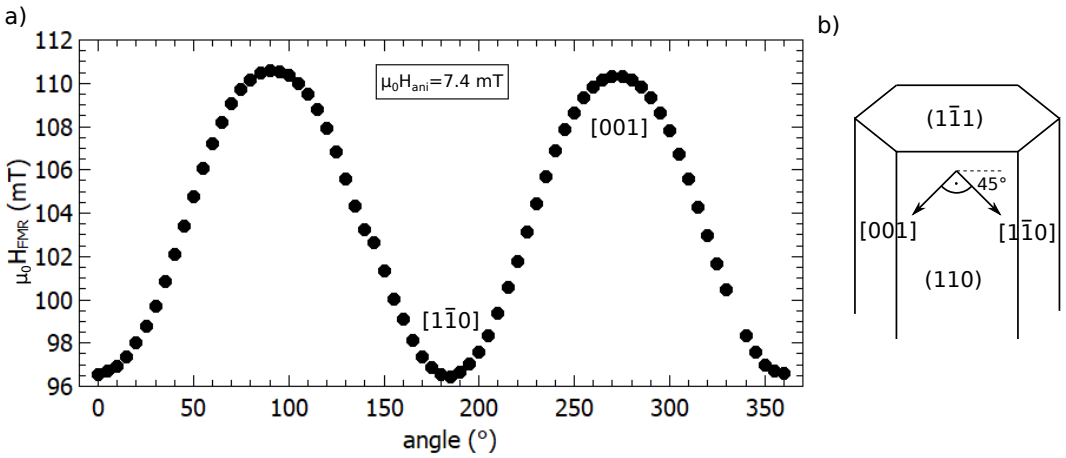

Figure 4.4: Angular dependence of a 15 nm thick Py film grown on GaAs(110). The two-fold anisotropy has a strength of H_{ani} =7.4 mT. The crystalline orientations of easy and hard axis according to the full film measurement are compared to a NT with growth direction [1$\bar{1}$1] and facet orientation (110). The crystalline orientations do not align parallel or perpendicular to the NTs axis.

and the low value of $\mu_0 \Delta H(0) = 0.5$ mT indicate a well grown Py layer with little inhomogeneities.

In order to detect crystalline anisotropies an angular dependence of the resonance field is measured and shown in Fig. 4.4 a). The graph exhibits clearly a two fold anisotropy with hard and easy axis in the [001] and [1$\bar{1}$0] directions, respectively. The strength of the anisotropy is $\mu_0 H_{\text{ani}} = 7.4$ mT. Similar measurements conducted on thinner Py layers also grown on GaAs(110), reveal no significant changes of the anisotropy. Three different Py thicknesses: 6, 8 and 10 nm have been measured, which all exhibited a crystalline anisotropy of $\mu_0 H_{\text{ani}} \approx 6$ mT with no distinct tendency towards lower film thicknesses.

In addition to that the same measurement is conducted on a full film sample with a 5 nm Al_2O_3 layer in between the GaAs(110) and the Py. The result is a vanishing crystalline anisotropy with $\mu_0 H_{\text{ani}} < 0.7$ mT. Due to the amorphous structure of Al_2O_3, this behavior is expected, as well as exploited in the next subsection to manipulate the anisotropy in magnetic NTs.

The facet orientation and growth direction of the NTs described in section 3.1 as well as the hard and easy axis orientation obtained from the full film measurement are shown for the (110) facet in Fig. 4.4 b). The NTs growth direction was chosen to be [1$\bar{1}$1], consequently one of the facets is the (110) plane and thus directly comparable to the full film case. The hard and easy axis are located within the facet plane and both enclose an angle of 45° with the growth direction of the NT. Hence the crystalline anisotropy favors neither a vortex state nor a uniform state in a magnetic NT.

sample	s1	s2	s3	s4
layer	Py/Al	Al_2O_3/Py/Al	Al_2O_3/Py/Al	Py/Al
t (nm)	15	15	15	30
ϕ_{vv} (nm)	500±20	500±20	500±20	250±20
AMR (%)	0.25±0.03	0.7±0.05	0.09	-
K_2 (kJ/m^3)	-23±1.5	-15±1	-	-22±2
$\mu_0 H_{sat,\parallel}$ (mT)	53±3	30±3	< 5	50 ±5

Table 4.1: Overview of important parameters and results for the NT types investigated in this thesis. All NTs had an Al capping layer with a thickness of 3 nm. If Al_2O_3 is present it has a thickness of 1 nm. t denotes the Py layer thickness and ϕ_{vv} the NT diameter measured from vertex to the opposing vertex. K_2 is the in-plane anisotropy constant. $H_{sat,\parallel}$ is the external magnetic field necessary to align the magnetization $\mathbf{M}$ parallel to the NTs long axis.

4.1.4 AMR measurements on single nanotubes

The results shown in this subsection are partially published in [11].

All NT types investigated in the course of this thesis are summarized in Table 4.1, together with important parameters and results. First the ferromagnetic ground state found in Py coated NTs is introduced, followed by a discussion on the influence of the Al_2O_3 buffer layer, the NT length and the substrate temperature during growth of the Py layer. The anisotropy and corresponding energies will also be discussed. The subsection ends with an explanation of the origin of the enormous anisotropy in terms of a shadowing effect occurring during growth of the Py layer. The setup introduced in section 3.3 is utilized for the experiments presented in the following. The external field is swept from positive to negative field values if not explicitly stated different.

The ground state of magnetic nanotubes

Fig. 4.5 presents an AMR measurement conducted on a NT with $\phi_{vv} = 500$ nm, t =15 nm and 3 nm Al capping layer, referred to as sample s1. The diameter is always determined ex-situ after deposition of all coating layers and measured from vertex to opposite vertex. An uncertainty of ± 20 nm is given by the scanning electron microscope utilized for this purpose.

In case the field is applied parallel to the tubes axis (black dots), the measurement shown in Fig. 4.5 immediately reveals that the magnetic state at zero magnetic field differs from that at high fields, denoted position 2 and 1 in Fig. 4.5 respectively. When sweeping the magnetic field up and down the ground state at zero field is taken without hysteresis, indicating a continuous transformation between states 1 and 2. Furthermore, the resistance for high fields applied perpendicularly to the tube's axis (position 3) converges to the value of the black curve at zero field. This means the two states have to be either identical or result in the same AMR response.

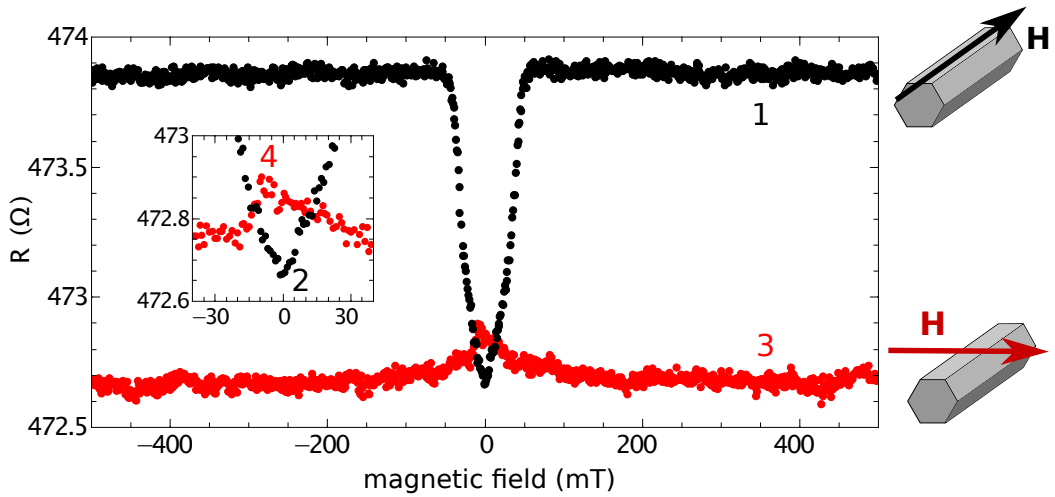

Figure 4.5: AMR measurement for two field directions. The black dots correspond to field applied parallel to the tubes axis and the red points correspond to field applied perpendicularly to the tubes growth direction. The inset shows the field region from -40 to 40 mT. Important positions on both graphs are marked with numbers 1-4.

The first possibility is not reasonable, since the magnetic state at position 3 is a energetically unfavorable variation of an onion state (see simulation in Fig. 4.7 b1)). The field is large enough to make the domain walls of the onion state vanish. Thus the magnetization is solely perpendicular to the current direction. This state can only be occupied as long as a very high external field is applied, since even out-of-plane components of $\mathbf{M}$ are present at the lower and upper edges (compare Fig. 4.7 b1)). Considering a vortex state at zero applied field, the AMR signal also obtains a minimum, since the magnetization is perpendicular to the current direction, which is necessarily always oriented parallel to the NTs long axis. Application of a magnetic field along the tube's length therefore results in a continuous transformation from the vortex state to the uniform state. As soon as all magnetic moments are oriented parallel to the external field, the resistance does not change anymore. This field value is denoted $\mu_0 H_{\mathrm{sat},\parallel}$ and is determined to be 53 ± 3 mT in the measurement presented in Fig. 4.5.

The inset of Fig. 4.5 displays the field region between -40 and 40 mT in detail. During the transformation starting from a fully in-plane configuration to zero field (black dots) the NT state continuously enters the VS at zero field, whereas for perpendicularly applied field (red dots) remanence (position 4) occurs. The field is swept from positive to negative and the resistance still increases beyond 0 mT. This behavior can be caused by a metastable onion state entered if the field is applied perpendicularly to the tube. Since the OS exhibits two domain walls with magnetization components parallel to the NT, the resistance is increased compared to a VS. In order to transform an onion state to a vortex state, large areas of the magnetization would have to be rotated (compare Fig. 4.2 b)). This introduces an

energy barrier, potentially preventing the transition between both states. A different explanation for the resistance difference of position 2 and 4 is a multiple domain state. This state introduces domain walls which create magnetization components parallel to the tubes axis (compare Fig. 2.6 f)) causing a slight increase in resistance. The absolute value depends on the number of domain walls. This issue will be discusses further in section 4.2.1, where additional information provided by STXM measurements is used to address the question.

Influence of the Al_2O_3 buffer layer

In order to further investigate the origin of the VS a second type of NTs is fabricated. This time a 1 nm thick Al_2O_3 layer separates the GaAs from the 15 nm thick Py film. The diameter is again 500 nm and the Py is capped with 3 nm Al. The sample is referred to as s2.

The AMR measurement is displayed in Fig. 4.6 a). Both samples s1 and s2 are measured in a four-point configuration with voltage contacts separated by $9\ \mu$m (compare Fig. 3.5). Hence the measured resistance is directly comparable. Due to the insulating Al_2O_3 buffer layer of s2, current is largely prevented from entering the semiconducting GaAs core, increasing the resistance R_0 from 472.5±0.2 Ω for s1 to 620.5±0.2 Ω for s2. The suppressed current-flow in the GaAs also increases the AMR ratio $(R_\parallel - R_\perp)/R_\perp$ by roughly a factor of 3, from 0.25 ± 0.03 % for s1 to 0.7 ± 0.05 % for s2. This can cause a deteriorating signal-to-noise ratio which can only partially be compensated by enhancing the current. Typical current values are 1-10 μA. Considering the Py layer and the GaAs core as parallel current channels and assuming the 1 nm Al_2O_3 layer to be perfectly isolating, the resistance of the GaAs core is determined to 2000 Ω.

The most important difference between s1 and s2 is the value $\mu_0 H_{\text{sat},\parallel}$. For s2 $\mu_0 H^{\text{s2}}_{\text{sat},\parallel} = 30\pm3$ mT, which is significantly lower than $\mu_0 H^{\text{s1}}_{\text{sat},\parallel} = 53\pm3$ mT for s1. Hence, the uniaxial anisotropy favoring the VS as magnetic ground state was reduced by the buffer layer. In the following the magnitude of the uniaxial anisotropy is investigated in detail by a simple analytic model.

The transition from VS to US is monotonic in field. In addition there is no state higher in energy than the US and lower than the VS (for instance, compare black dots in Fig. 4.6). It is comparable to a hard axis loop, where the difference between initial an final state is a measure of the energy difference between both states. The difference in energy density between VS and US, denoted $\Delta\epsilon$, can thus be obtained using the relation

$$\mu_0 H_{\text{sat},\parallel} = \frac{2\Delta\epsilon}{M_S}, \tag{4.1}$$

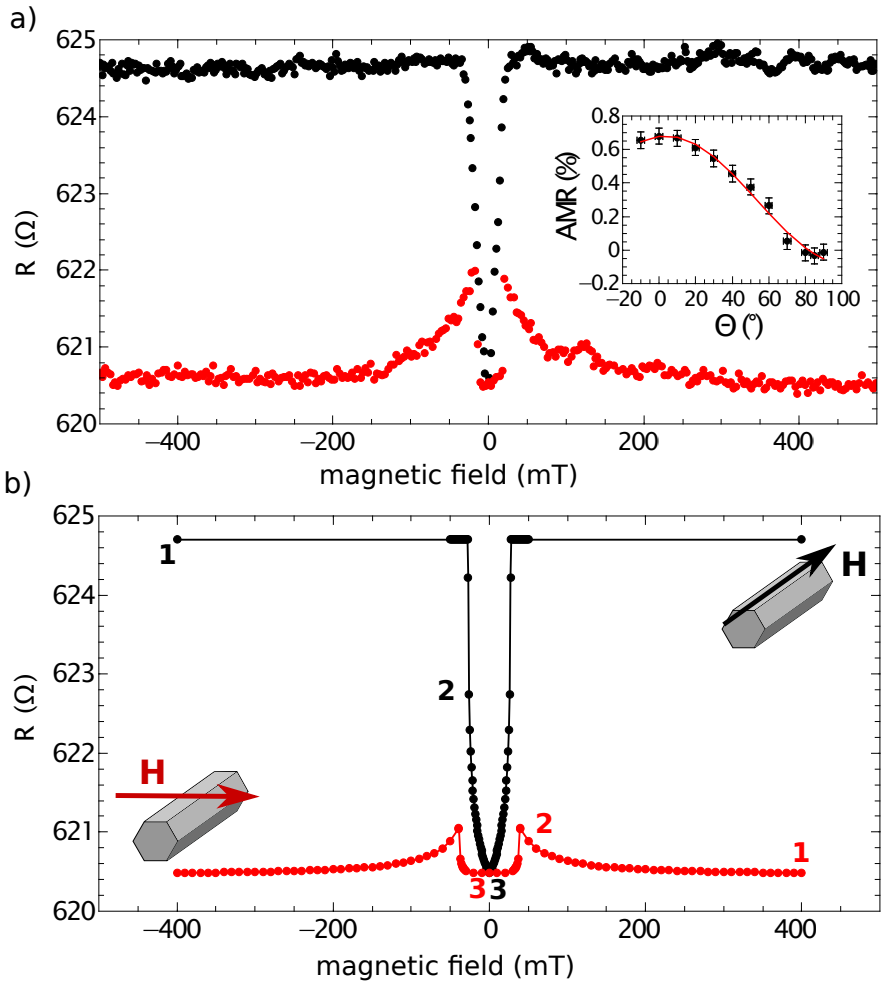

Figure 4.6: a) AMR measurement of sample s2, consisting of 15 nm Py and 1 nm Al_2O_3 between the GaAs core and the magnetic layer. The inset shows the absolute AMR value for different angles Θ, obtained at 1 T. Were $\Theta = 0$ corresponds to the field applied parallel to the tubes axis (black dots) and $\Theta = 90$ corresponds to field applied perpendicularly to the tubes axis (red dots). b) AMR simulation of the measurement shown in a). The magnetic states for points marked with red and black numbers are shown in Fig. 4.7.

where M_S is the saturation magnetization of Py, measured for instance in section 4.1.3. Eq. (4.1) yields $\Delta\epsilon_{s1} = 21200$ J/m^3 and $\Delta\epsilon_{s2} = 13200$ J/m^3 for samples s1 and s2. The total energy density difference $\Delta\epsilon$ can be split up in its components

$$\Delta\epsilon = \Delta\epsilon_{\text{ex}} + \Delta\epsilon_{\text{ani}} + \Delta\epsilon_{\text{dem}}, \tag{4.2}$$

comprising the exchange energy density difference $\Delta\epsilon_{\text{ex}}$, the anisotropy energy density difference $\Delta\epsilon_{\text{ani}}$ and the demagnetizing energy density difference $\Delta\epsilon_{\text{dem}}$. The exchange energy is zero in case of a US due to the parallel alignment of all magnetic moments and only appears in the VS, induced by the six edges, at which the magnetic moments are tilted. The hard axis of the anisotropy is known to be aligned parallel to the tubes axis, hence it is negligible for the VS, since all magnetic

moments are pointing along the easy axis. Finally, due to the flux closed nature of the VS, the demagnetizing energy density is nearly zero, whereas the US creates a stray field at the ends of the tube. Hence, Eq. (4.2) can be rewritten as

$$\Delta\epsilon = (0 - \epsilon_{\text{ex,VS}}) + (\epsilon_{\text{ani,US}} - 0) + (\epsilon_{\text{dem,US}} - 0). \tag{4.3}$$

The anisotropy is assumed to be uniaxial and can thus be described by

$$\epsilon_{\text{ani,US}} = -K_2 \cos^2\Theta, \tag{4.4}$$

where K_2 is the uniaxial anisotropy constant and Θ is the angle between hard axis and $\mathbf{M}$. $\Theta = 0$ if $\mathbf{M}$ is parallel to the tubes axis. The demagnetizing energy of the US is approximated by a general ellipsoid [58]

$$\epsilon_{\text{dem,US}} = \frac{1}{2}\mu_0 M_S^2 \frac{t}{t+L} = 300 \frac{\text{J}}{\text{m}^3}, \tag{4.5}$$

where $t = 15$ nm is the thickness of the Py coating and $L = 20$ μm is the length of the NT. In order to estimate the exchange contribution to Eq. 4.2, micromagnetic simulations are used. Two AMR simulations have been conducted using $K_2^{\text{s1}} = -21000$ J/m^3 and $K_2^{\text{s2}} = -13000$ J/m^3. The latter is shown in Fig. 4.6 b). From the simulations the values $H_{\text{sat,}\parallel\text{,sim}}^{\text{s1}} = 48$ mT and $H_{\text{sat,}\parallel\text{,sim}}^{\text{s2}} = 28$ mT are obtained. Using these values and Eq. (4.5) together with Eq. (4.2) yields $\epsilon_{\text{ex,VS,sim}}^{\text{s1}} = 2100$ J/m^3 and $\epsilon_{\text{ex,VS,sim}}^{\text{s2}} = 2100$ J/m^3. Hence, the exchange energy density does not change for different anisotropies and can be used to obtain the anisotropy constants from the measurements. Finally utilizing all values discussed above, Eq. (4.2) gives $K_2^{\text{s1}} = -23000$ J/m^3 and $K_2^{\text{s2}} = -15000$ J/m^3 for s1 and s2, respectively. Hence the 1 nm thick Al_2O_3 buffer layer reduces the anisotropy by a factor of 1.5. All values obtained above are summarized in table 4.1.

An angular dependence of the absolute AMR signal, obtained at 1 T, is shown for s2 in Fig. 4.6 a). The AMR signal was normalized to the resistance at zero field R_0 and shows a maximum (minimum) corresponding to a parallel (perpendicular) alignment of current and external field. The data follows the well known $\cos^2\Theta$ dependence of Eq. (2.70) and the fitted function is shown in red.

Another feature of sample s2 becomes evident when applying the external field perpendicular to the tubes axis (red dots in Fig. 4.6). As usual the field is swept from positive to negative values. For $H < 15$ mT the resistance suddenly drops to a value, comparable to the high field response. Thus, the resistance reduction indicates a transition of the onion state into a VS. This differs from the behavior of sample s1, where an increasing resistance indicates a hysteretic characteristic.

Fig. 4.6 b) shows a simulated AMR graph using the uniaxial anisotropy K_2^{s2} corresponding to sample s2. Due to the large anisotropy found in the measured NTs, the simulations were conducted applying periodic boundary conditions (PBCs) to a slice of a NT of length 1 μm. The large anisotropy prevents USs or mixed states,

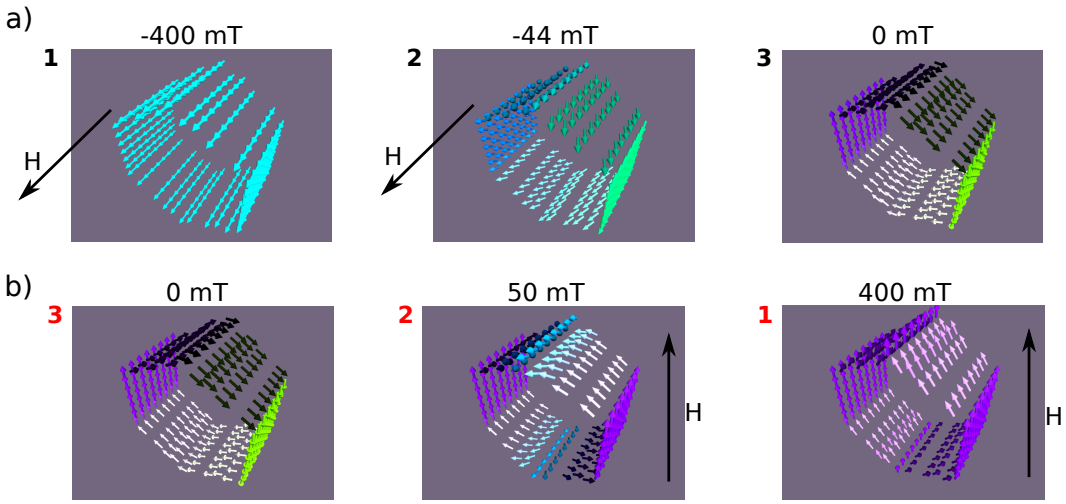

Figure 4.7: Simulated magnetic states, exemplary shown for a slice of the NT. The numbers are introduced in Fig. 4.6 b). In case of black (red) numbers the field is applied parallel (perpendicular) to the NTs axis. a1) displays a US, a3) and b3) show the VS at zero field and b2) is in an onion state with domain walls oriented parallel to the tubes axis at the top and bottom corner.

such as a US with closure domains from occurring at zero field. Therefore PBCs are a justified treatment to the given problem. Furthermore the application of PBCs decrease the computation time by many orders and thus the single cell size can be reduced to a value below the exchange length of Py (≈ 5 nm). All simulations conducted were able to enter the VS in case the field was applied perpendicularly to the tubes axis. In addition the transition from onion state to VS takes place at higher fields than for the measurements. For instance, during simulations shown in Fig. 4.6 the VS is obtained at field values twice as large as compared to measured values. The discrepancy between simulation and measurement is likely attributed to magnetic pinning. The pinning seems to be pronounced if the Py film is directly grown on the GaAs facets.

Fig. 4.7 shows simulated magnetic states obtained for various applied field values and directions. a) corresponds to field parallel to tubes axis and b) shows the perpendicular case. While both scenarios enter the vortex state at zero applied field, a continuous rotation of $\mathbf{M}$ is only achieved in a). The onion state is displayed in b2), which gradually transforms into an onion like state with large out-of-plane components at the side facets shown in b1) for very large fields.

Length variation

In order to investigate the influence of the demagnetizing field on the ground state, two samples with different lengths are considered. Specimen s2 has a length of 20 μm and sample s2.1 is 30 μm long. Since both NTs are picked from the same wafer, they are identical except of their lengths. As s2.1 was measured in a two-point configuration instead of s2 in a four-point, the absolute resistance of both is not

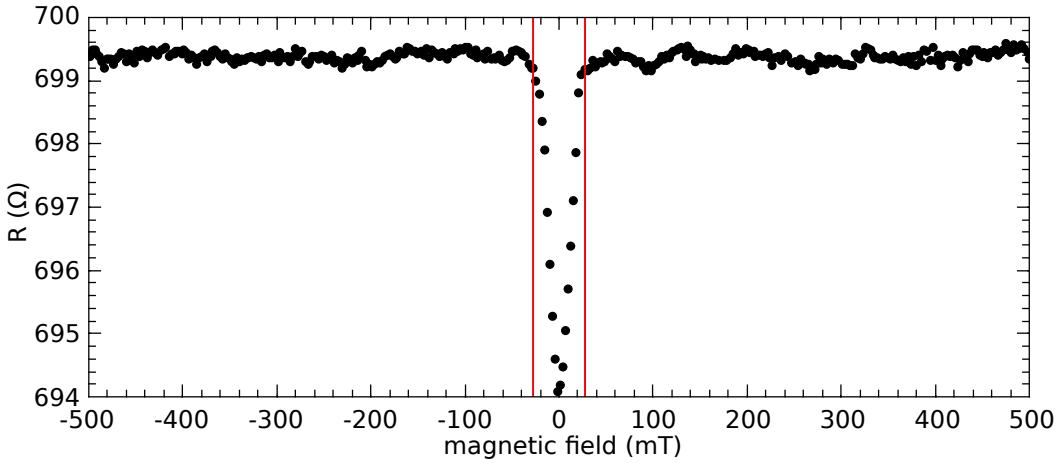

Figure 4.8: AMR measurement of sample s2, with length $L = 30\ \mu$m. The field is applied parallel to the tubes axis. The red lines mark the field positions at which the US is occupied: $H_{\text{sat},\parallel} = \pm(28 \pm 3)$ mT

comparable. However, the AMR signal is almost not affected since the contact resistance is low.

As expected the absolute AMR values of s2.1 0.72±0.05% and s2 0.68±0.05% are equivalent within the error. Additionally, also the field values necessary for saturation along the tubes length are the same: $H^{\text{s2.1}}_{\text{sat},\parallel} = \pm(30 \pm 3)$ mT and $H^{\text{s2}}_{\text{sat},\parallel} = \pm(30 \pm 3)$ mT, confirming a negligible contribution of the demagnetizing energy for the investigated NT-parameters and lengths.

Assuming a US and using the ellipsoid approximation of Eq. (4.5) the difference for both length types is calculated to be only 0.25 mT. This result is also obtained by micromagnetic simulations, conducted without additional uniaxial anisotropy. According to section 4.1.1 the ground state in this case should be mostly magnetized parallel to the tubes axis with only little closure domains forming at its endings.

Influence of temperature during growth of the Py layer

In order to investigate the effects of temperature, during growth of the Py layer, on the anisotropy another sample, denoted s3, is fabricated. The NTs exhibit the same layer composition as s2 and s2.1, namely 1 nm Al_2O_3 / 15 nm Py / 3 nm Al, as well as the same diameter. However, the wafer was heated to 300 °C prior to the Py deposition. Hence the Fe and Ni atoms are expected to experience a higher mobility on the facets.

Fig. 4.9 shows the measured AMR response. The black (red) dots are obtained for the case of parallel (perpendicular) alignment of external field and NT axis. Important positions in the graph are numbered 1-4. The NT is almost in a US, indicated by the low value of $H_{\text{sat},\parallel} < 5$ mT and the resistance at zero applied field. The magnetic state at zero field (position 4 and 2) is no VS, since it otherwise

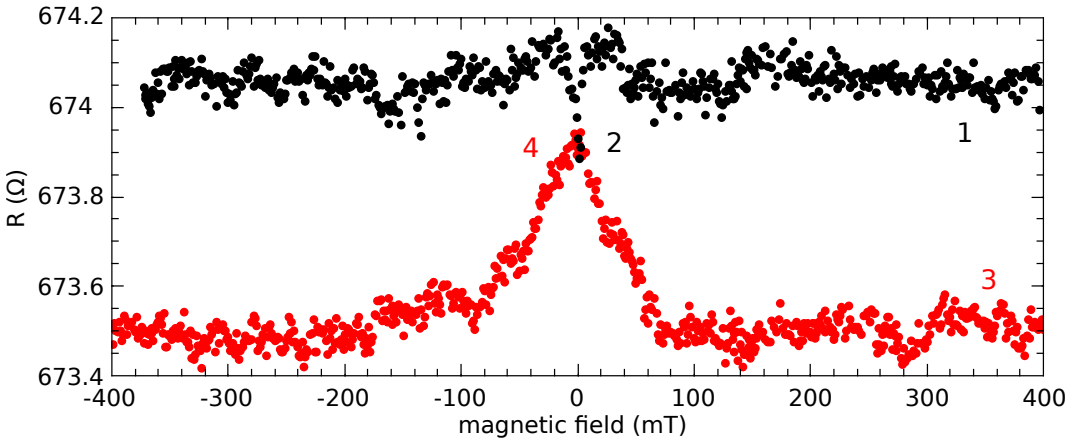

Figure 4.9: AMR measurement of NT type s3. The sample was kept at 300 °C during the Py growth. The external field is either applied parallel (black dots) or perpendicular (red dots) to the tubes axis. Important positions are numbered 1-4.

must exhibit the same resistance as the onion like state at very high external fields (position 3). Furthermore, if the field is applied perpendicularly to the tubes axis, the domain walls forming below 100 mT monotonically transform into the state at zero field (position 3 to 4). As the transition occurs without remanence at position 4, a metastable onion state can be excluded (compare to Fig. 4.5, position 4). A similar continuous transformation is observed between position 1 and 2. Both transitions can only take place if the ground state is a mixed state, consisting of a US with closuring domains at the NTs endings. A simulated mixed state is illustrated in Fig. 4.1 c1) and c2).

The investigated NT is 10 μm long and the distance between the voltage contacts is 4 μm. Since the distance of the contacts is 9 μm for former measurements on s2 the resistance of s3 is also normalized to 9 μm. Hence $R_0^{s3} = 1350\ \Omega$ and $R_0^{s2} = 620.5\ \Omega$ and the resistance increased by a factor of 2. Additionally, the absolute AMR signal is reduced from 0.7% for s2 to 0.09% for s3. Since most of the current is flowing in the Py, both differences indicate a damaged Py layer. Most likely the GaAs experienced thermal decomposition [59], which leads to Ga droplets forming at the surface of the NT. The subsequent deposition of Py leads to intermixing between both metals, reducing the saturation magnetization and the electrical conductivity. Since the temperature during growth is measured by a thermocouple at the sample holder and not directly at the wafer position, it is possible that the temperature at the NTs site may be much higher than the measured value of 300 °C. NTs which Py was deposited at 450 °C showed clear sighs of decomposition with droplet diameters in the range of 50 nm and no AMR signal at all.

In summary, the investigation of s3 shows the expected ground state change, however the sample took damage during fabrication. Hence the reason for the mixed state, appearing at zero field, can not be linked without doubt to the enhanced mobility of the Ni and Fe atoms.

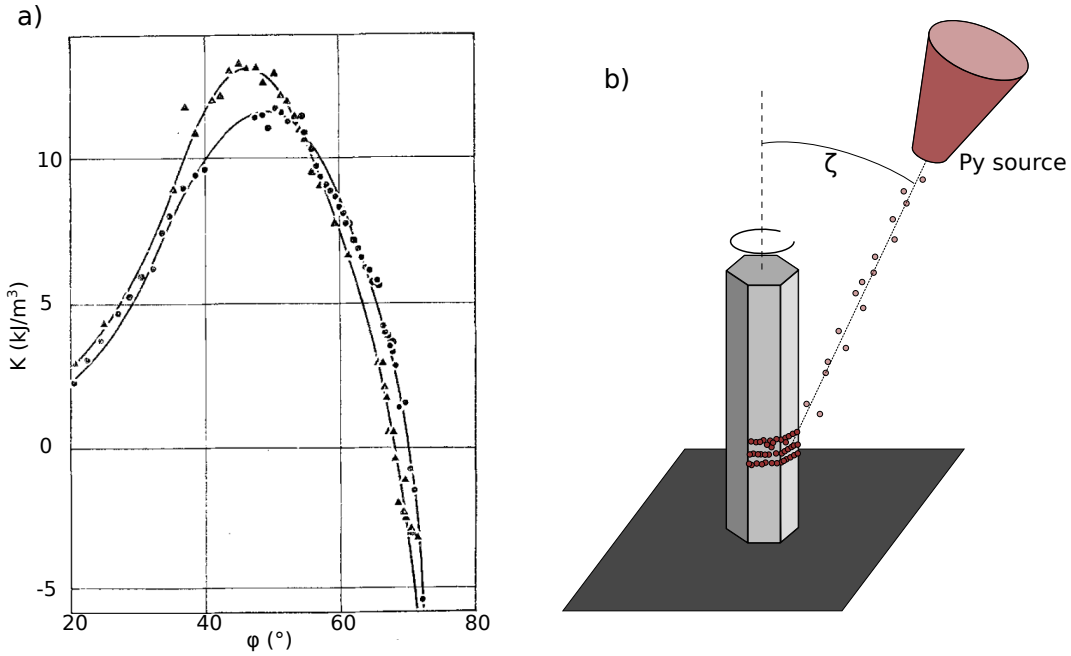

Figure 4.10: a) Dependence of the uniaxial magnetic anisotropy on the angle of incidence for full film Py samples grown on glass discs. φ is the angle between evaporation beam direction and surface normal. Taken from [60]. b) Illustration of the Py chain formation on GaAs NTs during Py deposition. The angle ζ can be related to φ via $\zeta = 90° - \varphi$.

The shadowing effect

The origin of the large uniaxial anisotropy can be explained in terms of a self-shadowing effect occurring during the metal layer deposition. This effect is well known for full-film samples and has been extensively studied [60–63]. A necessary precondition for the occurrence of the anisotropy is a small angle between long axis of the NTs and the Py evaporation beam direction, referred to as ζ. For our MBE chamber $\zeta = 28°$.

Fig. 4.10 a) shows an anisotropy measurement for various angles of incidence $\varphi = 90 - \zeta$, conducted on full film samples. The data was obtained utilizing FMR and the image is taken from [60]. The anisotropy exhibits positive values in case ζ is in the range of $20° - 70°$ and negative values in case $\zeta < 20°$. Positive means the easy axis is oriented perpendicularly to the Py evaporation beam direction. Since $\zeta = 28°$, only the perpendicular case is relevant in the following. During the initial stages of the Py layer formation, small crystallites are randomly forming on the facets of the NTs. These act further as growth nuclei, adopting the crystalline structure of the GaAs. Simultaneously the region behind them is deprived of Py deposition, leading to a shadowing effect that causes crystalline chains to form. These are oriented perpendicularly to the beam direction and thus circle the circumference of the NTs due to rotation during the growth process, as illustrated in Fig. 4.10 b). Thicker layers of Py subsequently fill the depleted regions with polycrystalline Py,

creating a smooth surface for the thicknesses applied in our samples ($15 - 30$ nm). For example NT s1 exhibits a root mean squared roughness of only 0.4 nm (compare Fig. 3.2 e)).

The Py full film samples measured for instance by Smith et al. are grown on thin carbon substrates. The maximal reported anisotropy values are roughly $K_2 = 12 - 13$ kJ/m^3 [60–62] (see for instance Fig. 4.10 a)). In contrast, sample s1 exhibits an anisotropy almost twice as large. This discrepancy is explained by the nearly perfect crystalline structure of the GaAs facets. The substrate order is largely adopted by the in-situ grown Py layer. The crystalline chains thus can become very long without defects, forming a pronounced anisotropy. Fig. 4.11 shows a TEM image of sample s1. The crystalline structure of the Py layer is clearly visible by the atom order parallel to the GaAs facet plane. In the imaged area the chain is visible without major defects. The bright and dark regions within the Py layer are caused by slight thickness variations of the NT slice, induced by the fabrication process of the slice which includes FIB cuts. The averaged thickness of the TEM sample is roughly 100 nm.

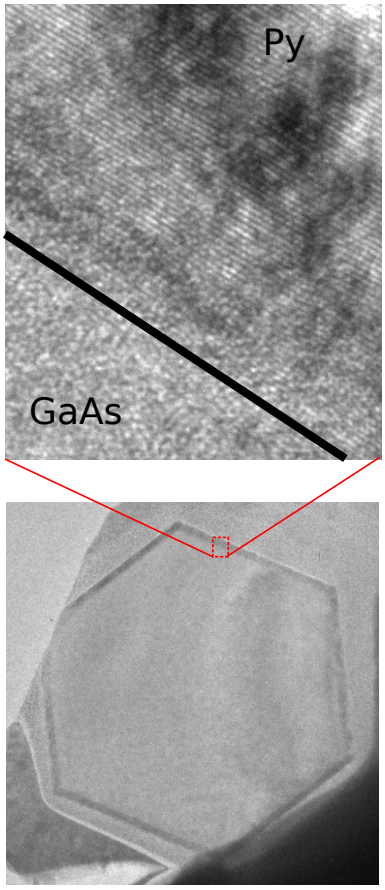

Figure 4.11: TEM image of sample s1. Crystalline chains, parallel to the interface, are visible in the Py layer

Knowledge of the origin of the growth-induced anisotropy enables the discussion of previously presented data in a new context. For example, s1 and s2, whose only difference is the insulating Al_2O_3 layer, show an anisotropy difference of $\Delta K_2 = 8000$ J/m^3. The 1 nm thick buffer layer creates a slightly rougher surface and influences the crystalline growth of the Py layer, due to its amorphous structure.

Almost no growth induced anisotropy was reported by other groups, who also investigated GaAs rods coated with MBE grown Py [17, 18]. Since most of their samples were made without in-situ growth of the GaAs rods and the Py layer, the contact with air causes oxidation of the GaAs surface, which significantly reduces the growth induced anisotropy. In this case the magnitude of the remaining anisotropy is determined by the implemented angle ζ and the measurement shown in Fig. 4.10 a).

Since the anisotropy in Py NTs is generated by a growth induced effect, the magnetic ground state should be tunable by variation of the growth conditions. For instance, different angles ζ are expected to change the growth induced anisotropy, as shown by Fig. 4.10 a). While $\zeta = 90°$ results in zero growth induced anisotropy

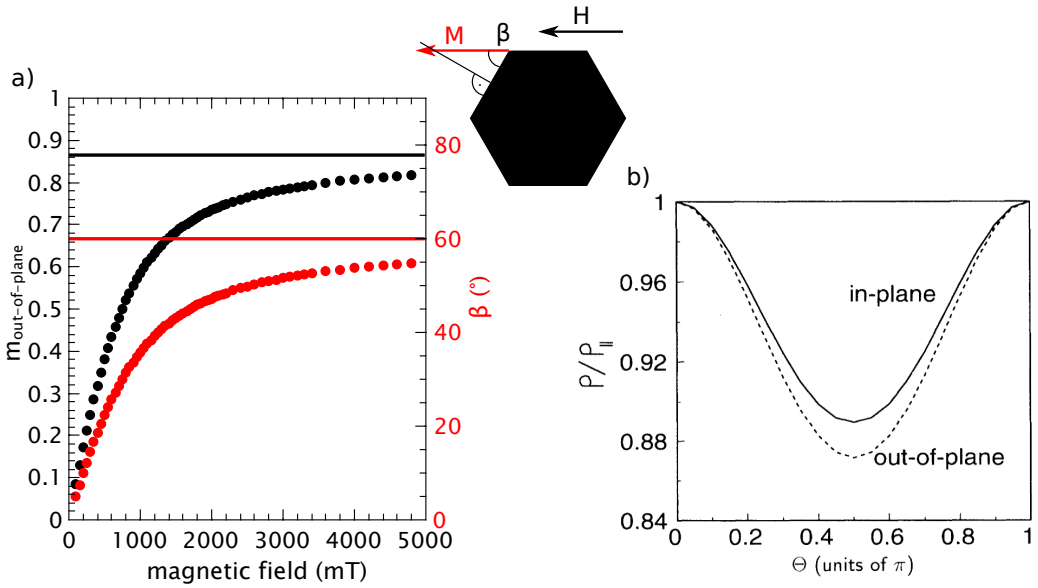

Figure 4.12: a) Out-of-plane component of the facet considered in Fig. 4.2. β refers to the canting angle, which asymptotically approaches 60° for **H** applied perpendicular to the NT and parallel to one facet plane. b) Normalized resistivity in a thin magnetic film for various angles between **M** and **J** if **M** rotates in the film plane (solid line) and out of the film plane (dashed line). Taken from [64].

and $90° > \zeta > 20°$ results in an anisotropy favoring the VS, angles below 20° should favor the US, with magnetization parallel to the tubes axis. NTs with varying angle ζ have not been investigated in the framework of this thesis, since it is difficult to implement various Py evaporation angles into existing MBE chambers. Hence, a more comfortable parameter is exploited to tune the ground state in NTs: The growth temperature. Increasing the mobility of the metal atoms on the facets reduces the anisotropy, since atoms are able to diffuse into the shadowed regions during the initial stages of growth. This has been shown by Smith et al. [62] for full films. Unfortunately, the Py coated GaAs NTs react very sensitively to high temperatures, causing intermixing of the Py and the GaAs layers, as discussed above.

4.1.5 Beyond bulk AMR

The measurements presented in the last subsection are evaluated by treating the AMR response of the VS at zero field and the onion like state for very high fields applied perpendicularly to the NTs axis as equivalent. This statement is, however, only true for the approximation of bulk AMR, where there is no difference for all directions featuring $\mathbf{M} \perp \mathbf{J}$. Diffusive scattering at the surfaces of thin films leads to a reduction in AMR ratio compared to bulk materials. This phenomenon is considered theoretically in [64], where the Boltzmann transport equation in linear response is solved for a free electron gas in the relaxation-time approximation.

Fig. 4.12 b) shows the calculated normalized resistivity of a thin Py film (20 nm) as a function of the angle Θ between $\mathbf{M}$ and $\mathbf{J}$. $\Theta = 0°$ (90°) corresponds to parallel (perpendicular) alignment. The solid line corresponds to an in-plane rotation of $\mathbf{M}$, whereas the dashed line shows a rotation out-of-plane. For both scenarios the line shape is well described by the $\cos^2\Theta$ dependence. The magnitude of the AMR signal is considerably larger for an out-of-plane rotation, compared to an in-plane rotation. This can be understood due to anisotropic scattering. It limits the mean free path of electrons with large velocity components perpendicular to the film plane. Hence, the diffusive scattering at the film boundary is reduced and the resistance decreases, leading to a larger AMR ratio [64].

In the context of magnetic NTs this effect is possible if the field is applied, for instance, perpendicular to the tubes axis as it is the case for the red dots in Fig. 4.5 and Fig. 4.6 a). However these measurements exhibit no decrease in resistance for high external fields and thus no increase in AMR ratio.

To explain this finding micromagnetic simulations are conducted and shown in Fig. 4.12 a). The out-of-plane component of $\mathbf{M}$ is plotted as a function of external magnetic field. Since $\mathbf{H}$ is applied parallel to top and bottom facet, $m_{\text{out-of-plane}}$ is equivalent for the four oblique facets and the maximal achievable out-of-plane tilting angle is 60° with the corresponding $\mathrm{m}_{\text{out-of-plane}} = \sin 60° = 0.87$ in normalized units. This value is approached asymptotically with increasing field. For example at $H = 2$ T, 85% of the maximal tilting angle is obtained.

According to Fig. 4.12 b) the maximal tilting angle translates in an AMR difference for out-of-plane and in-plane magnetization rotation plane of approximately 1%. In contrast, the maximal applied field in the previously shown measurements is 0.4 T (compare Fig. 4.6 b)). The corresponding tilting angle extracted from simulations is 18.7° (≈ 0.1 in units of π). The resulting AMR difference for out-of-plane and in-plane rotation is smaller than 0.1%. Furthermore the effect is not present for top and bottom facets, which additionally reduces the signal by a factor of 2/3. It should be mentioned that reference [64] obtained an AMR ratio of almost 12% for a 20 nm thick Py film, which is at least a factor 16 higher than the values obtained for Py coated NTs examined in this thesis.

In summary the effect is within the noise floor of our measurements presented in Fig. 4.5 and Fig. 4.6 a) and the obtained data is well described by considering only bulk AMR for the investigated field range. Consequently the simulated AMR response in section 4.1.4 was obtained by forming the square cosine of the local angle between $\mathbf{M}$ and $\mathbf{J}$ for all magnetic cells.

4.2 Multi-domain vortex states in magnetic NTs

In this section two NT types are investigated using STXM, described in detail in section 3.6. Besides sample s1, exhibiting a diameter of $\phi_{vv} = 500$ nm and a thickness

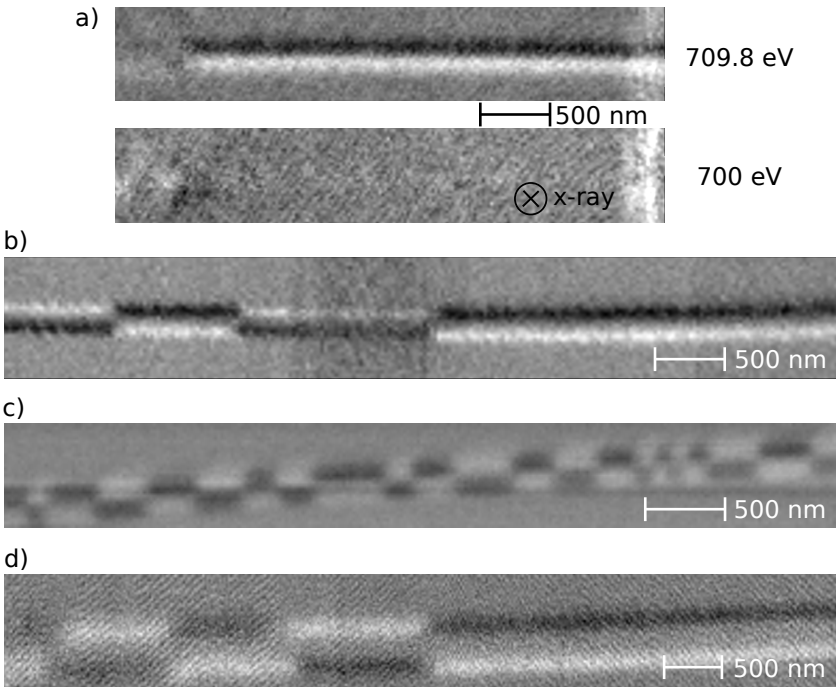

Figure 4.13: STXM images of magnetic NTs obtained at zero field. a) Measurement conducted at the L_3-edge of iron (709.8 eV) compared to the same image taken at 700 eV, confirming the magnetic origin of the contrast. b) and c) images of NT s4. d) Image of NT s1. All NTs shown are in the vortex state with different amount of domains. The diameter of s1 is large enough to identify the top facet as gray stripe, due to annihilation of the signal of top and bottom facet.

of $t = 15$ nm Py a new NT type denoted s4 has been prepared. Sample s4 comprises $\phi_{vv} = 210$ nm and $t = 30$ nm. Both samples are grown without an Al_2O_3 buffer layer so that the Py layer is in direct contact with the GaAs core. Their properties are summarized in table 4.1. In the measurements presented in the following the NTs are placed such that top and bottom facets are parallel to the substrate plane. The X-ray beam is applied perpendicular to the substrate surface. Since STXM is a transmission technique, some states occurring in NTs can lead to annihilation of the magnetic signal. For instance, in the case of a VS, the magnetic contrast from top and bottom facets average to zero, while the oblique facets accumulate their signals. This leads to opposing contrast (black and white) on both sides of the NT, parallel to its long axis and no contrast at the center. An exemplary image is shown in Fig. 4.13 a). The shown images are obtained by calculating the XMCD asymmetry, given by Eq. (3.5). Since two images are necessary, magnetic contrast can also be artificially generated by movement of the specimen during the measurement. To verify the magnetic origin of the contrast a second image was recorded, this time at an X-ray energy of 700 eV. The resulting image in Fig. 4.13 a) shows no contrast at all. This is expected, since at an energy of 700 eV no transitions from the 2p electrons to the unfilled 3d orbitals of iron are possible. Since these are responsible for the magnetic contrast (L_3-edge), the XMCD technique consequently results in zero contrast and Fig. 4.13 a) is identified as global vortex state.

The VS is now exposed to a field larger than 100 mT perpendicular to the tubes axis. The NT enters the OS and after removal of the external field the NT decays into a multi-domain state as shown in Fig. 4.13 b)-d). Multiple application and removal of the external field leads to equivalent domain patterns. This is true as long as the angle of the external field relative to the NTs long axis is kept constant. For instance, application of the field parallel to the NT results in a different domain pattern at zero field, as if the field was perpendicularly aligned. This leads to the conclusion that magnetic pinning is responsible for the multi-domain pattern. A NT without pinning would enter either a global vortex state at zero field, or a state with two vortex domains of opposing chirality separated by a domain wall that is located in the middle of the NT. In simulations it can be shown that the latter state is occupied if the length of the NT is sufficiently large. With the external field decreasing, the VS is simultaneously entered at both NT endings, but with different sense of rotation. At zero field this results in a single domain wall at the center of the NT.

Fig. 4.13 d) shows the magnetic state of sample s1. Since the diameter of the tube is rather large, the effect of cancellation of magnetic contrast of top and bottom facet can be clearly observed. This results in a region at the center of the tube without contrast. The image was taken with the X-rays entering the top facet of the NT at an incidence angle of 30° with respect to the NTs axis. Hence the image gets blurred on the left side due to a low depth of focus.

In the following the behavior of the multi-domain state with field applied parallel to the tubes axis is investigated. Fig. 4.14 shows a hysteresis loop for sample s4. The loop starts at H=80 mT. As the field value is decreased domains start to become visible close to 50 mT. Since the Py layer of NT s4 as well as s1 are in direct contact to the GaAs they are expected to exhibit a similar growth induced anisotropy and thus a comparable field value at which the US is occupied. For s1 this value was determined with AMR to be $\mu_0 H^{s1}_{sat,\parallel} = 53 \pm 3$ mT. Fig. 4.14 confirms this value within the error. $\mu_0 H^{s4}_{sat,\parallel}$ is thus added to the summary in table 4.1. It should be mentioned that the contrast in Fig. 4.14 was not ideally adjusted, making the black and white areas less pronounced compared to the images shown in Fig. 4.13.

As the field decreases the domain walls do not vanish or move, as there is no net torque acting on them. At zero field the NT is in a multi-domain state with 6 domains. The field is then increased to -80 mT. The transition from VS to US occurs by a continuous rotation of all magnetic moments in the direction of the external field. In other words, the domain walls become larger until they merge, creating a US. After the last image at -80 mT is taken, the field was instantly set to zero. As can be seen in the last image of Fig. 4.14 the resulting state is equivalent to the former state at zero field. Only the sense of rotation of the domains changed. Since both states are degenerate, the direction of rotation is arbitrarily assumed and the position of the domain walls is solely determined by pinning.

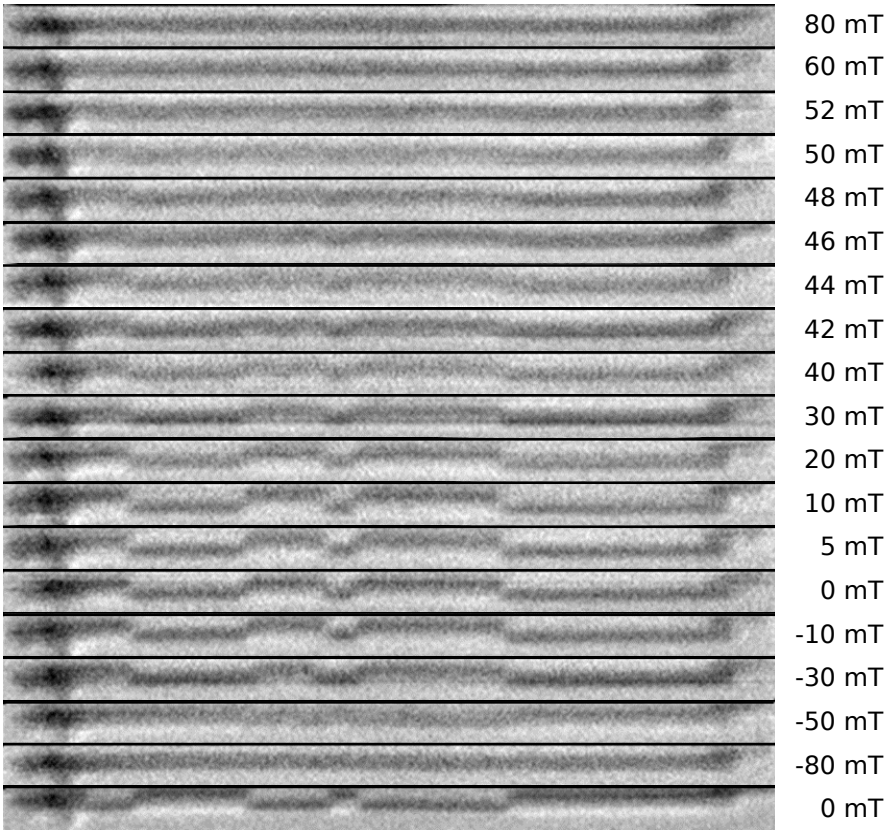

Figure 4.14: Series of STXM images of sample s4 for various external field values. The field is applied parallelly to the tubes axis and starts at 80 mT. The field is subsequently reduced to -80 mT. The last image is taken directly after removal of the external field. The chirality has changed for both images taken at zero field, while the domain positions are unaffected.

4.2.1 Domain wall width

In this subsection the domain wall width Δ_{DW} found in NTs is subject of investigation and the question on the magnetic state at zero field after application of an external field perpendicular to the tube's axis is revisited (compare section 4.1.4).

Fig. 4.15 a) shows a domain wall measured in sample s4. A line scan across the domain wall, following the red line, is used to experimentally determine the domain wall width to $\Delta_{\mathrm{DW}}^{\mathrm{exp}} \approx 140$ nm. This value can be viewed as upper limit, since the spot size of the X-ray beam is approximately 40 nm.

In the following the domain wall width without convoluted beam profile is calculated with an analytical model. To account for the flux closure of the VS, a thin film of infinite lateral sizes with a single Néel domain wall is assumed. Hence only stray fields parallel to the tubes axis within the wall are possible (compare Fig. 2.6 f)). The total energy of the system comprising demagnetizing energy, exchange energy and a uniaxial anisotropy energy as a function of the domain wall width parameter l is displayed in Fig. 4.15 b). It yields a minimum at $l = 20.41$ nm. l is

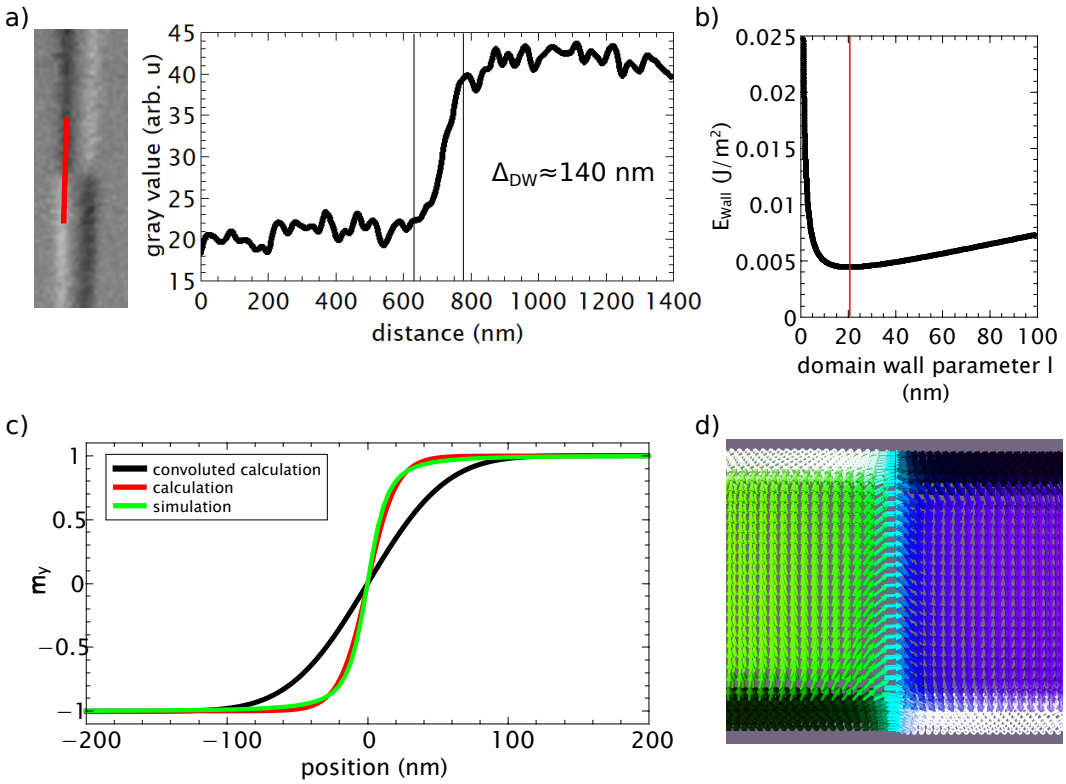

Figure 4.15: a) Measurement of the domain wall width of sample s4 along the red line. The domain wall width is determined to be $\Delta_{\mathrm{DW}}^{\mathrm{exp}} \approx 140$ nm. b) Calculated total energy of the domain wall, including exchange, anisotropy and demagnetizing energy yields a minimum for $l = 20.41$ nm. c) The calculated domain wall profile m_{y} is shown in red. Convolution with a 40 nm Gaussian function (beam profile) leads to the black line, with $\Delta_{\mathrm{DW}}^{\mathrm{calc}} \approx 148$ nm. The green line is a simulated domain wall profile obtained using parameters corresponding to s4. The associated image is shown in d).

linked to Δ_{DW} via Eq. (2.57), hence $\Delta_{\mathrm{DW}}^{\mathrm{calc}} = 64$ nm. The material parameters of s1 are used for the calculation: $A_{\mathrm{ex}} = 1.3 \cdot 10^{-11}$ J/m, $\mu_0 M_{\mathrm{S}} = 1$ T and $K_2^{\mathrm{s1}} = -23$ kJ/m^3. Although the anisotropy of s4 has not been measured directly with AMR, it is found by STXM measurements (see Fig. 4.14) that it is similar to the value obtained for s1 as discussed in the previous subsection.

The same domain wall width is obtained using micromagnetic simulations. The domain wall is forced into the NT by starting with opposing vortex domains at the NT endings. After the relaxation process the domain wall width is determined to be $\Delta_{\mathrm{DW}}^{\mathrm{sim}} \approx 70$ nm. The result is identical for NTs with 250 nm and 500 nm diameter. The latter is exemplary shown in Fig. 4.15 d).

The graph in Fig. 4.15 c) summarizes the obtained domain wall profiles for calculation (red) and simulation (green). Both match very well, confirming the Neèl type nature of the domain wall that was assumed for the calculation. In order to compare the measured value $\Delta_{\mathrm{DW}}^{\mathrm{exp}}$ with $\Delta_{\mathrm{DW}}^{\mathrm{sim}} \approx \Delta_{\mathrm{DW}}^{\mathrm{calc}}$ a convolution with the X-ray beam profile is performed. The resulting domain wall profile is displayed as black

curve in Fig. 4.15 d), yielding $\Delta_{\mathrm{DW}}^{\mathrm{calc,\,conv}} \approx 148$ nm, which is almost equal to the measured value.

Thus, in the following the result $l = 21$ nm will be utilized to estimate the number of domain walls necessary to account for the difference in AMR signal at zero field compared to high fields (≈ 0.4 T) for the measurement on sample s1 presented in Fig. 4.5, where the external field is applied perpendicularly to the NTs axis. Previously the discrepancy was explained in terms of a metastable onion state, however, it is also conceivable that a multi-domain state causes an enhanced resistance at zero field, since every domain wall creates a small region with magnetization parallel to the tubes axis which increases the resistance (denoted x-direction in the following). In order to estimate the contribution of a single domain wall to the AMR ratio the wall profile is expressed as $m_x(x) = 1/\cosh(x/l)$, where m_x is the magnetization component pointing in the x-direction (compare Eq. (2.58)). Since the AMR response depends quadratically on m_x, the contribution of one single domain wall is given by

$$\int_{-\infty}^{\infty} m_x(x)^2 dx = 2l. \tag{4.6}$$

Thus a single domain wall creates an effective length $2l = 42$ nm magnetized in x-direction. For the measurement shown in Fig. 4.5 the distance between the voltage contacts is 9 μm and the resistance difference between black and red dots at zero field is roughly 16.5%. Thus approximately 35 domains are necessary to account for the obtained resistance difference. In other words one domain wall every 250 nm. A comparable domain wall density has been observed, for instance, in Fig. 4.13 c).

In summary the increase in resistance at zero field still has two possible explanations, a multi-domain state and a metastable onion state. A feature that favors the latter, however, is the way the state at zero field is entered. The sweep direction is always from positive to negative fields. The resistance is monotonically rising, while approaching zero field (red graph in Fig. 4.5). Even beyond zero field the resistance is increasing, and suddenly drops. This behavior is expected if a metastable onion state is present, that is transformed into a different onion state with opposite orientation of magnetization at sufficiently large negative field values. In addition the multi-domain state should be entered at positive field values (compare simulations shown in Fig. 4.6 b)). Subsequently the state should stay constant until the same negative field is reached, were it is left again. The measurement should basically look like the red curve in Fig. 4.6 a) or b) with the difference that the resistance at zero field is larger than the high field resistance. In the case discussed above it should be 16.5 % larger compared to the absolute AMR ratio of s4 listed in table 4.1. Hence the onion state is still the most reasonable explanation to account for the increase in resistance when approaching zero field in the measurement shown in Fig. 4.5 (red dots).

4.3 Dynamical properties of ferromagnetic nanotubes

In this section the dynamic properties of individual permalloy NTs with hexagonal cross sections are investigated by means of PMR-based FMR and TRMOKE. The experimental findings are compared to micromagnetic simulations in each subsection. In the framework of this section only homogeneous rf excitation is discussed. First the high-field response is analyzed, where the dependence of the mode patterns to the alignment of the external field with respect to the NTs direction of rotation around its long axis is highlighted. The modes of the top facet are optically accessible and presented in the following subsection. Finally the section concludes with an analysis of mode patterns at zero field. These are fundamentally different to modes appearing in high field because of the (multi-domain) vortex ground state.

4.3.1 Mode patterns in high field probed with PMR

In this subsection the magnetic response to rf excitation is analyzed by PMR-based FMR.[1] The technique is described in detail in section 3.5. Once fabricated every micro resonator has a fixed eigenfrequency given by the cavity geometry. This frequency is approximately 13.7 GHz for all resonators used in the following. Corresponding micromagnetic simulations are conducted at the same excitation frequency.

In the following the NTs s1 and s4 are investigated. Their properties can be found in table 4.1. Fig. 4.16 a) and b) show two different NT arrangements within the cavity. While in a) two facets are perpendicular to the substrate normal, in b) two facets are parallel to it. These positions are denoted position 1 and position 2 in the following and the coordinate system is chosen such that x is parallel to the tube's axis and z is normal to the substrate plane. The rf excitation field is always normal to the substrate plane and homogeneous within the cavity. An external in-plane field $\mathbf{H}$ with strength up to 2 T can be applied and rotated in the xy-plane indicated by the angle Θ.

Fig. 4.17 shows PMR measurements in a) and c) and the corresponding micromagnetic simulations in b) and d), respectively. Sample s4 is considered in a) and b) and the results of sample s1 are presented in c) and d). In a) and b) (c) and d)) the NTs are placed according to position 1 (position 2) introduced in Fig. 4.16. The line scans shown are obtained either for $\Theta = 0°$ or $90°$. The black (measurements) or red (simulations) arrows relate the exemplarily selected line scans to the full angular dependences. The intensity of the simulations is arbitrary and depends on the number of cells. However, since the cell number is kept constant for equal diameters (8×256×256 for s1 and 8×128×128 for s4) the relative intensity of

[1] The measurements have been conducted at the Helmholtz-Zentrum Dresden-Rossendorf (HZDR) under the supervision of Dr. J. Lindner.

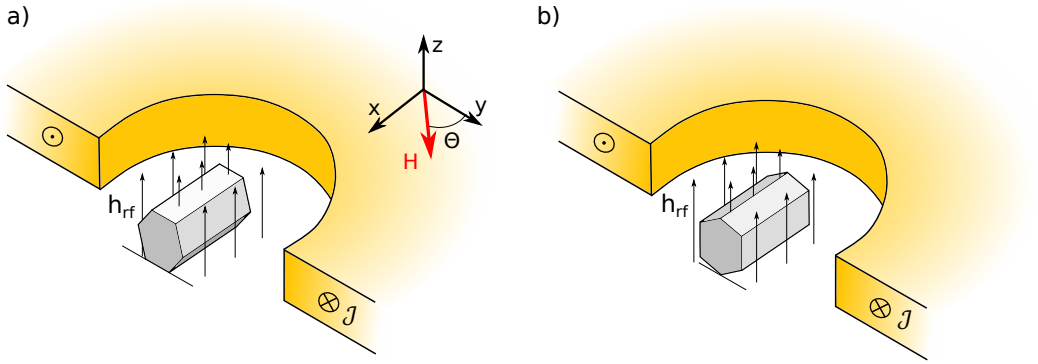

Figure 4.16: The NTs are placed such that their axis are parallel to the x-axis and the external magnetic field $\mathbf{H}$ can be rotated in the xy-plane, indicated by the angle Θ. The z-axis is parallel to the substrate normal. a) and b) show schematic cross sections of the PMR. While in a) the NTs facet is parallel to the substrate (position 1) in b) the hexagonal tube is rotated by 30°, hence only the edge is touching the substrate (position 2). The rf current J generates a homogeneous out-of-plane rf field h_{rf} across the whole sample.

different line scans is comparable. The simulations are conducted with PBCs on a cross sectional area of a NT (compare AMR simulations in section 4.1.4). Hence mode patterns parallel to the NTs axis are neglected. Since measurements on s1 and s4 are each conducted on a single NT, the measured intensities are also comparable for sample s1 and s4, respectively. Measuring for instance sample s1 with two NTs of different length would result in an intensity difference since the filling factor (Eq. 3.3) of the cavity consequently changes. Due to lock-in technique the derivative of the absorbed intensity is detected. Hence the measured curves are the derivatives of Lorentzian-type absorption peaks with negative (white) and positive (black) slope.

For $\Theta = 0$ homogeneous FMR on all facets is encountered at 200 mT for s4 (compare Fig. 4.17 a)). In this arrangement the magnetic response of the NT is almost as a full film, with slight disturbances originating from the six edges of the NT. These disturbances result from different internal fields due to the curvature at the edges. Hence the resonance conditions are unequal and FMR appears at different applied field values within the volume of the edges. Using Eq. (2.27) a full film response, without considering anisotropies, is calculated to be at $H^{s4}_{\mathrm{FMR,\,calc}} = 183$ mT, which is reasonably close to the measured ($H^{s4}_{\mathrm{FMR,\,mes}} = 200$ mT) and simulated ($H^{s4}_{\mathrm{FMR,\,sim}} = 180$ mT) values. Since the measurements are conducted at 13.7 GHz the influence of anisotropies can be neglected for the calculation.

The same arrangement but for sample s1 leads to a slightly different behavior. The FMR response is shifted to higher field values. The simulated and measured FMR positions are $H_{\mathrm{FMR,\,sim}} = 245$ mT and $H_{\mathrm{FMR,\,mes}} = 277$ mT (compare Fig. 4.17 c) and d)). Since both simulation and measurement behave equally, the shift in resonance position is attributed to a changed energy landscape (exchange as well as dynamical demagnetizing energy) due to a varying thickness to diameter ratio $\phi_{vv}/t \approx 33$ for s1 and 8 for s4.

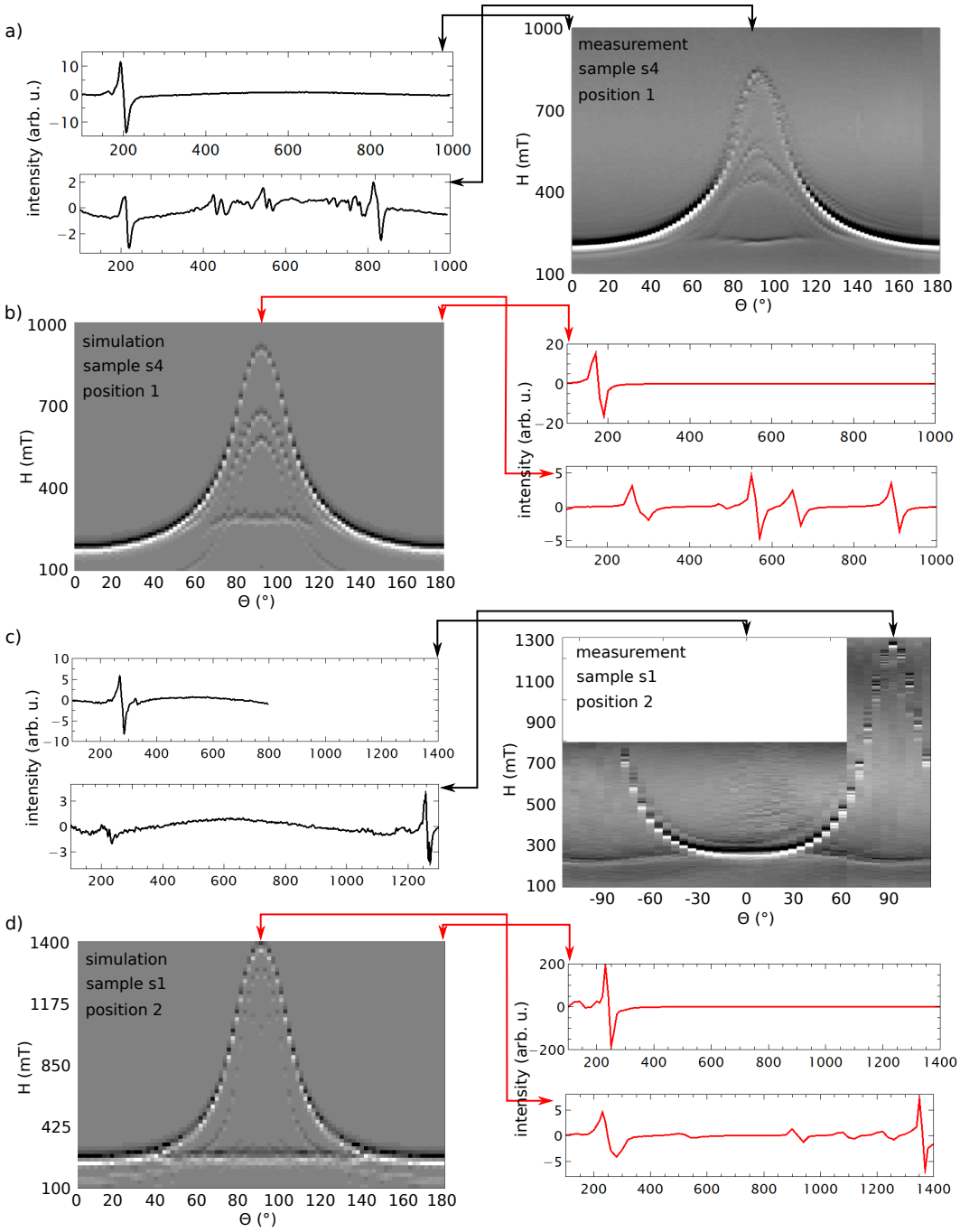

Figure 4.17: a) PMR-based FMR measurement of sample s4 and the corresponding simulation shown in b). The NT is positioned according to position 1 in Fig. 4.16 b). c) PMR-based FMR measurement of sample s1 and the corresponding simulation shown in d). The NT is positioned according to position 2 in Fig. 4.16 c). The line scans are obtained at 0° and 90° for all shown angular dependences, indicated by the red and black arrows. Since no additional resonances are expected in the white area in c), the measurement has not been conducted for these regions due to very long recording times.

The situation becomes much more complicated when the field is applied perpendicularly to the tube's axis ($\Theta = 90°$). Depending on the direction of rotation the NT can exhibit a variety of complex mode patterns. First s4 is considered in the following. The NT is located in the planar microresonator according to position 1 and thus top and bottom facets are parallel to the external field. Hence both facets undergo FMR at roughly $H^{s4}_{\text{FMR, mes}} = 215$ mT, leading to a signal that is 6 times smaller than the FMR response if the field is applied parallel to the tube's axis. As only 1/3 of the facets undergo FMR one might expect a difference of a factor of 3. However, the FMR signal is not homogeneous across the two facets, but rather localized at their center, leading to a decreasing signal. This can be seen in the first images of Fig. 4.18 a) and b).

In addition at low external field values there are traveling excitations that move around the circumference of the NT. These modes are very weak compared to, for instance, the in-plane FMR response and originate from the inhomogeneous precession of $\mathbf{M}$ at the edges of the NT. If frequency and k-vector match the dispersion relation of the NT this driving field can excite spin waves. The moving patterns start to disappear for higher field values and are not present above approximately 350 - 400 mT.

As the external field is increased above this value two pronounced intermediate modes appear at $H^{s4}_{\text{INT1, sim}} = 570$ mT and $H^{s4}_{\text{INT2, sim}} = 640$ mT. Their intensity mode profiles are displayed in Fig. 4.18 a). The standing wave patterns are features of the hexagonal geometry of the NT and can not be explained in simple terms. The final mode, at $H^{s4}_{\text{OOP, sim}} = 900$ mT, is an out-of-plane excitation appearing at both left and right vertexes (see Fig. 4.18 a)). Since the magnetization within the facets is not able to align with the external magnetic field at finite values, the modes are localized at left and right vertices. This results directly from the Stoner-Wohlfarth model [65], if $\mathbf{H}$ and $\mathbf{M}$ are neither perpendicular nor parallel. It can also be seen in the asymptotic behavior of $m_{\text{out-of-plane}}$ approaching high external fields in Fig. 4.12 a).

In the following position 2 with $\Theta = 90°$ is discussed for NT s1. The measurement presented in Fig. 4.17 c) shows no intermediate resonances. However, a standing wave close to the former FMR response appears at 260 mT. Although, the transition of this mode to the FMR mode of position 1 shown in Fig. 4.19 seems to be of continuous nature, visualization of the mode (compare Fig. 4.18 c)) reveals a different structure, with little in common with a homogeneous FMR excitation. Since the mode appears at field values below 350 - 400 mT it is accompanied by traveling spin waves, which make the intensity profile in Fig. 4.18 c) look slightly asymmetric.

The final mode found at very high fields is the out-of-plane response of the left and right facet at $H^{s1}_{\text{OOP, mes}} = 1260$ mT. Note that its profile is, similar to the in-plane FMR response, not homogeneous across the facets. Higher order patterns of the out-of-plane mode occur at lower field values and are shown in Fig. 4.18 c) for 1100 mT and 1240 mT. Utilizing the out-of-plane resonance condition for a full film (Eq.

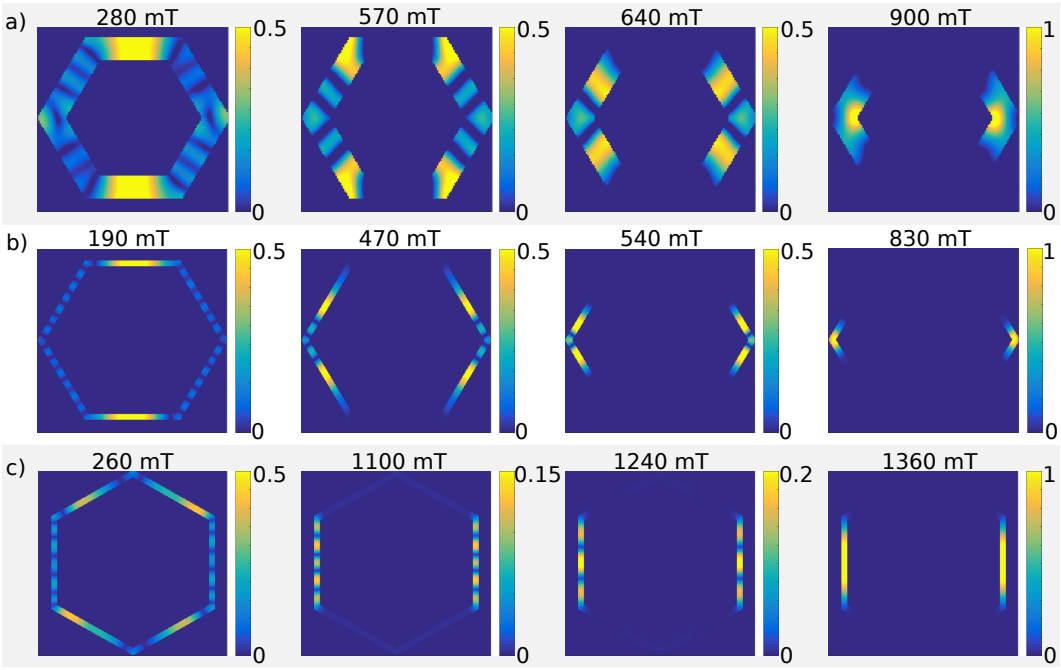

Figure 4.18: Simulated intensity mode profiles for different field strengths and NT geometries at an excitation frequency of 13.7 GHz. **H** is applied perpendicularly to the tube for all shown simulations ($\Theta = 90°$). The images are produced calculating the absolute square of two snap-shots shifted in phase by 90°. a) Mode profiles simulated according to the sample parameters of s4 and position 1 in Fig. 4.16. The corresponding line scan is shown in Fig. 4.17 b). b) Mode profiles simulated according to the sample parameters of s1 and position 1 in Fig. 4.16. c) Mode profiles simulated according to the sample parameters of s1 and position 2 in Fig. 4.16. The corresponding line scan is shown in Fig. 4.17 d).

(2.30)) gives $H_{\text{OOP, calc}} = 1460$ mT. Since the facet is magnetized out-of-plane the demagnetizing energy is approximately changed according to Eq. (4.5). Using the facet thickness $t = 15$ nm and facet width $L = 250$ nm finally yields $H_{\text{OOP, calc}} = 1400$ mT. Hence treating the facet as individual stripe results in a good approximation of the simulated out-of-plane resonance field.

The measured ($H^{s1}_{\text{OOP, mes}} = 1260$ mT) and simulated ($H^{s1}_{\text{OOP, sim}} = 1360$ mT) out-of-plane resonance fields differ by 100 mT. This discrepancy can be understood considering Fig. 4.19. The image shows the simulated magnetic response of a NT rotated around its long axis from position 1 to position 2 in steps of 2.5°. As can be seen even very little tilting angles can have a huge influence on the mode structure. Considering the out-of-plane response at position 2, a small deviation from the exact angle leads to a decreasing external field at which the mode appears. This behavior is expected, since the out-of-plane angle increases from position 1 to position 2, where it reaches its maximum value of 90° and **H** is perpendicular to two facets (compare Fig. 4.16 c)). Since the measured NT is positioned with a precision of approximately $\pm 10°$, a slight misplacement is likely related to the shift in out-of-plane excitation field.

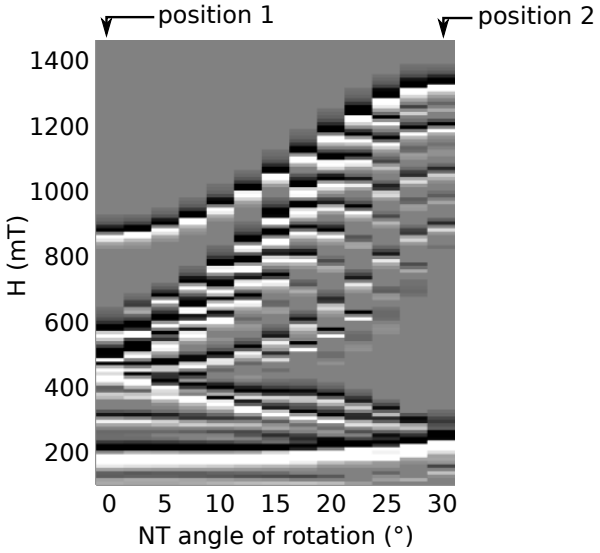

Figure 4.19: Simulated mode transition from position 1 to position 2 introduced in Fig. 4.16 b) and c). In the process the NT is rotated in steps of 2.5° around its long axis. The mode profiles at position 1 and 2 are shown in Fig. 4.18 b) and c), respectively. The simulation corresponds to the sample parameters of s1 and is conducted at a homogeneous excitation with a frequency of 13.7 GHz.

Finally, sample s1 and s4, both in position 1 are compared. The main difference between both NT types is the Py thickness to diameter ratio ($\phi_{vv}^{\mathrm{s1}}/t_{\mathrm{s1}} \approx 33$ and $\phi_{vv}^{\mathrm{s4}}/t_{\mathrm{s4}} \approx 8$). Although the ratio differs drastically, the mode patterns are almost identical (see Fig. 4.18 a) and b)). While the in-plane and out-of-plane FMR modes are expected to be similar, surprisingly also the intermediate modes appear at only slightly shifted field values. As a minor difference between s1 and s4, the modes appearing in s1 are more localized to the left and right vertices of the NT. Thus the intermediate mode at 470 mT becomes fully visible in s1, whereas in s4 its maximum intensity is very close to top and bottom facet.

These findings lead to the conclusion that the mode patterns are almost insensitive to geometrical changes, as long as the NT is hexagonally shaped.

4.3.2 Lateral resolution obtained with TRMOKE

Since PMR-based FMR is an averaging method and the simulations are conducted on a thin cross sectional area of a NT, TRMOKE is utilized to obtain information of mode patterns on the facet planes. This technique is described in detail in section 3.4 and the NT is placed according to position 1 introduced in Fig. 4.16 b). Since TRMOKE is based on the reflection of near infrared light, only modes appearing on the top facet are accessible. Furthermore the external field is limited to 300 mT and is applied in the plane defined by the top facet. The resolution is limited by the diffraction limit of visible light to some hundreds of nanometers. Hence in the following only sample s1 with a comparably large facet width of 250 nm is considered.

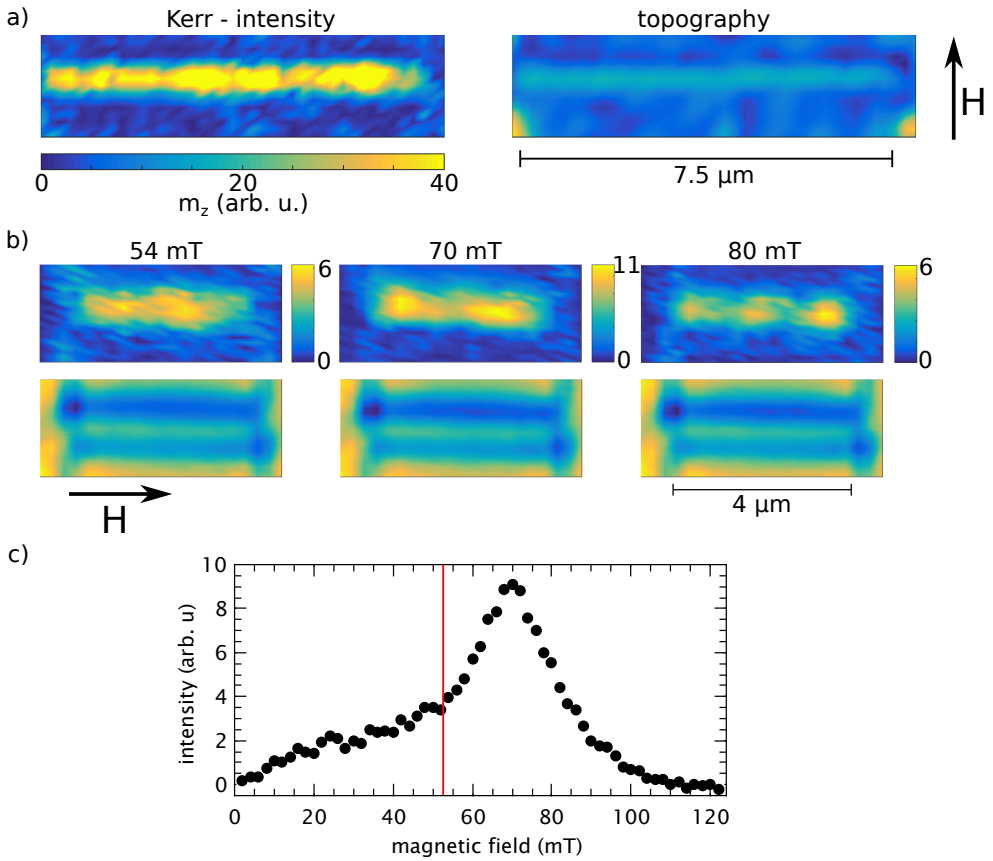

Figure 4.20: Measurement of the Kerr rotation utilizing TRMOKE. The intensity images are generated by taking the absolute square of two measurements shifted by a phase of 90°. a) The measurement was conducted on a 7.5 μm long tube at H = 800 mT, applied perpendicularly to the NTs axis. b) The NT is 4 μm long and the external field is applied parallel to the NTs axis. c) Every point in the graph corresponds to a Kerr-intensity measurement as the ones exemplarily shown in b). All pixels of a single image were added together to generate one point in the graph. The red line marks $H^{s1}_{sat,\parallel}$.

The NTs investigated in this subsection are positioned in the gap of a CPW (compare Fig. 3.7 b1)). Thus the rf excitation is oriented out-of-plane with respect to top and bottom facets. Fig. 4.20 summarizes the results obtained for non-zero external field. The intensity images show the Kerr rotation and are generated by calculating the absolute square of two single images, shifted by a phase of 90°. The topographic images are simultaneously recorded by calculating the sum signal of both photodiodes and essentially show the NT through an optical microscope (objective lens with 100x magnification).

Fig. 4.20 a) shows sample s1 cut to a length of 7.5 μm. The NT is excited homogeneously with a frequency of 10 GHz. The field is applied perpendicularly to the NTs axis. At H = 80 mT a homogeneous FMR pattern appears. The NT is in an onion state and resonance can only occur at top and bottom facet. The mode is identical with the FMR mode shown in Fig. 4.18 b) at 190 mT. However, it is shifted

to smaller field values, since the excitation frequency is reduced from 13,7 GHz to 10 GHz.

The field is now applied parallel to the tube's axis. The tube is cut to 4 μm and the excitation frequency is reduced to 5 GHz. The frequency as well as the tube length are reduced in order to clearly separate different mode patterns in space and frequency. The lower frequency reduces the line width (compare Eq. (2.32)) and the decreased length increases field differences between mode patterns (compare Eq. (2.37)). As the field increases a homogeneous FMR pattern starts to develop as shown in Fig. 4.20 b). This corresponds to the mode recorded in Fig. 4.17 c) for $\Theta = 0°$. The maximal Kerr-signal is obtained close to 70 mT. The mode pattern at 70 mT is not a homogeneous FMR, but an overlap with the third higher order mode (confined higher order modes are illustrated for instance in section 2, Fig. 2.3). At 80 mT the FMR signal is already decreasing and a fifth higher order mode pattern starts to emerge. These modes can not occur in the simulations discussed in the last subsection, due to applied periodic boundary conditions. In contrast, they can be identified in the PMR-based FMR measurements on NT s1. In Fig. 4.17 c) one higher order mode appears at slightly larger fields than the dominant FMR response for $\Theta = 0°$. Note that the NT in the former measurement is longer than the one discussed in this subsection, thus the distance in field between FMR and higher orders is smaller.

An interesting feature can be identified considering Fig. 4.20 c). Every point of the graph is generated from a single intensity image by summing over all pixels. Since the images have the same size the graph displays the relative Kerr intensity. The absorption peak shows a typical Lorentzian line shape with a maximum at 70 mT. The higher order modes described earlier are located within the line width of the FMR response. The Lorentzian shape is only valid for fields larger than 50 mT, marked by the red line in Fig. 4.20 c). This behavior can be explained in terms of a change in the magnetic state. From AMR measurements it is known that sample s1 requires approximately 50 mT in order to enter the uniform state (compare section 4.1.4, Fig. 4.5). Before this threshold a continuous transition from VS to US takes place, changing the absorptive properties of the NT. This leads to the conclusion that the higher order modes shown in Fig. 4.20 b) are backward volume like modes, since $\mathbf{M} \parallel \mathbf{k}$.

4.3.3 Mode patterns in zero field

The external field is now removed. Consequently the ground state is occupied, which is either a global vortex state or a multi-domain vortex state, as discussed in section 4.2. For the simulations, summarized in Fig. 4.21, a global vortex state is assumed. The magnetic response for various rf frequencies is simulated by application of a short, homogeneous excitation pulse and a subsequent fast Fourier-Transformation (FFT) of a 4 μm long NT with sample parameters of s1 (compare table 4.1). The

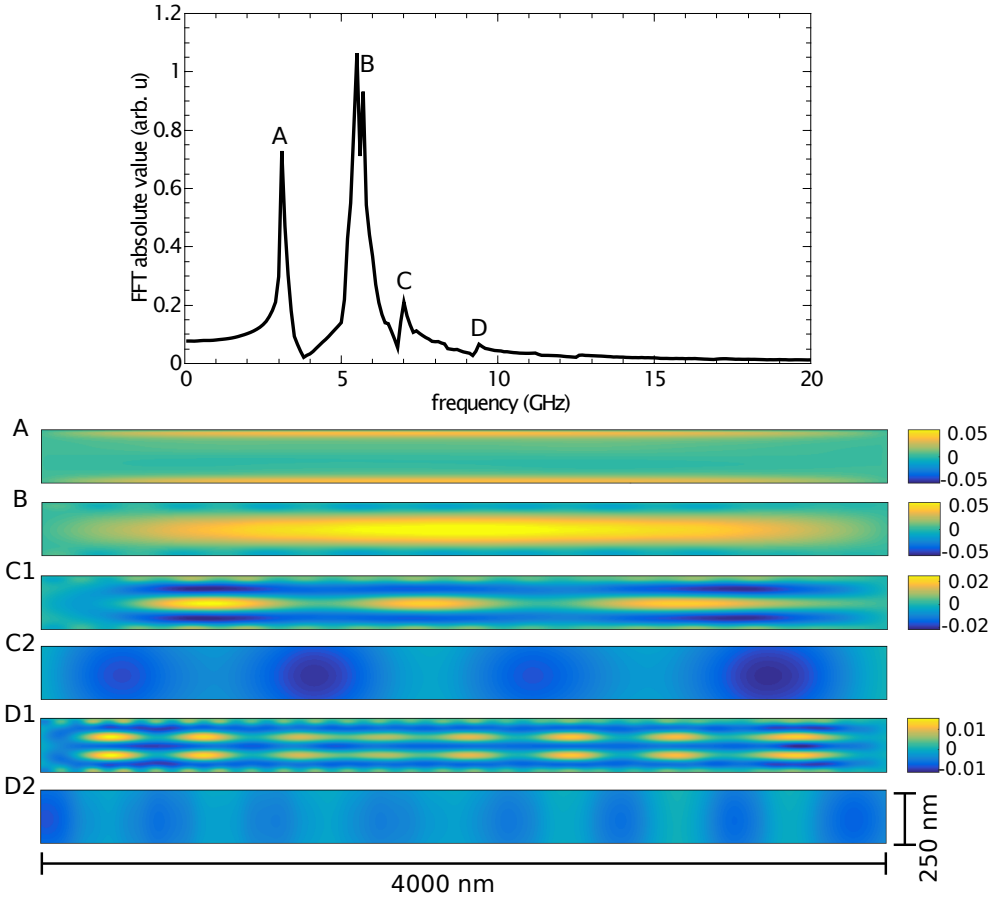

Figure 4.21: Simulated magnetic response of a NT, with sample parameters according to s1, in zero external field. The mode profiles are alphabetically numbered and plotted for the top facet below the graph. A: edge mode at 3.1 GHz, B: in-plane FMR mode at 5.5-5.7 GHz, C: first higher order mode at 7 GHz, D: second higher order mode at 9.4 GHz. C2 and D2 are obtained by convolution of C1 or D1 with the beam profile of the laser used in TRMOKE measurements.

graph in Fig. 4.21 displays the absolute square of the FFT. A variety of peaks can be identified, labeled A,B,C, and D. The corresponding mode profiles are shown below in Fig. 4.21. Only the top facet is displayed in the images.

The first magnetic response (A) is an edge excitation. It can be imagined as FMR response, occurring only at the edges of the volume. The facets exhibit in-plane FMR at larger frequencies (5.5-5.7 GHz (B)). This difference is induced by the curvature at the edges, which changes $\mathbf{H}_{\text{eff}}$ due to the different exchange and demagnetization energy contributions. Because of this the in-plane FMR resonance is maximal at the center of the facet planes. The first pronounced higher order mode (C) shows three peaks parallel to the tube's axis and two valleys perpendicular to it. The wavelength in both directions is determined by the lateral dimensions of the top facet. Since the magnetization is in a vortex state the parallel mode exhibits $\mathbf{M} \perp \mathbf{k}$. A similar behavior is observed for the second higher order mode at 9.4 GHz.

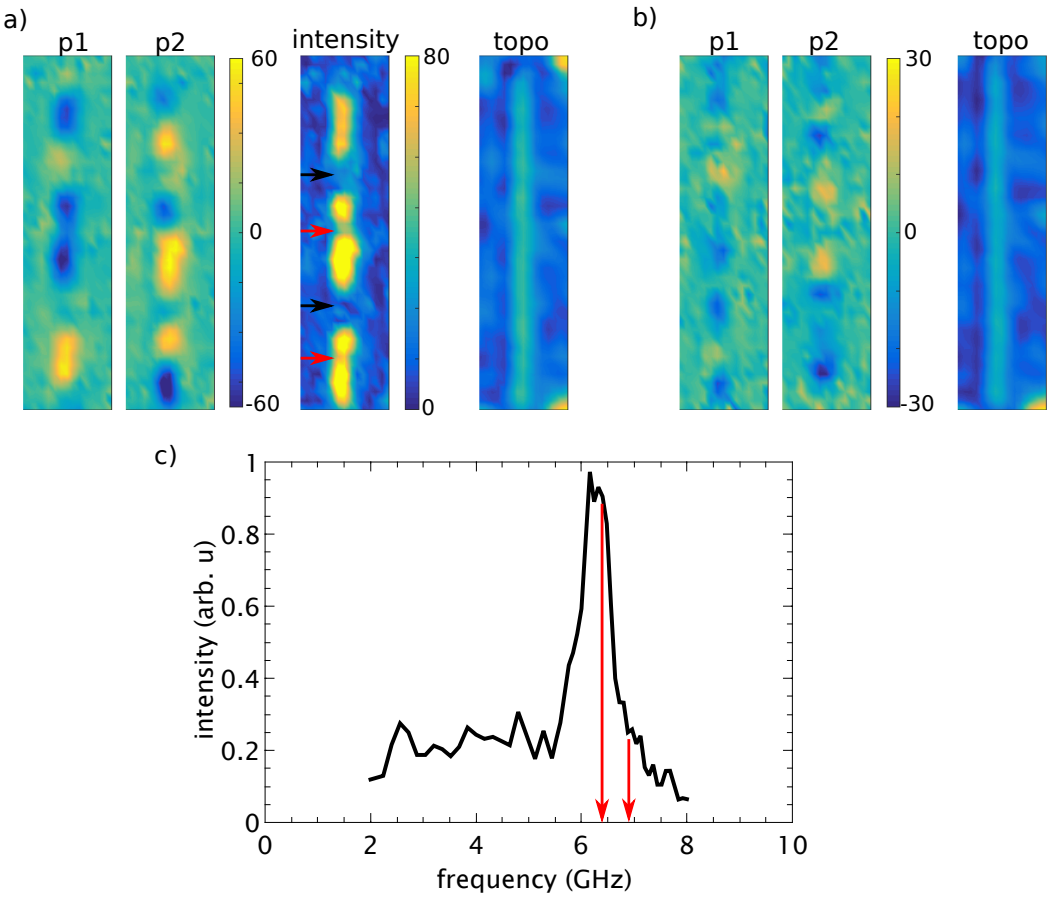

Figure 4.22: TRMOKE measurements of sample s1 cut to a length of 7.5 μm. All images are recorded at zero external field. p1 and p2 are two measurements shifted by a phase of 90°. The intensity image is obtained by taking the absolute square of images p1 and p2. Large and small areas with vanishing Kerr signal are marked with black and red arrows in the intensity image, respectively. The topo image displays the actual sample observed through a objective lens with 100-times enlargement. The excitation frequency is a) 6.4 GHz and b) 6.9 GHz. The graph in c) shows the relative intensity, obtained from integration over the intensity images. The image positions of a) and b) are highlighted with red arrows.

Since the TRMOKE setup operates with laser light with a wavelength of 800 nm, the resolution is approximately given by the diffraction limit of visible light ($\approx \lambda/2$). The beam profile is approximated by a Gaussian function with corresponding sigma. A convolution with the mode patterns found on the top facet (Fig. 4.21) can be used to reproduce the measured signal. C2 and D2 show the result when the mode profile of C1 and D1 is convoluted, respectively. The pattern perpendicular to the NT axis is completely canceled out and thus undetectable by the setup. Only modes parallel to the NT can be observed. In addition the resolution is limited by the width of the top facet (250 nm) which is smaller than the laser beam profile (diameter is approximately 400 nm). The neighboring oblique facets do not contribute to the magnetic signal, since they reflect the incoming laser light away from the detection unit.

Fig. 4.22 shows the measurements conducted at H = 0 and position 2 introduced in Fig. 3.7. In Fig. 4.22 c) the Kerr intensity as a function of frequency is shown. It is obtained by calculating the absolute square of two phases shifted by 90°. Subsequently every intensity image is summed up to one single value displayed in the graph. A maximum intensity can be observed around 6.3 GHz. This magnetic response looks similar to the simulated FMR mode visualized in Fig. 4.21 B. However, considering the actual images the mode is not homogeneous across the NTs length. This behavior can only be explained if the magnetic ground state is no global vortex state, but a multi-domain state, as discussed in section 4.2. Due to this, the interpretation of the mode structures becomes extremely difficult, especially because the single vortex domains can exhibit a relative phase between each other. This behavior can be seen for the FMR mode shown in Fig. 4.22 a) by regions of blue and yellow color. Domain walls are identified in the intensity image, where no resonance takes place.

Since the resolution of the laser spot is approximately 400 nm, domains with smaller lateral dimensions may not be resolved and can lead to misinterpretation concerning the number of observable domains in the intensity images. In section 4.2 Fig. 4.13 c) vortex domains with a length as small as 100 nm have been found by STXM. Thus the Kerr contrast in a region with multiple vortex domains could average out if the domain width is sufficiently small. Since domain walls in the investigated NTs usually have a width below 80 nm (compare section 4.2.1), the large gaps between regions of resonance appearing in the intensity image (black arrows in Fig. 4.22 a)) are explained in terms of this averaging effect. This claim is additionally supported by the appearance of very small separating regions also visible in the intensity image, marked with red arrows.

Comparing the intensity graphs obtained for simulations (Fig. 4.21) and measurements (Fig. 4.22 c)) a major difference is the edge mode. It is completely missing in the measurements. As the mode is only located at the edges of the hexagonally shaped NT this characteristic is expected, since the corresponding laser light gets deflected and is unable to enter the detector.

Fig. 4.22 b) shows a much weaker mode structure appearing close to 7 GHz. According to the simulations a higher order mode is expected at this frequency range. The mode structure is similar to the FMR response but exhibits more peaks and valleys. Hence it is likely a higher order mode. However, some uncertainty remains, especially because of the low signal-to-noise ratio and the limited resolution. Considering the intensity graph the mode lies within the line width of the FMR mode. In contrast, these modes are separated in the simulations shown in Fig. 4.21. This difference may be attributed to the length of the NT, which is 7.5 μm for the measurements and only 4 μm for the simulations. In longer NTs the higher order modes will shift closer to the FMR peak.

4.4 Spin waves in hexagonally shaped nanotubes

In this section the rf excitation is not homogeneous across the specimen. Instead it is reduced to a small area in the middle of the NT. This is experimentally realized using gold stripes or small coplanar waveguides with a width less than 1 μm. This geometry enables the creation of spin waves for certain frequencies. First the mode patterns are simulated and different local excitation geometries are discussed. The results are subsequently compared to measurements conducted with TRMOKE. Zero field and high external fields can lead to regions in which spin waves can exclusively travel. This is exemplarily shown for the onion state. Finally a simulated dispersion relation for hexagonally shaped NTs is compared to STXM measurements conducted on NT s4.

4.4.1 Simulated mode patterns

The simulations presented in this subsection are conducted on a NT with length $L = 10$ μm at zero external field. Since the TRMOKE setup resolution is limited to the diffraction limit of visible light, only sample s1 with a facet width of 250 nm is considered in the measurements and the associated simulations. The spin waves are locally excited on one facet with an in-plane rf field. The excitation is sinusoidal in time and homogeneous within an area of width w in the bottom facet (black regions in Fig. 4.23). The frequency is varied between 2 - 10 GHz. In the experiment only one facet is in direct contact to the gold stripe (compare Fig. 4.24 a)). Hence, the majority of the driving field above the stripe is oriented in-plane and restricted to a relatively small area, which justifies the simplifications applied in simulations. In order to reduce spin wave reflection at both ends of the NT, the intrinsic Gilbert damping constant is gradually increased within the last 0.5 μm in the simulations.

Fig. 4.23 shows snapshots in time of top (t) and bottom (b) facet for various frequencies. The excitation is located on the bottom facet at the black area. Below 3 GHz the dispersion relation does not match the given frequency and spin waves are unable to leave the vicinity of the antenna, instead the decay exponentially with increasing distance. At around 3 GHz edge modes are excited (not shown). The first spin waves traveling on the facet planes appear at 4 GHz. The spin waves exhibit a different intensity on both sides (+ and -) of the region of excitation. Although this effect can have several causes when conducting experiments, in the case of simulations it is very likely connected to an antisymmetric dispersion relation. In the following two possible causes are discussed together with an explanation why they are excluded from simulations. 1) A realistic driving field of a stripe antenna would exhibit out-of-plane and in-plane components. This introduces a chirality that causes a different response in the LLG for both directions. In simulations this effect is not present, since the driving field is homogeneously oriented in-plane. 2) Damon

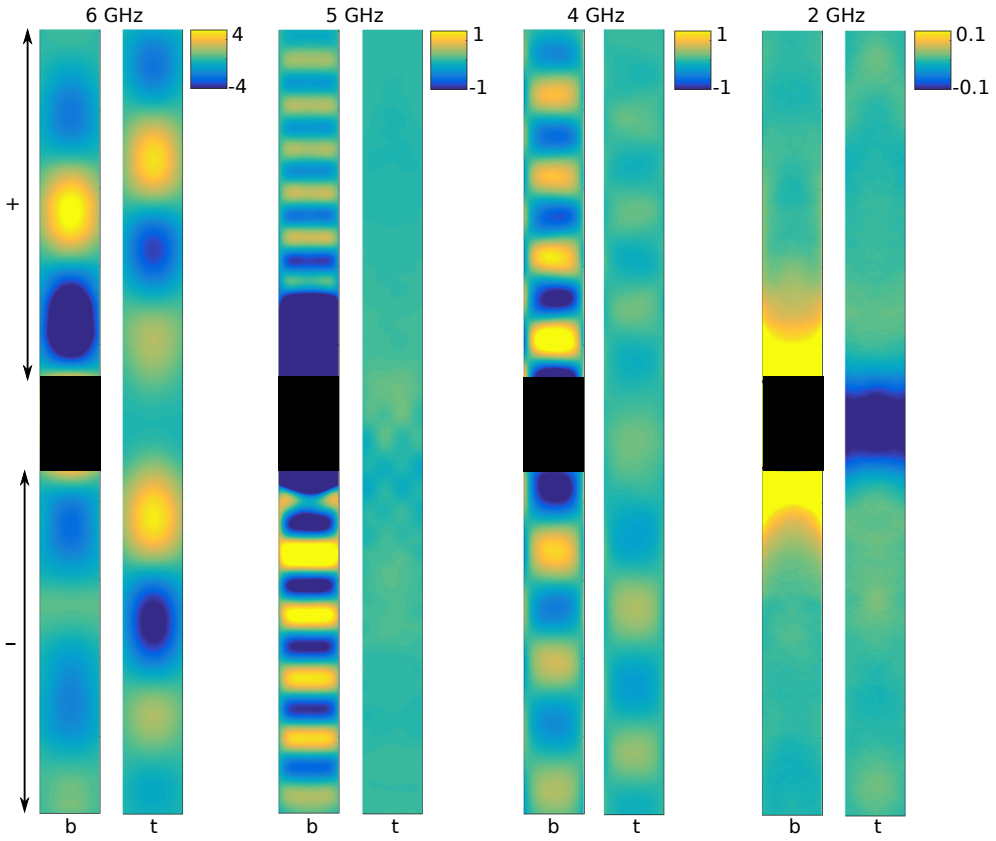

Figure 4.23: Spin waves excited locally at the black region ($w = 1$ μm) of the bottom facet (b). In addition the top facet (t) is shown for each frequency. The length of the NT is 10 μm with parameters according to sample s1. The simulation was conducted at zero external field. In the following the averaged wavelength are listed: $\lambda_{b,+}$, $\lambda_{b,-}$, $\lambda_{t,+}$ and $\lambda_{t,-}$, where + and - denotes the upper and lower parts of the corresponding facets, separated by the excitation regions.
6 GHz: $\lambda_{b,+} = 2.8$ μm, $\lambda_{b,-} = -$, $\lambda_{t,+} = 2.3$ μm, $\lambda_{t,-} = 2.5$ μm
5 GHz: $\lambda_{b,+} = -$, $\lambda_{b,-} = -$, $\lambda_{t,+} = 0.6$ μm, $\lambda_{t,-} = 0.8$ μm
4 GHz: $\lambda_{b,+} = 1.0$ μm, $\lambda_{b,-} = 1.5$ μm, $\lambda_{t,+} = 1.4$ μm, $\lambda_{t,-} = 2.0$ μm

Eshbach waves characteristically show a non homogeneous volume profile, causing different surface intensities on both sides of the excitation region, for sufficiently thick magnetic layers. In simulations, top and bottom layers are summed up over their thicknesses, thus nullifying the effect.

A more direct way to identify the asymmetric spin wave dispersion is a comparison of the wave lengths on both sides of the region of excitation. In the caption of Fig. 4.23 the wavelengths (λ) of the upper part and the lower part, named + and -, are evaluated at top (t) and bottom (b) facet. At 4 GHz the difference in wavelength is maximal with $\Delta\lambda_b = \lambda_{b,-} - \lambda_{b,+} = 0.5$ μm and $\Delta\lambda_t = \lambda_{t,-} - \lambda_{t,+} = 0.6$ μm. An asymmetry is found for all investigated frequencies if they enabled the creation of spin waves.

An interesting feature, originating from the local excitation at the bottom facet, is the difference in wavelength for top and bottom facet. At 4 GHz the effect is very pronounced and the difference on both facets is between $0.4 - 0.5$ μm. A similar

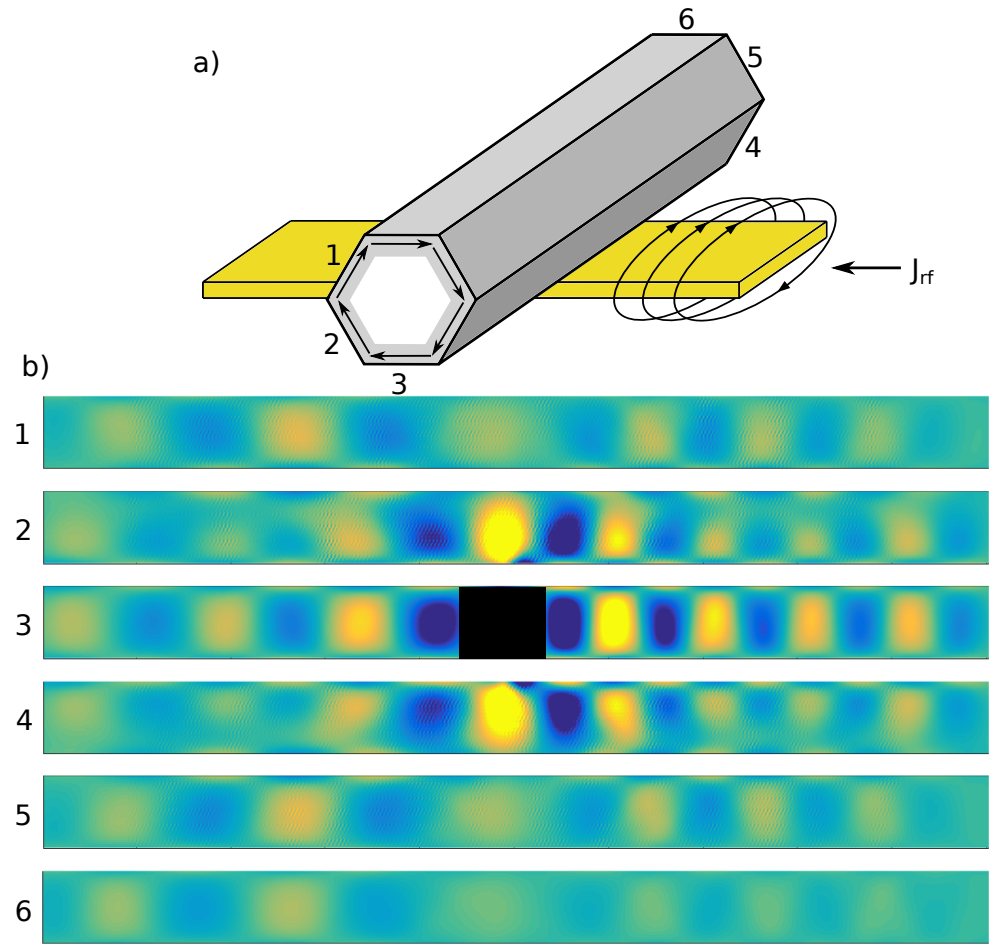

Figure 4.24: a) Schematic drawing of the simulated geometry. The excitation is only implemented on facet 3 (black area). The NT is in a vortex state and the simulation is conducted at $f = 4$ GHz and $\mathbf{H} = 0$ mT. b) Shows the facets introduced in a) unfolded. The simulation is equivalent to 4 GHz shown in Fig. 4.23.

behavior can be identified at 6 GHz. A precise description of this phenomenon is missing at the moment, but a possible reason might be identified considering the response at 5 GHz. As shown in Fig. 4.23, no spin waves are excited at the top facet. Analyzing the facets 1,2,4 and 5, as introduced in Fig. 4.24 a), the coupling of the spin waves to neighboring facets is largely hampered. While on facet 2 and 4, weaker spin waves are still excited (not shown) with comparable wavelength to $\lambda_{t,+} = 0.6$ and $\lambda_{t,-} = 0.8$, on facet 1 and 5 are no spin waves at all.

The behavior is different at 4 GHz. Fig. 4.24 b) shows all facet sides, named $1 - 6$. The bottom and top facets are now denoted 3 and 6, respectively. Although the excitation only occurs in the black area on facet 3, the spin waves are able to couple to all six facets. In this context the difference in wavelength might be attributed to an interaction between the 6 channels of traveling spin waves. Unfortunately only the mode structure at 6 GHz creates a sufficient intensity at the top facet to be detectable by the TRMOKE setup. In order to measure the modes appearing

at different frequencies with a surface sensitive technique, it would be necessary to create an excitation region on every facet, as it is indicated in chapter 2, Fig. 2.4. This, however, is very challenging to experimentally realize. Corresponding simulations show an identical spin wave pattern on every facet, determined by the dispersion relation of the system. (compare [8] and Eq. (2.5) for circular NTs).

4.4.2 First measurements with TRMOKE

The experiments presented in this section are conducted with TRMOKE in zero external field and the sample geometry introduced in Fig. 3.11 and schematically drawn in Fig. 4.24 a). The method only detects the top facet, furthest from the excitation antenna. Due to the limited resolution, experiments are only conducted on sample s1 (parameters are listed in table 4.1).

A frequency sweep from 2 to 10 GHz is performed. The most dominant spin wave patterns are shown in Fig. 4.25 a) at 6.24 GHz and b) at 6.32 GHz. Apart from these frequencies no spin wave patterns have been found in the frequency sweep. This finding is mainly explained because of the local excitation at the bottom facet. As discussed in the former subsection, this type of excitation can prevent spin waves from traveling at the bottom facet (compare Fig. 4.23). Unfortunately the top facet is the only one accessible by the laser beam. According to the simulations summarized in Fig. 4.23, only the mode pattern at 6 GHz shows a sufficiently large intensity on the top facet to be measured. Hence simulated and measured spin waves can be correlated.

The line scans shown in Fig. 4.25 are generated from the adjacent images. From these the wave length can be determined to be approximately 1.4 μm for both frequencies. It is thus likely that both spin waves originate from the same dispersion branch. Since the TRMOKE setup is capable of a minimal frequency step size of 80 MHz, no measurement between those frequencies could be conducted. It should be noted that the measured wavelength is smaller than the simulated values ($\Delta\lambda \approx 1$ μm). The possible cause of this discrepancy is an unresolved question at the moment this thesis is written.

The measured spin waves are only able to travel to one side of the antenna. Although from simulations an intensity difference is expected for both sides due to an asymmetric spin wave dispersion, the signal in Fig. 4.25 a) should not be completely within the noise floor of the experiment. The lack of signal is thus explained in terms of a multi-domain state. As the experiment is conducted at zero field, the NT is likely to exhibit a multi-domain state, especially because it experienced a magnetic field before the measurements presented in Fig. 4.25 were conducted. A domain wall, close to the upper edge of the antenna could prevent spin wave motion in this direction. This is due to a varied dispersion relation for the in-plane magnetized region of the domain wall. Hence, the spin waves impinging on the wall might get reflected instead of transmitted [66].

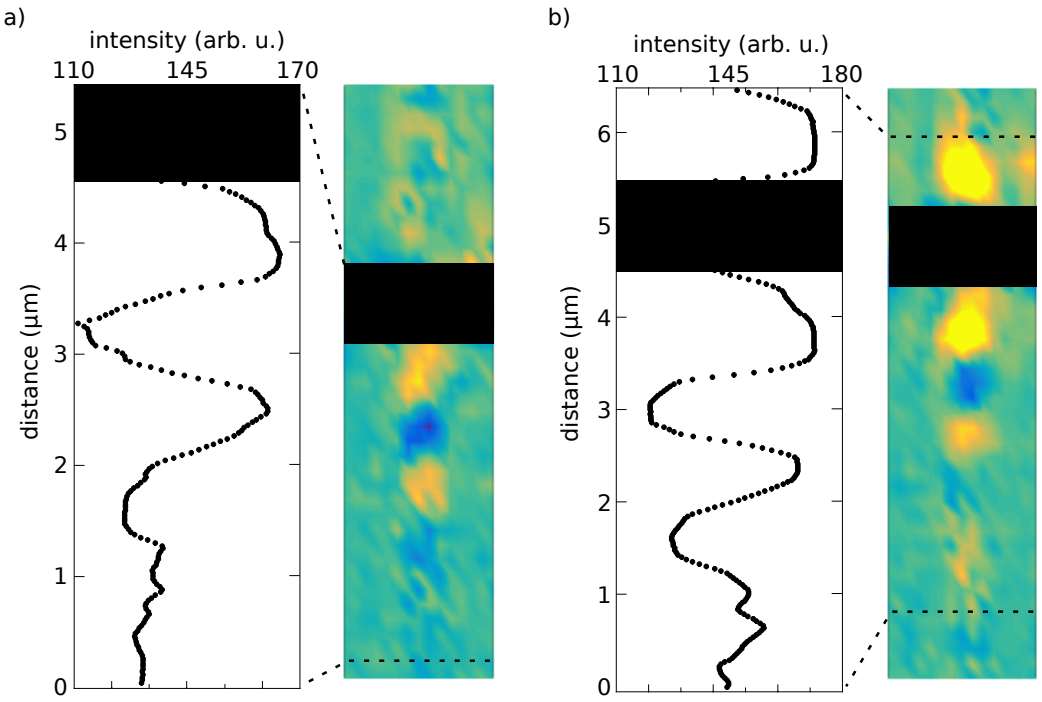

Figure 4.25: TRMOKE measurements conducted at a frequency of a) 6.24 GHz and b) 6.32 GHz. The spin waves are locally excited at the black region with a stripe antenna. The line scans are taken at the center of the image with a width of a few pixels. From this, the wave lengths are determined to be approximately 1.4 μm for a) and b).

Interestingly, high enough excitation fields can push the domain walls away from the antenna. This is experimentally proven during STXM measurements of a similar sample design [11]. In this experiment, application of rf excitation for some seconds, exceeding 4 dBm throughput resulted in the removal of all initially created domain walls. Lower powers can also move the domain walls, instead of pushing them to the end of the NT, where they annihilate. The domains could be removed for all tested frequencies between 2 and 8 GHz. The gold antenna in this experiment was 1 μm wide with a thickness of 250 nm.

The experiments presented in Fig. 4.25 are conducted at 0 dBm. A domain wall very close to the upper boundary of the black excitation region in Fig. 4.25 a) is assumed in the following. As mentioned previously, the changed dispersion relation within the domain wall can prevent spin waves from crossing it. Hence no spin waves are detected in this direction. In contrast in Fig. 4.25 b) one oscillation can be seen in the upper direction. Since the data in b) was acquired after the measurement shown in a) the domain wall could have moved upwards, allowing for one peak. In the lower direction the fast relaxation of the spin waves after only two full oscillations indicates a high damping. Simulations suggest a much larger travel distance if the rf excitation is located on every facet, wrapped around the circumference of the NT (compare the antenna geometry shown in Fig. 2.4).

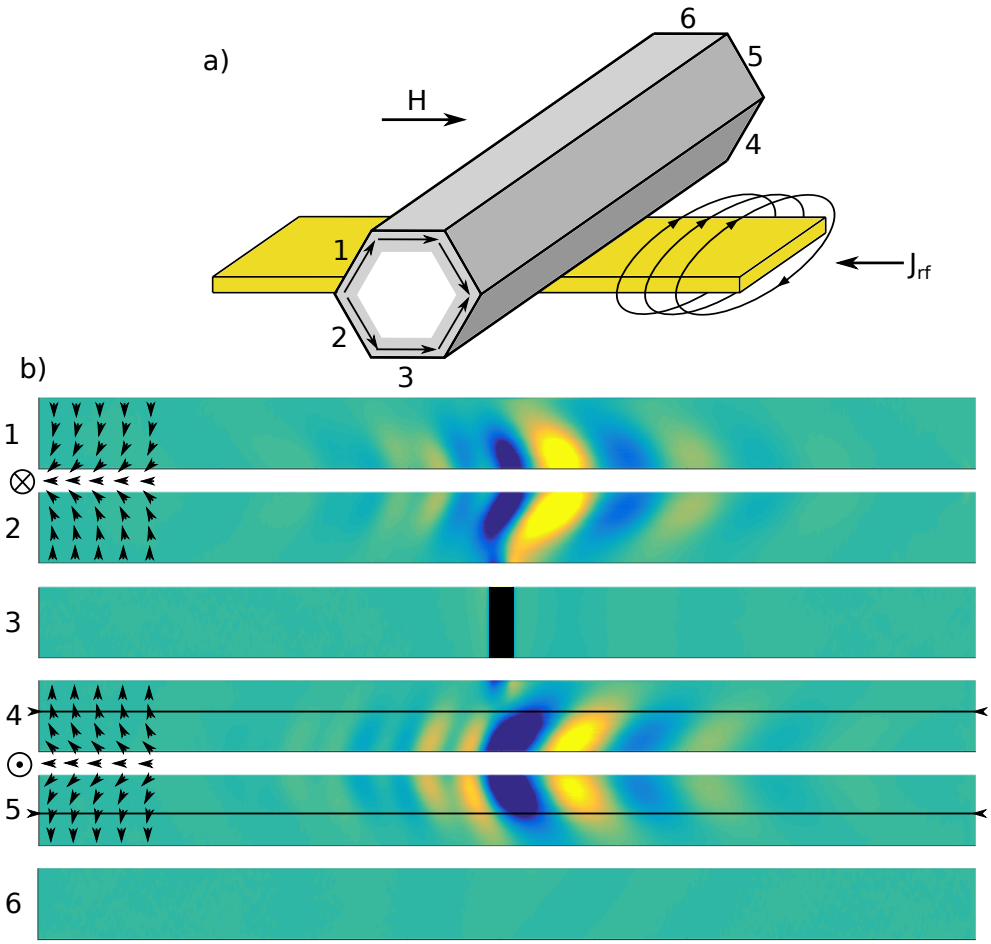

Figure 4.26: a) Schematic drawing of the simulated geometry. The excitation is only implemented on facet 3 (black area in b)). The NT is in an onion state and the simulation is conducted at $f = 4$ GHz and H = 120 mT. b) Shows the facets introduced in a) unfolded. The magnetization orientation is shown with black arrows.

4.4.3 Spin wave confinement in the onion state

In this subsection the possibility of sending spin waves along a domain wall within a NT is discussed. Similar effects in flat film structured samples have been reported for instance in [67] and [12]. The creation of domain walls is achieved by applying a magnetic field of H = 120 mT perpendicular to the tubes axis. The magnetic state is consequently the onion state with two domain walls between facet 1-2 and 4-5, as illustrated in Fig. 4.26.

From Fig. 4.2 in section 4.1.2 the domain wall width can be extracted for the given field value. The position at which the domain wall has less than 5% in-plane magnetization component (parallel to the tubes axis) is exemplarily marked as black lines in Fig. 4.26 for facets 4 and 5. The corresponding magnetization is shown as black arrows. At facets 1 and 2 the magnetization is additionally tilted slightly out-of-plane towards the GaAs core of the NT. At facets 4 and 5 it tends away from

the core, simply because of the way the external field is applied (compare Fig. 4.26 a)).

The simulation, conducted at 4 GHz, shows a clear confinement of the spin waves within the region of both domain walls. For higher excitation frequencies the confinement becomes less stringent and the spin waves are capable of partially entering facet 3 and 6. This behavior has been extensively studied in [12].

Considering the wavelengths of both directions (right and left) from the center excitation, $\lambda_{\text{right}} = 1.43\ \mu$m and $\lambda_{\text{left}} = 0.43\ \mu$m, the nonreciprocity occurring in the onion state is even more pronounced as for the vortex state.

For all simulations presented, the width of the region of excitation is as expected only relevant for the intensity of the spin waves, but not for their properties, such as their wavelength. Interestingly in Fig. 4.26, the excitation is rather far away from the domain walls and even lacks direct connection. Still the dynamical stray fields created locally are sufficient to excite the confined spin waves within the domain walls.

4.4.4 Dispersion relation

This section discusses the dispersion relation of hexagonally shaped NTs. The experiments shown are conducted using STXM and the sample geometry presented in subsection 3.6.1, Fig. 3.11 is applied. The simulated rf fields are only partially comparable to the excitation profiles created in the measurements using an antenna, which comprises out-of-plane (perpendicular to the NT) as well as in-plane (parallel to the NT) components. On the other hand the rf field used for simulations comprises only out-of-plane components.

Unfortunately the accessible spin wave patterns strongly depend on the way the NT is excited. This is illustrated in the following considering an antenna wrapped around the circumference of a NT, as shown in chapter 2, Fig. 2.4. The dependence becomes evident taking into account the dispersion relation shown in Fig. 4.28. While mode m_2 is a resonance of the top and bottom facet, m_3 appears only on the four oblique facets. These modes are separated in frequency due to different dynamical fields induced by different angles between the equilibrium magnetization and the rf field. Due to symmetry mode m_3 is not accessible, if the region of excitation is wrapped around the NT. Instead mode m_2 is now appearing on all 6 facets.

The dispersion relation shown in Fig. 4.28 was calculated using a rf field with $\text{sinc}(x) = \sin(x)/x$ profile both in space and time. The cut-off frequency and cut-off wave vector is set to 40 GHz and 2 μm^{-1} (half of the simulated tube length), respectively. Since the FFT of a $\text{sinc}(x)$ profile is a rectangle, all k-vectors are excited with the same intensity up to the cut-off wavelength. The rf field is applied perpendicular to the NTs axis and the x coordinate of the $\text{sinc}(x)$ profile is parallel to the NTs axis. Temporal snapshots of the magnetization with a resolution of 80

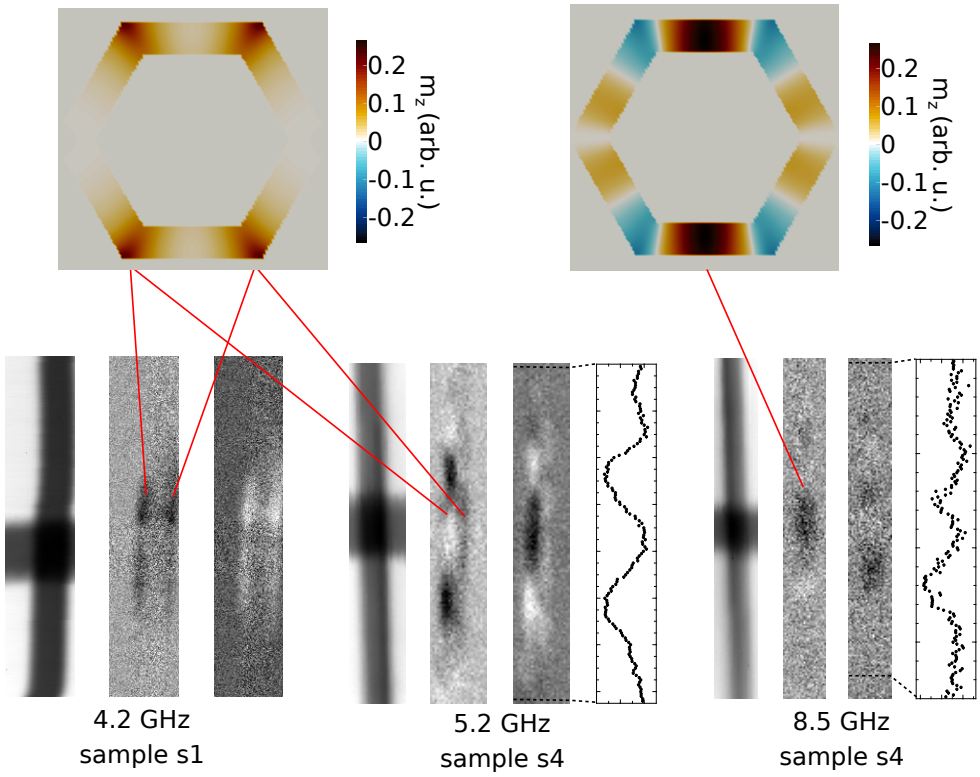

Figure 4.27: Exemplary wave patterns measured with STXM. The cross sections are simulated for sample parameters according to s4 (compare table 4.1). At $f = 4.25$ GHz (s1) and $f = 5.21$ GHz (s4) an edge mode is visible. At $f = 8.57$ GHz a mode at top and bottom facet appears. For all measurements a topographic image and two images with magnetic contrast at different phases are shown.

MHz are subsequently taken. These images are analyzed with a two dimensional Fourier Transformation. The frequency axis of the dispersion relation is obtained by FFT of each discretization node. The wave vector axis results from FFT along the length of the tube. The remaining spatial coordinates are summed up, ultimately resulting in the dispersion relation shown in Fig. 4.28. [2]

In order to obtain the simulated mode profiles shown in Fig. 4.27, the spatial sinc(x) profile is replaced by a homogeneous excitation (the time profile is not changed). This allows for extraction of only the modes with $k = 0$. The resulting edge mode m_1 and the FMR mode m_2 (compare Fig. 4.28) are shown in Fig. 4.27.

The measurements introduced in the following have been conducted with STXM either at the Swiss light source or at the Berlin Electron Storage Ring Society for Synchrotron Radiation II (BESSY II). Fig. 4.27 highlights three measurements. Sample s1 shows maximum magnetic response at the position of the antenna (width = 1 μm) at 4.2 GHz. The spin wave is unable to complete a full oscillation but clearly stays at the edges of the NT. The corresponding simulation is shown above and was conducted for sample parameters according to s4 and $k = 0$. Interestingly all four edges oscillate in-phase, resulting in an accumulation of the magnetic signal

[2] Calculation performed by Attila Kakáy.

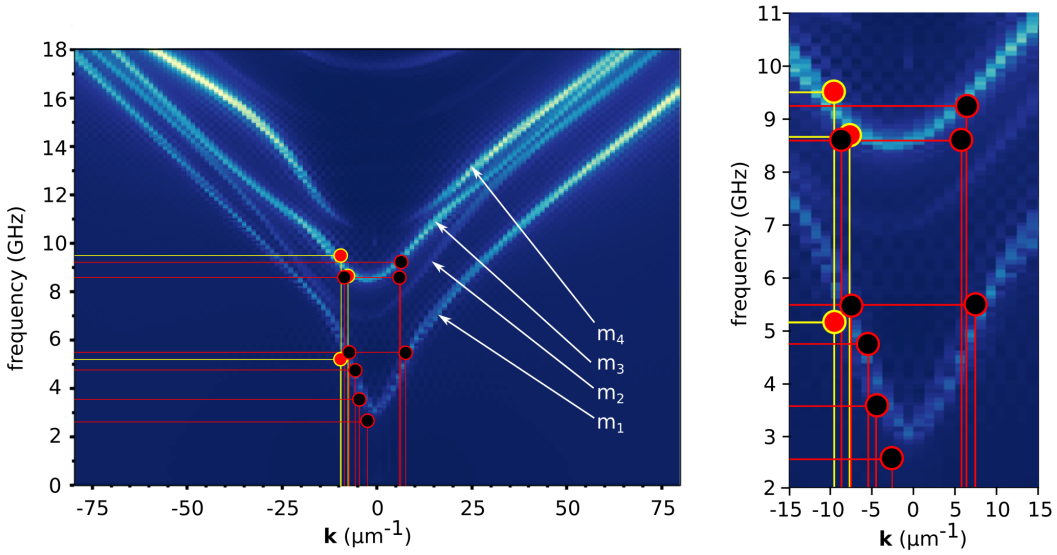

Figure 4.28: Simulated spin wave dispersion for sample parameters according to s4, except $\phi_{vv} = 210$ nm. The four most dominant modes are named m_i, $i = 1, 2, 3, 4$. Measured wavelengths are marked with red and black dots. Red dots are obtained from the determination of the wave length and black dots are obtained from the evaluation of the phase velocity. The right image shows the experimentally accessible region of the dispersion relation in detail.

utilizing the STXM technique (see section 3.6). On the other hand, if the oscillation of top and bottom facet is antisymmetric, the magnetic signal will annihilate.

For sample s4 (antenna width = 0.5 μm) the edge mode appears at 5.21 GHz and accomplishes one period in the $-\mathbf{k}$ direction. Hence, the wavelength can be determined from the line scan to be $\lambda_{\mathrm{m}_1} \approx 0.6$ μm. The associated point is marked in the dispersion relation and corresponds to the edge mode m_1. All k-vectors determined in this way are marked as red dots with yellow contour in Fig. 4.28.

Note that STXM can not be used to determine the chirality of the VS. Hence the assignment of the directions -$\mathbf{k}$ and $+\mathbf{k}$ to the measured points in Fig. 4.28 is arbitrary. However, since the measurements were conducted at zero field the ground state stayed unchanged. Hence the points marked in Fig. 4.28 are either correctly positioned or they have to be mirrored on a vertical axis at $k = 0$.

As the frequency is further increased, a mode pattern appears in sample s4 at 8.57 GHz. With the formerly described method, its wavelength can only be determined in the -$\mathbf{k}$ direction, yielding $\lambda_{\mathrm{m}_3}^{8.5\mathrm{GHz}} \approx 0.85$ μm. That is because in the $+\mathbf{k}$ direction the spin wave does no complete a full period. Utilizing the dispersion relation the spin wave can be related to mode m_3. The corresponding simulation displayed in Fig. 4.27 shows resonance at the top and bottom facet. Because both facets oscillate in phase, the signal of both adds up. Since the magnetic ground state is a vortex state, this mode is the first Damon Eshbach like spin wave ($\mathbf{M} \perp \mathbf{k}$) measured using STXM in the scope of this thesis.

The spin wave occurring at highest frequency is detected at 9.5 GHz with a wavelength of $\lambda_{\mathrm{m}_3}^{9.5\mathrm{GHz}} \approx 0.75\ \mu$m. Marking its position in the dispersion relation it can be again associated to the mode m_3. Unfortunately no spin wave patterns with evaluable wavelengths have been simultaneously found for the $-\mathbf{k}$ and the $+\mathbf{k}$ direction. Thus in the following the phase velocity defined as $v_\mathrm{p} = \omega/k$ is used to obtain the associated k-vectors of the spin waves. With the STXM setup we usually detect one frequency period with 7 parallel channels. Hence we have access to the time necessary to complete a single period at the applied frequency f: $t = 1/(fN_\mathrm{f})$, where $N_\mathrm{f} = 7$ is the number of frames taken during one period. Measuring the distance s that valleys or peaks move during different frames thus enables to calculate v_p, yielding

$$k = \frac{2\pi}{s \cdot N_\mathrm{f}}. \tag{4.7}$$

This analysis allows the measurement of k, even though a complete cycle has not been accomplished by the spin waves. This way additional measurement points can be added to the dispersion relation marked with black dots and red contour. For the edge mode m_1 at f=5.5 GHz the dispersion relation is symmetric within the error and k is determined to be approximately 7 $\mu\mathrm{m}^{-1}$ for negative and positive direction. The most interesting results are found at a frequency of 8.57 GHz, where the spin waves travel a distance of $s = 0.18 \pm 0.02\ \mu$m and $s = 0.12 \pm 0.02\ \mu$m, per frame ($N_\mathrm{f} = 6$), in the negative and positive k direction, respectively. Using Eq. (4.7) this yields $k_+ = 5.8 \pm 0.7\ \mu\mathrm{m}^{-1}$ and $k_- = 8.7 \pm 1.4\ \mu\mathrm{m}^{-1}$. This measurement is the first direct proof of the nonreciprocity of spin waves in magnetic NTs. This asymmetry of the dispersion relation is introduced into the system solely due to the curvature of the NT (compare section 2.3.3).

Unfortunately mode m_4 could not be measured, since the necessary high frequencies could not be reached with reasonable power throughput due to the antenna used in the measurements. The higher the frequency, the more power gets reflected at the constriction of the antenna because of the resistance mismatch. Additionally high frequency spin waves require antennas with very small width in order to be excited. Hence, the antennas become vulnerable to damage caused by high power throughput. Mode m_4 would be especially interesting because it vanishes approaching $k = 0$. Thus it shows no homogeneous pattern but only traveling spin waves exhibiting $k \neq 0$. Furthermore its dispersion asymmetry is very pronounced, which makes this mode even more interesting for the investigation of the nonreciprocity.

It should be mentioned that backward volume like modes have been observed for sample s4 below 4.5 GHz. These modes circulated the circumference of the NT and were found close to the antenna. At 4.2 GHz they maximally extended 1 μm away from the antenna in both directions. These modes are likely connected to non-linear effects, induced because of very high excitation intensities. The simulated dispersion

relation is only valid for spin waves with wave vectors parallel to the tubes axis and thus completely ignores backward volume geometries.

5 Conclusion and Outlook

The aim of this thesis was a detailed analysis of the static and dynamic properties of hexagonally shaped magnetic nanotubes consisting of permalloy. The material was initially chosen because of its typical lack of magnetic in-plane anisotropies in full film samples. Consequently the magnetic ground state was expected to be dependent solely on the geometry. The ratio between diameter and length (ϕ_{vv}/L) thus would determine the ground state, as it was shown by simulations. However, AMR experiments revealed a vortex state to be present at zero field, irrespective of the tubes length or diameter. This finding indicates a strong anisotropy perpendicular to the NTs long axis with a different origin than only the reduction of stray fields.

The direct growth of Py on top of the GaAs resulted in a pronounced crystalline order adopted from the underlying semiconductor. This was directly observed by TEM measurements. A 1 nm thick Al_2O_3 buffer layer was subsequently grown between metal and semiconductor in order to hamper crystalline growth. This led to a reduction of the saturation field, necessary to saturate the material parallel to the tubes axis, by a factor of 1.5. Since a Py full film grown on a (110) GaAs plane (equivalent to the facets of the NT) only exhibits very little anisotropy (≈ 3 kJ/m^3), the large anisotropy encountered in NTs (≈ 21 kJ/m^3) was thus explained in terms of a self-shadowing effect occurring during growth. A prerequisite for its occurrence is a small angle between NT axis and Py evaporation beam direction, which is $\zeta = 28°$ for our MBE chamber. During the process of growth elongated crystalline chains with a tendency to elongate perpendicular to the atom beam direction are formed. Consequently these chains favor the vortex state in NTs. Finally the gaps in between the chains are filled as well, creating a very smooth surface with a root mean squared roughness of approximately 0.4 nm.

Knowledge of the origin of the growth-induced anisotropy offers the possibility of tuning the magnetic ground state. For instance, elevated temperatures during growth may increase the metal atom mobility on the facets, preventing crystalline chains. Consequently the magnetic ground state becomes solely geometry dependent. This however turned out to be problematic for GaAs-based NTs because of decomposition of the material at high temperatures. Also a varying evaporation angle ζ can change the anisotropy. In the limit of $\zeta = 90°$ it behaves as a full film.

A downside of an AMR measurement is its averaging nature. In order to obtain spatial magnetic resolution across the NTs long axis STXM was employed. The measurements revealed an additional ground state configuration: Multiple vortex domains with alternating handedness. Given the small domain wall width ($\Delta_{DW} \approx 70$ nm), multiple domains did not influence the AMR measurements sufficient

enough to be previously identified. After growth the NTs usually exhibit a single global vortex state. Exposure to an external magnetic field caused the single vortex state to decay into a multi-domain state at zero field. This finding may enable a broad range of future experiments concerning domain wall motion in magnetic NTs, as these are expected to reach higher speeds than in flat stripes [9,42]. By using very small antennas, localized rf fields could be exploited to delete the formerly created domains [11]. Since magnetic storage media rely on reading and writing processes this finding may be of particular interest for applications.

The second part of this thesis concentrated on dynamical properties of Py NTs. PMR based FMR was utilized to measure averaged absorption peaks up to 2 T. A variety of different mode patterns was found, depending strongly on the sense of rotation of the NT around its long axis with respect to the external field orientation. Besides in-plane and out-of-plane FMR resonances also complex mode patterns at intermediate fields were found. The exact cross sectional mode structure was subsequently visualized using micromagnetic simulations. Depending on the field strength and orientation, only localized modes solely living at edges or facets could be found. These potentially offer different channels for information transport.

Since both PMR and AMR are averaging techniques, TRMOKE was used to gain local spatial information. As the technique depends on the reflection of laser light it could only detect few of the formerly found modes, such as the in-plane FMR mode and higher order patterns on the top facet. At zero external field the multiple domain state could again be observed by many localized resonances with different relative phases.

Finally spin waves in hexagonally shaped NTs are investigated. For the experiment it was convenient to place the NT on top of a stripe antenna. This however leads to an rf excitation that is mostly concentrated on the facet in touch with the antenna. Simulations conducted with local regions of excitation at the bottom facet showed significant differences to homogeneous excitations. Only some of the spin waves created at the bottom facet are able to couple to the opposite facet and are hence detectable by optical methods. In addition the first spin waves in magnetic NTs were successfully detected by TRMOKE with a wavelength of 1.4 μm at a frequency of 6.24 - 6.32 GHz.

Spin waves were also investigated with STXM. As the simulated dispersion relation indicates, only a few modes are located on the top facet. Hence in this regard STXM is of advantage compared to TRMOKE, since the X-rays transmit the sample and are not limited to reflection of light from the top facet. This way edge modes could be observed for a broad range of frequencies, as well as Damon Eshbach like modes above 8 GHz. All spin wave patterns are related to the simulated dispersion relation with reasonable accuracy. While the measured edge modes show, similar to the simulations, almost no asymmetric dispersion, the nonreciprocity could be proven for the first time with DE like spin waves detected at 8.57 GHz. The k-vectors of both propagation directions were $k_+ = 5.8 \pm 0.7\ \mu\text{m}^{-1}$ and $k_- = 8.7 \pm 1.4\ \mu\text{m}^{-1}$. In

magnetic NTs the nonreciprocity is a purely curvature induced effect. A downside of the experiments was the surprisingly high damping found in the investigated NTs. It causes the spin waves to decay quickly. Sometimes spin waves are unable to accomplish a full oscillation.

In summary, the complex geometry of a hexagonal magnetic NT exhibits a tremendous amount of differences compared to flat structures, as they are currently present in most modern magnetic storage devices. Flux closed structures in combination with existing flat film technology might be interesting for future logic and memory devices. They can offer additional degrees of freedom for spin wave channels and can exhibit magnetic ground states at zero field that are otherwise hard to accomplish. For instance, the Damon Eshbach geometry, in which spin waves exhibit the highest group velocity [39], is given by default in all investigated NTs.

Bibliography

[1] S. S. P. Parkin and S.-H. Yang. Memory on the racetrack. *Nat. Nanotechnol.*, 10(3):195–198, March 2015.

[2] V. V. Zhirnov, R. K. Cavin, J. A. Hutchby, and G. I. Bourianoff. Limits to binary logic switch scaling - a gedanken model. *Proc. IEEE*, 91(11):1934–1939, November 2003.

[3] J. M. Owens, J. H. Collins, and R. L. Carter. System applications of magnetostatic wave devices. *Circuits, Systems, and Signal Processing*, 4(1-2):317–334, March 1985.

[4] S. S. P. Parkin, M. Hayashi, and L. Thomas. Magnetic Domain-Wall Racetrack Memory. *Science*, 320(5873):190–194, April 2008.

[5] M. Hayashi, L. Thomas, R. Moriya, C. Rettner, and S. S. P. Parkin. Current-Controlled Magnetic Domain-Wall Nanowire Shift Register. *Science*, 320(5873):209–211, April 2008.

[6] M. Haidar and M. Bailleul. Thickness dependence of degree of spin polarization of electrical current in permalloy thin films. *Phys. Rev. B*, 88(5):054417, August 2013.

[7] T. A. Moore, M. Kläui, L. Heyne, P. Möhrke, D. Backes, J. Rhensius, U. Rüdiger, L. J. Heyderman, T. O. Mentes, M. Á. Niño, A. Locatelli, A. Potenza, H. Marchetto, S. Cavill, and S. S. Dhesi. Domain wall velocity measurement in permalloy nanowires with X-ray magnetic circular dichroism imaging and single shot Kerr microscopy. *J. Magn. Magn. Mater.*, 322(9):1347 – 1352, May 2010.

[8] J. A. Otálora, M. Yan, H. Schultheiss, R. Hertel, and A. Kákay. Curvature-Induced Asymmetric Spin-Wave Dispersion. *Phys. Rev. Lett.*, 117(22):227203, November 2016.

[9] M. Yan, C. Andreas, A. Kákay, F. Garcia Sanchez, and R. Hertel. Fast domain wall dynamics in magnetic nanotubes: Suppression of Walker breakdown and Cherenkov-like spin wave emission. *Appl. Phys. Lett.*, 99(12):122505, September 2011.

[10] P. Landeros, O. J. Suarez, A. Cuchillo, and P. Vargas. Equilibrium states and vortex domain wall nucleation in ferromagnetic nanotubes. *Phys. Rev. B*, 79(2):024404, January 2009.

[11] M. Zimmermann, T. N. G. Meier, F. Dirnberger, A. Kákay, M. Decker, S. Wintz, S. Finizio, E. Josten, J. Raabe, M. Kronseder, D. Bougeard, J. Lindner, and C. H. Back. Origin and manipulation of stable vortex ground states in permalloy nanotubes. *Nano Lett.*, 18(5):2828–2834, April 2018.

[12] K. Wagner, A. Kákay, K. Schultheiss, A. Henschke, T. Sebastian, and H. Schultheiss. Magnetic domain walls as reconfigurable spin-wave nanochannels. *Nat. Nanotechnol.*, 11(5):432–436, February 2016.

[13] J. Bachmann, M. Knez, S. Barth, H. Shen, S. Mathur, U. Gösele, and K. Nielsch. Ordered Iron Oxide Nanotube Arrays of Controlled Geometry and Tunable Magnetism by Atomic Layer Deposition. *J. Am. Chem. Soc.*, 129(31):9554–9555, July 2007.

[14] O. Albrecht, R. Zierold, S. Allende, J. Escrig, C. Patzig, B. Rauschenbach, K. Nielsch, and D. Görlitz. Experimental evidence for an angular dependent transition of magnetization reversal modes in magnetic nanotubes. *J. Appl. Phys.*, 109(9):093910, May 2011.

[15] A. Rudolph, M. Soda, M. Kiessling, T. Wojtowicz, D. Schuh, W. Wegscheider, J. Zweck, C. H. Back, and E. Reiger. Ferromagnetic GaAs/GaMnAs Core Shell Nanowires Grown by Molecular Beam Epitaxy. *Nano Lett.*, 9(11):3860–3866, September 2009.

[16] B. Gross, D. P. Weber, D. Rüffer, A. Buchter, F. Heimbach, A. Fontcuberta i Morral, D. Grundler, and M. Poggio. Dynamic cantilever magnetometry of individual CoFeB nanotubes. *Phys. Rev. B*, 93(6):064409, February 2016.

[17] A. Buchter, R. Wölbing, M. Wyss, O. F. Kieler, T. Weimann, J. Kohlmann, A. B. Zorin, D. Rüffer, F. Matteini, G. Tütüncüoglu, F. Heimbach, A. Kleibert, A. Fontcuberta i Morral, D. Grundler, R. Kleiner, D. Koelle, and M. Poggio. Magnetization reversal of an individual exchange-biased permalloy nanotube. *Phys. Rev. B*, 92(21):214432, December 2015.

[18] M. Wyss, A. Mehlin, B. Gross, A. Buchter, A. Farhan, M. Buzzi, A. Kleibert, G. Tütüncüoglu, F. Heimbach, A. Fontcuberta i Morral, D. Grundler, and M. Poggio. Imaging magnetic vortex configurations in ferromagnetic nanotubes. *Phys. Rev. B*, 96(2):024423, July 2017.

[19] K. Baumgaertl, F. Heimbach, S. Maendl, D. Rueffer, A. Fontcuberta I Morral, and D. Grundler. Magnetization reversal in individual Py and CoFeB nanotubes locally probed via anisotropic magnetoresistance and anomalous Nernst effect. *Appl. Phys. Lett.*, 108(13):132408, March 2016.

[20] X. Xing, S. Li, X. Huang, and Z. Wang. Engineering spin-wave channels in submicrometer magnonic waveguides. *AIP Adv.*, 3(3):032144, March 2013.

[21] C. L. Dennis, R. P. Borges, L. D. Buda, U. Eberls, J. F. Gregg, M. Hehn, E. Jouguelet, K. Ounadjela, I. Petej, I. L. Prejbeanu, and M. J. Thornton. The defining length scales of mesomagnetism: a review. *J. Phys.: Condens. Matter*, 14(49):1175 – 1262, November 2002.

[22] B. Heinrich and J.F. Cochran. Ultrathin metallic magnetic films: magnetic anisotropies and exchange interactions. *Adv. Phys.*, 42(5):523–639, July 1993.

[23] R. Fitzpatrick. *Classical Electromagnetism*. CreateSpace Independent Publishing Platform, 2016.

[24] A. Aharoni. *Introduction to the Theory of Ferromagnetism*. Oxford University Press, 2001.

[25] T. N. G. Meier. Thermodynamical properties of fluctuating magnetic stripe domains in ultrathin Fe/Ni/Cu(001) and Ni/Fe/Cu(001) films. Master's thesis, University of Regensburg, 2014.

[26] R. Schäfer A. Hubert. *Magnetic Domains*. Springer Berlin Heidelberg, 1998.

[27] B. Heinrich, J. F. Cochran, A. S. Arrott, S. T. Purcell, K. B. Urquhart, J. R. Dutcher, and W. F. Egelhoff Jr. Development of Magnetic Anisotropies in Ultrathin Epitaxial Films of Fe(001) and Ni(001). *Appl. Phys. A*, 49(5):473–490, November 1989.

[28] D. S. Chuang, C. A. Ballentine, and R. C. O'Handley. Surface and step magnetic anisotropy. *Phys. Rev. B*, 49(21):15084–15095, June 1994.

[29] L. Landau and E. Lifshitz. On the theory of the dispersion of magnetic permeability in ferromagnetic bodies. *Phys. Zeitsch. der Sow.*, 8:153–169, 1935.

[30] T. L. Gilbert. A Lagrangian formulation of the gyromagnetic equation of the magnetization field. *Phys. Rev.*, 100:1243, 1955. [abstract only].

[31] M. M. Decker. *Spin Current Induced Control of Magnetization Dynamics*. PhD thesis, Universität Regensburg, 2017.

[32] Z. Clinski, K.B. Urquhart, and B. Heinrich. Using ferromagnetic resonance to measure the magnetic moments of ultrathin films. *J. Magn. Magn. Mater.*, 166(1-2):6–26, February 1997.

[33] M. O. Härtinger. Magnetische Eigenschaften neuer ferromagnetischer Materialien. Master's thesis, Universität Regensburg, 2011.

[34] C. Kittel. On the Theory of Ferromagnetic Resonance Absorption. *Phys. Rev.*, 73(2):155–161, January 1948.

[35] G. Woltersdorf. *Spin-pumping and two magnon scattering in magnetic multilayers*. PhD thesis, Simon Fraser University, 2004.

[36] K. Vogt, F. Y. Fradin, J. E. Pearson, T. Sebastian, S. D. Bader, B. Hillebrands, A. Hoffmann, and H. Schultheiss. Realization of a spin-wave multiplexer. *Nat. Commun.*, 5:3727–, April 2014.

[37] B. A. Kalinikos and A. N. Slavin. Theory of dipole-exchange spin wave spectrum for ferromagnetic films with mixed exchange boundary conditions. *J. Phys. C: Solid State Phys.*, 19(35):7013–7033, December 1986.

[38] J. Stigloher, M. Decker, H. S. Körner, K. Tanabe, T. Moriyama, T. Taniguchi, H. Hata, M. Madami, G. Gubbiotti, K. Kobayashi, T. Ono, and C. H. Back. Snell's Law for Spin Waves. *Phys. Rev. Lett.*, 117(3):037204, July 2016.

[39] C. Bayer, J. Jorzick, S. O. Demokritov, A. N. Slavin, K. Y. Guslienko, D. Berkov, N. L. Gorn, M. P. Kostylev, and B. Hillebrands. *Spin Dynamics in Confined Magnetic Structures III*. Springer Berlin Heidelberg, 2006.

[40] N. Kazantseva, R. Wieser, and U. Nowak. Transition to Linear Domain Walls in Nanoconstrictions. *Phys. Rev. Lett.*, 94(3):037206, January 2005.

[41] T. Luc and S. S. P. Parkin. *Current Induced Domain-wall Motion in Magnetic Nanowires*. Handbook of Magnetism and Advanced Magnetic Materials, 2007.

[42] M. Yan, C. Andreas, A. Kákay, F. Garcia Sanchez, and R. Hertel. Chiral symmetry breaking and pair-creation mediated Walker breakdown in magnetic nanotubes. *Appl. Phys. Lett.*, 100(25):252401, June 2012.

[43] I. A. Campbell, A. Fert, and O. Jaoul. The spontaneous resistivity anisotropy in Ni-based alloys. *J. Phys. C: Solid State Phys.*, 3(1S):95–101, May 1970.

[44] N. F. Mott. The resistance and thermoelectric properties of the transition metals. *Proc. Royal Soc. A*, 156(888):368–382, August 1936.

[45] T. McGuire and R. Potter. Anisotropic magnetoresistance in ferromagnetic 3d alloys. *IEEE Trans. Magn.*, 11(4):1018–1038, July 1975.

[46] R. I. Potter. Magnetoresistance anisotropy in ferromagnetic NiCu alloys. *Phys. Rev. B*, 10(11):4626–4636, December 1974.

[47] A. Vansteenkiste, J. Leliaert, M. Dvornik, M. Helsen, F. Garcia-Sanchez, and B. Van Waeyenberge. The design and verification of MuMax3. *AIP Adv.*, 4(10):107133, June 2014.

[48] J. Hubmann. *GaAs nanowires: Epitaxy, crystal structure-related properties and magnetic heterostructures*. PhD thesis, Universität Regensburg, 2015.

[49] R. S. Wagner and W. C. Ellis. Vapor-liquid-solid mechanism of single crystal growth. *Appl. Phys. Lett.*, 4(5):89–90, April 1964.

[50] V. G. Dubrovskii, N. V. Sibirev, J. C. Harmand, and F. Glas. Growth kinetics and crystal structure of semiconductor nanowires. *Phys. Rev. B*, 78(23):235301, December 2008.

[51] P. Krogstrup, H. I. Jørgensen, E. Johnson, M. H. Madsen, C. B. Sørensen, A. Fontcuberta i Morral, M. Aagesen, J. Nygård, and F. Glas. Advances in the theory of III–V nanowire growth dynamics. *J. Phys. D: Appl. Phys.*, 46(31):313001, July 2013.

[52] S. Furthmeier, F. Dirnberger, J. Hubmann, B. Bauer, T. Korn, C. Schüller, J. Zweck, E. Reiger, and D. Bougeard. Long exciton lifetimes in stacking-fault-free wurtzite GaAs nanowires. *Appl. Phys. Lett.*, 105(22):222109, December 2014.

[53] J. M. D. Coey. *Magnetism and Magnetic Materials*. Cambridge: Cambridge University Press, 2010.

[54] M. Móller, K. Lenz, and J. Lindner. Frequency-Domain magnetic resonance - alternative detection schemes for samples at the nanoscale. *J. Surf. Interfac. Mater.*, 2(1):46–68, March 2014.

[55] J. Raabe, G. Tzvetkov, U. Flechsig, M. Böge, A. Jaggi, B. Sarafimov, M. G. C. Vernooij, T. Huthwelker, H. Ade, D. Kilcoyne, T. Tyliszczak, R. H. Fink, and C. Quitmann. PolLux: A new facility for soft x-ray spectromicroscopy at the Swiss Light Source. *Rev. Sci. Instrum.*, 79(11):113704, October 2008.

[56] M. Obstbaum. *Inverse spin Hall effect in metallic heterostructures*. PhD thesis, Universität Regensburg, 2015.

[57] Y. Zhao, Q. Song, S.-H. Yang, T. Su, W. Yuan, S. S. P. Parkin, J. Shi, and W. Han. Experimental Investigation of Temperature-Dependent Gilbert Damping in Permalloy Thin Films. *Sci. Rep.*, 6:22890, March 2016.

[58] J. A. Osborn. Demagnetizing Factors of the General Ellipsoid. *Phys. Rev.*, 67(11):351–357, June 1945.

[59] M. F. Millea and D. F. Kyser. Thermal Decomposition of Gallium Arsenide. *J. Appl. Phys.*, 36(1):308–313, January 1965.

[60] V. Kamberský, Z. Málek, Z. Frait, and M. Ondris. The dependence of the uniaxial magnetic anisotropy in evaporated films on the angle of incidence. *Czech. J. Phys. B*, 11(3):171–178, March 1961.

[61] M. S. Cohen. Anisotropy in Permalloy Films Evaporated at Grazing Incidence. *J. Appl. Phys.*, 32(3):87–88, March 1961.

[62] D. O. Smith, M. S. Cohen, and G. P. Weiss. Oblique-Incidence Anisotropy in Evaporated Permalloy Films. *J. Appl. Phys.*, 31(10):1755–1762, November 1960.

[63] T. G. Knorr and R. W. Hoffman. Dependence of Geometric Magnetic Anisotropy in Thin Iron Films. *Phys. Rev.*, 113(4):1039–1046, February 1959.

[64] T. G. S. M. Rijks, R. Coehoorn, M. J. M. de Jong, and W. J. M. de Jonge. Semiclassical calculations of the anisotropic magnetoresistance of NiFe-based thin films, wires, and multilayers. *Phys. Rev. B*, 51(1):283–291, January 1995.

[65] C. Tannous and J. Gieraltowski. The Stoner–Wohlfarth model of ferromagnetism. *Eur. J. Phys.*, 29(3):475–487, March 2008.

[66] S. Macke and D. Goll. Transmission and reflection of spin waves in the presence of Néel walls. *J. Phys. Conf. Ser.*, 200(4):042015, January 2010.

[67] F. Garcia-Sanchez, P. Borys, R. Soucaille, J.-P. Adam, R. L. Stamps, and J.-V. Kim. Narrow Magnonic Waveguides Based on Domain Walls. *Phys. Rev. Lett.*, 114(24):247206, June 2015.

List of Acronyms

AFM	atomic force microscopy
ALD	atomic layer deposition
AMR	anisotropic magnetoresistance
BESSY	Berlin Electron Storage Ring Society for Synchrotron Radiation
BV	backward volume
CPW	coplanar wave guide
DE	Damon Eshbach
FD	finite difference
FE	finite element
FFT	fast Fourier transform
FIB	focused ion beam
FMR	ferromagnetic resonance
GHz	gigahertz
GIS	gas injection system
HWHM	half width at half maximum
LLD	light emitting diode
LLG	Landau-Lifshitz-Gilbert
MBE	molecular beam epitaxy
NR	nanorod
NT	nanotube
OS	onion state
PBC	periodic boundary conditions
PMR	planar microresonator
Py	permalloy
RHEED	reflection high-energy electron diffraction
rf	radio frequency
SEM	scanning electron microscope
STXM	scanning transmission X-ray microscopy
SLS	Swiss Light Source
TEM	transmission electron microscope
TRMOKE	time resolved magneto optical Kerr effect
UHV	ultra-high vacuum
US	uniform state
VLS	vapor-liquid-solid
VS	vortex state
WZ	wurtzite
XMCD	X-ray circular dichroism
ZB	zinc-blende

List of Constants and Symbols

π	3.1415...	circle constant
e	$1.6 \cdot 10^{-19}$ C	electron charge
m_e	$9.11 \cdot 10^{-31}$ kg	electron mass
$\hbar$	$6.63 \cdot 10^{-34}$ m^2kg/s	Planck's constant
μ_0	$4\pi \cdot 10^{-7}$ N/A^2	vacuum permeability
A_{ex}	$1.3 \cdot 10^{-11}$ J/m	exchange stiffness of permalloy
$\mu_0 M_S$	1 T	saturation magnetization of permalloy
γ	$1.85 \cdot 10^{11}$ $T^{-1}s^{-1}$	gyromagnetic ratio of permalloy
g	2.00	electron spin g-factor
$\hat{n}$	unit vector	
μ_r	relative permeability	
ω	angular frequency	
ΔH(0)	zero frequency linewidth offset	
f	frequency	
h_{rf}	radio-frequency excitation field	
w	stripe width	
$q(x,t)$	spin wave mode profile	
ρ_V	dynamical volume charge density	
σ_S	dynamical surface charge density	
$V^{sd}_{k,k'}$	matrix element for s-d transitions	
τ	mean relaxation time	
ρ	resistivity	
R,r	radius	
R_n	Fourier amplitude	
Z_n	Fourier amplitude	
n	order of spin waves	
J	current vector	
H	magnetic field vector	
M	magnetization vector	
$\mathcal{H}$	Hamiltonian	
ϵ	energy density	
J_{ij}	exchange integral	
Θ	angle (multiple definitions)	
φ	angle (multiple definitions)	
S	spin vector	
m	normalized magnetization vector	
A	exchange stiffness	
l_{ex}	exchange length	

M_S	saturation magnetization
ϕ	magnetic scalar potential
$\mathbf{B}$	magnetic induction vector
K_6	six-fold anisotropy constant
$K^{\parallel}$	in-plane anisotropy constant
$K^{\perp}$	out-of-plane anisotropy constant
K_4	four-fold anisotropy constant
K_2, $K_U^{\parallel}$	uniaxial in-plane anisotropy constant
$K_U^{\perp}$	uniaxial out-of-plane anisotropy constant
γ	gyromagnetic ratio
$\mathbf{E}$	electrical field vector
α	empirical Gilbert damping constant
δ	skin depth
χ	magnetic susceptibility
M_{eff}	effective magnetization
H_{FMR}	ferromagnetic resonance field
ΔH	half width at half maximum linewidth
R_{rms}	root mean squared roughness
Q	quality factor
F	filling factor
U	voltage
P	power
α_0	detector parameter (Schottky diode)
C1, C2	capacitances
I	intensity
ε	FMR mixing angle
$\mathscr{B}$	effective magnetic induction
$\mathscr{H}$	effective magnetic field
λ	wave length
k	wave vector
t, d	film thickness
ε_{SW}	excitation efficiency
l	domain wall parameter
Δ_{DW}	domain wall width
K_{eff}	effective anisotropy constant
V	volume
a	number of atoms per unit cell
E	energy
$\hat{\mathbf{K}}$	demagnetizing kernel
$N_d(E_F)$	density of states of d-electrons at the Fermi energy

λ_{LS}	spin-orbit coupling constant
ϕ_{vv}	nanotube diameter measured from vertex to opposite vertex
R	resistance
$\hat{\mathbf{G}}$	Green's tensor
σ	conductivity
L	orbital momentum or length or inductance
$\mathrm{T_C}$	Curie temperature
ζ	permalloy evaporation angle
v_p	phase velocity
N_f	number of frames
s	distance covered by spin waves

Acknowledgment

First of all I would like to thank my supervisor Prof. Dr. Christian H. Back for offering me the possibility to work on his chair at the university of Regensburg. The sharing of knowledge during weekly group discussions helped me a lot.

I would like to thank Prof. Dr. D. Bougeard and his group members for growing the samples in the III-V MBE system. Without all of you I would have no samples to start with in the first place. Here I would especially like to thank Florian Dirnberger for the early (and late) hours, he spent with me at the MBE chamber. His level of frustration tolerance is admirable.

Thanks to the collaboration with the group of Dr. J. Lindner from the Helmholtz-Zentrum Dresden-Rossendorf (HZDR) I became acquainted with many interesting people. The PMR-based FMR measurements have been conducted at the institute under his supervision. I would like to especially thank Attila Kakáy for the great time at the beamtimes in Berlin and in Villingen (CH). It is hard to mention everything I need to thank Attila for, since it would need some extra pages. In short, thank you for all the fruitful discussions, ideas, work and help.

A big thanks to Thomas N. G. Meier. No matter what problem I faced, Thomas was always there to help. This includes help with experimental setups like the SEMPA, with simulations, with calculations and general discussions. Thank you for the fun time.

A special thanks to my parents Michael and Eveline, who always stood by me.

Thanks to my beloved girlfriend and future wife, Daniela, for the time I could share with you beyond work. I love you more than anything in the world.

I would also like to thank:

Matthias Kronseder for the help with the MBE system and the general help if problems of any sort arose. Thank you for proofreading this thesis.

Martin Decker for the work at the TRMOKE setup and also for many discussion on magnetic nanotubes and related topics.

Johannes Stigloher for helping me with simulations at the beginning of my thesis and for answering many questions.

Sebastian Wintz and Simone Finizio for the support at the beamtimes

Thanks to all members/ex-members of my office for the great time: Alex, Daniel, Simon, Thomas, (robotic) Swientek. Its hard to imagine finding something similar to our office ever again.

And finally I would like to thank all the table football players: Martin, Matthias, Hannes, Robert, Jan, Anton, Helmut, Daniel, Adrian.. I always looked forward to the coffee break because of you guys.

List of Publications

Covered in this thesis:

M. Zimmermann, T.N.G. Meier, F. Dirnberger, A. Kákay, M. Decker, S. Wintz, S. Finizio, E. Josten, J. Raabe, M. Kronseder, D. Bougeard, J. Lindner and C.H. Back. *Origin and manipulation of stable vortex ground states in permalloy nanotubes.* Nano Lett., **2018**, 18(5), 2828-2834

M. Zimmermann, M. Decker, E. Josten, J. Stigloher, F. Dirnberger, T.N.G. Meier, D. Bougeard, J. Lindner, C.H. Back and A. Kákay. *Dynamical magnetic properties of individual permalloy nanotubes*. (to be published)

M. Zimmermann, J. Otalora, F. Dirnberger, H. Schultheiss, M. Decker, S. Wintz, S. Finizio, D. Bougeard, J. Lindner, C.H. Back and A. Kákay. *3D transport of spin waves in magnetic nanotubes*. (to be published)

Other contributions:

T.N.G. Meier, M. Kronseder, **M. Zimmermann** and C.H. Back. *Quantification of thermal fluctuations in stripe domain patterns.* Phys. Rev. B, **2016**, 93(6), 064424

M. Kronseder, T.N.G. Meier, **M. Zimmermann**, M. Buchner, M. Vogel and C.H. Back. *Real-time observation of domain fluctuations in a two-dimensional magnetic model system.* Nat. Com., **2015**, 6, 6832

Erklärung

Die vorliegende Arbeit wurde selbstständig von mir verfasst. Es wurden keine anderen als die angegebenen Quellen und Hilfsmittel benutzt. Die Arbeit wurde bisher keiner anderen Prüfungsbehörde vorgelegt.

Regensburg, 26.07.2018

Michael Zimmermann